Advanced GPR Data Processing Algorithms for Detection of Anti-Personnel Landmines

The picture on the cover represents the action of the algorithm of target detection in clutter developed by the author. (See also chapter 3 of this thesis).

Advanced GPR Data Processing Algorithms for Detection of Anti-Personnel Landmines

Proefschrift

ter verkrijging van de graad van doctor

aan de Technische Universiteit Delft,

op gezag van de Rector Magnificus prof. dr. ir. J. T. Fokkema

voorzitter van het College voor Promoties,

in het openbaar te verdedigen op donderdag 7 december 2006 om 12:30 uur

door

Vsevolod KOVALENKO

Specialist (Master of Sciences) in Applied Mathematics

Karazin Kharkiv National University, Oekraïne

geboren te Kharkiv, Oekraïne

Dit proefschrift is goedgekeurd door de promotoren:

Prof. dr. ir. L. P. Ligthart
Prof. dr. sci. O. G. Yarovyi

Samenstelling promotiecommissie:

Rector Magnificus	voorzitter
Prof. dr. ir. L. P. Ligthart	Technische Universiteit Delft, promotor
Prof. dr. sci. O. G. Yarovyi	Karazin Kharkiv National University, promotor
Prof. ir. P. van Genderen	Technische Universiteit Delft
Prof. dr. ir. A.P.M. Zwamborn	Technische Universiteit Eindhoven
Prof. dr. M. Sato	Tohoku University
Prof. dr. J.-Y. Dauvignac	Universite de Nice-Sophia Antipolis
Prof. dr. sci. V.V. Sazonov	Moscow Institute for Physics and Technology
Prof. dr. ir. M. H. G. Verhaegen	Technische Universiteit Delft

This research has been supported by the Technology Foundation STW, applied science division of the Dutch Organization for Scientific Research NWO.

ISBN-10: 90-76928-11-8
ISBN-13: 978-90-76928-11-1

Keywords: ground penetrating radar data processing, antipersonnel mines detection

Copyright © 2006 by Vsevolod Kovalenko

All rights reserved. No part of the material protected by this copyright notice may be reproduced or utilized in any form or by any means, electronic or mechanical, including photocopying, recording or by any information storage and retrieval system, without written permission from the author.

Printed in The Netherlands

to Anastasia

CONTENTS

Chapter 1 Introduction

Antipersonnel landmines (APM) represent a constant threat to civilians and military units in many countries all over the world. Land mines are used to secure disputed borders and to restrict enemy movement in times of war. In a military theory APM serve a purpose similar to barbed wire or concrete dragon's teeth vehicle barriers, channeling the movement of attacking troops in ways that permit the defenders to engage them more easily. From a military perspective, land mines serve as force multipliers, allowing an organized force to overcome a larger enemy. But being comparatively cheap the APM are dispensed over large areas where they remain long after a war has ended. Presence of the APM often causes civilian deaths or mutilation and the fear of them results in economical disasters in rural areas affected by wars. According to anti–land mine campaigners, in Cambodia alone, mines have resulted in 35,000 amputees after the cessation of hostilities. Removal of landmines is dangerous, slow and costly. The total amount of deposited APM is estimated in excess of 100 millions and is growing [1, 2].

Although they may come in different shapes and sizes, the majority of the most widely spread APM follow the description of a small plastic cylinder of 5 to 12 cm in diameter and 4 to 8 cm in height filled with TNT [3]. Inner composition of APM varies from type to type and some of the developed technologies are in principle able to differentiate between the types. However, the main problem on the practical level remains low or no metal content of some of the APM of modern types. It is generally percept that the versions of the APM, which possess considerable amount of metal, represent lesser challenge in their detection.

The detection and clearance of the APM is very difficult and very important task. An area is counted as 'cleared of mines' if 99.6% of all mines formerly present in it have been detected and removed [2]. Although there is no clear restriction on the false alarm rate (FAR) but it is generally understood that the higher the FAR, the more time consuming, tiresome, and expensive the demining becomes. Currently, the main tool to locate an APM is still a prod. The prodding during which the whole area is meticulously tested by manually inserting a prod into the ground is a slow and dangerous process. The FAR here often counts to 100 false alarms per correct detection. Therefore the prodding is often preceded with the use of an inductive metal detector. This device allows fast and reliable detection of metal. There are two problems related to it: a) some of the mines contain little or no amount of metal and b) former battle-fields often contain too much metallic debris, which prevent tuning of the detector to low metal content.

Therefore many alternative technologies to help mine detection are under development. They include both biological such as the use of dogs, rats, pigs and even plants (see the discussion in [2]) and different non-organic approaches. Among the last the most promising are (in no particular order) Thermal Infra-Red cameras, Nuclear Magnetic Resonance based devices, artificial noses, and Ground Penetrating Radar (GPR).

This thesis is focused on the development of the algorithms of improved detection of the plastic-cased landmines with Ground Penetrating Radar. The Introductory chapter continues with the state of the art description of GPR technology. The approach taken to the developments of the thesis based upon this description is outlined in the conclusion to the chapter.

1.1 GPR technology for mine detection

Ground penetrating radar is a noninvasive electromagnetic geophysical technique for subsurface exploration, characterization and monitoring [4]. Its operation is based on emitting of electromagnetic waves into the ground where they are scattered by the nonhomogeneities. The energy scattered by the inhomogeneities in the soil is registered by the radar. The data acquired during these measurements are used to infer the structure of the subsurface. The reason of applicability of GPR to the problem of detection of APM coincides with the source of the main difficulty in its use. GPR is sensitive to any inhomogeneity in the ground. Therefore any APM regardless of the metal content can be detected. On the other hand, all the inhomogeneities, which do not represent mines, show up as a clutter in GPR images.

By the way GPR devices emit their probing waves they can be divided into two groups: the stepped frequency continuous wave and video-impulse radar. In the first case radar constantly radiates a sinusoidal electromagnetic wave, which frequency is changed by a certain law. In the second case a short electromagnetic video-pulse is emitted. Both types of GPR are developed for the use in mine detection. It is generally accepted the pros and contras of the two approaches have primarily technical nature and well balance each other.

The other way to divide mine-detection GPR devices is by the mode of their operation. GPR are made hand-held, vehicle mounted or platform mounted. This is a more principal division and the radars developed for different operation mode normally solve different problems.

1.1.1 Hand-held devices

The hand-held devices are supposed to be operated much like the inductive metal detectors. An operator of such radar covers the interrogated areas with sweeping motions trying to maintain constant velocity of movement and height of the antennas. As none of this requirement is easy to adhere to, the data processing and feature extraction algorithms are difficult to develop. On the other hand, such devices are easily transportable, may be used in difficult terrain conditions and what is also important are cheap [5].

The mine detection by these devices normally is confined to the detection of change in the background, which can be attributed to the presence of an object [5-9]. The resulting false alarm rate is quite high and therefore various advanced techniques aimed at lowering it are developed. Encouraging results have been re-

ported on the use of data processing based on hidden Markov models [6-8] and even Synthetic Aperture Radar [9]. Moreover, the hand held devices are often paired with inductive metal detectors into the sensor arrays [5, 9]. In the latter case it has been reported in [8] that the performance of the automated EMI/HH GPR sensor array was close to if not surpassing the performance of a human expert.

GPR of this class are aimed at the mine detection in the terrains difficult to access where no other solution is possible. On the other hand, there exist inherent limitations on the size and weight of these devices and problems related to their operation mode. These problems and limitations can be overcome by larger devices mounted on different types of vehicles.

1.1.2 Vehicle-mounted devices

The main alternative to the hand-held devices are the vehicle-mounted ones. These devices are mounted on various types of vehicles and may be used where the interrogated terrain allows the movement of the carriers. GPR of this type are divided into the two groups: forward-looking devices and downward-looking ones.

The forward looking devices, such as NIITEK-Wichman [10-12], FLGP-SAR [13], GPR developed in Stanford Research Institute [14], and some others operate in predicting mode. They illuminate the interrogated terrain obliquely and receive part of the energy scattered by the mines. In such a set-up plastic-cased APM are very difficult to detect and the whole approach is more characteristic to the anti-tank mine-detecting devices. At the same time the technology of detection of the anti-tank mines with the forward-looking GPR devices has been already developed to the industry level [15].

As a main alternative, the vehicle mounted GPR may be downward looking. In this case the device is fixed on a frame in front of or to the side from the carrier. The device then interrogates the terrain directly underneath it. Some of the systems implementing it have been developed to the industry or industry-prototype levels [16-20]. Most of the University level research is made around the systems that emulate the downward-looking vehicle mounted GPR approach, where a vehicle is often replaced with an accurate scanning platform [21-28]. The popularity of the approach is explained by the fact that if technically feasible it represents the best possible conditions from the radar point of view.

1.1.3 IRCTR Scanner-mounted GPR

The mine-detecting ground penetrating radar developed at IRCTR [29-31] represents a very accurate realization of a scanner-mounted downward-looking video-impulse GPR. The general idea behind the development of this device was implementing of the most flexible and extensive set of radar possibilities. The developers compromised on the cost and weight of the radar in order to assure the stability and vastness of the data it provides.

The resulting GPR simultaneously uses two orthogonal polarized transmit antennas [30] and four receiver antennas connected to the independent channels correspondingly. This set-up results in four co-polar and four cross-polar receiving channels. The identical dielectric wedge antennas are used as transmitters, identical loops are used as the receivers. The receive antennas are placed directly underneath the transmitters in order to narrow the footprint of the antenna system and thus to enhanse its spatial resolution. One of the consequences of the design is that the direct wave is the largest signal in the system, which defines the upper limit of the system's dynamic range. The radar is capable of collecting single echo-returns (called A-Scans) in the stop-and-go and continuous modes. The continuous data acquizition results in echo-profiles (called B-Scans). Collections of adjacent B-Scans constitute 3D datasets (called C-Scans) which are the primary format of the raw data for the device.

The radar (Figure 1.1) has 4 quasi-monostatic transmitter-receiver pairs (T1R2 and T2R1 co-polar; T1R3 and T2R4 cross-polar) and 4 significantly bi-stactic ones (T1R1 and T2R2 co-polar; T1R4 and T2R3 cross-polar). The radar is therefore capable of collecting fully polarimetric data. The heights of the receiving loops over the surfaces vary from 10 to 30cm depending of the scanner platform settings. The distance between the receiver loop and the aperture of the transmit antennas is 28 cm.

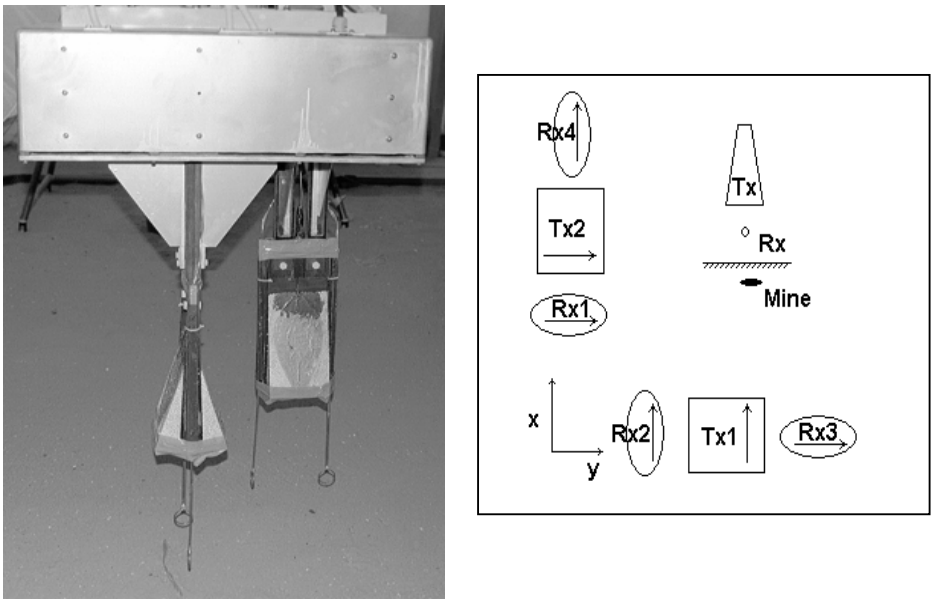

Figure 1.1 Video-impulse GPR of IRCTR (left) and its antenna configuration (right); Txi represent transmitting and Rxi – receiving antennas

The high quality of the hardware and the high stacking number provide a sub sample stability of the firing times of the generator. The jitter of the system has been determined equal to 6.47 ps on the entire C-Scan. After the slow trend of the generator towards the earlier firing time has been removed from the data the jitter becomes smaller and equals to approximately 3.5 ps. In both cases the jitter is well inside of one sample. The Radar and Scanner used to acquire the data considered in this thesis are detailed in Appendix C .

1.1.4 The main challenge in mine detection with GPR

It has been shown by the results of many researches that the problem of APM detection can not be solved on a straightforward hardware level [2, 5, 12, 15, 23]. That is, unlike the 'signal detection in noise' situation the mine detecting radar faces the following problem: the more sensible and accurate the hardware is the more of ever-present soil inhomogeneities and friendly objects it detects. Moreover, the energy scattered by the plastic-cased APM is very often lower than that scattered be friendly objects and even in some cases by the surface roughness. This renders the 'level threshold' detection inapplicable and the necessity in development of feature based detection becomes apparent. In turn, any type of feature-based detection requires the development and application of sophisticated data processing algorithms.

From a humanitarian demining perspective I see the following main challenge in mine detection with GPR. The false alarm rate on the (nearly) 100% detection level must be lowered until acceptable level. The acceptable level supposes that the operation of mine detection becomes faster in comparison with currently existing techniques (hence metal detector aided prodding). In order to achieve this goal a framework of data processing, feature selection and feature fusion algorithms must be built.

The issues connected with the building up of such a network will be treated in the present thesis.

1.2 Data processing algorithms

Successful detection of APM especially plastic-cased requires development of various feature-based detectors. This implies the development of the techniques of clutter suppression, feature selection and extraction, feature fusion, and multi-feature based detection. Virtually every landmine detecting GPR is equipped with its own set of data processing and interpretation routines. The algorithms accompanying each GPR correspond to the conditions in which the device is supposed to operate and to the problems it has to solve. The GPR data processing algorithms can be conventionally divided into four large classes of: clutter suppression, focusing, feature extraction and detection, and feature fusion.

1.2.1 Clutter suppression algorithms

As it was mentioned above, the main problem for detection of APM with GPR is the clutter. The clutter, which is defined as any electromagnetic phenomenon not associated with targets, cannot in general be treated as white additive noise. This significantly complicates the issue of the clutter suppression. Most of the algorithms of clutter suppression are based on the background subtraction in various forms [32-37]. The main idea of the algorithms of this type is the definition of the background model and then subtracting it from the measured signals. The simplest form of such algorithm is mean value elimination, often used in civil GPR systems in the generic or windowed format. In the latter format it has been implemented with some success for the mine detection GPR [32]. In [32] a 3-D realization of this approach where the averaging is made over an elliptic cylinder centered on the A-Scan in question is used. The technique has been shown to successfully eliminate the direct coupling and to a large extent suppress the surface bounce. Success in the latter aspect generally depends on the apt selection of the size of the averaging cylinder. Various implementations of the same approach that use median filtering etc. were also considered [33-35]. All these approaches, however, fail at least partially if the surface roughness is such that the apt selection of the averaging (or median determination etc.) radius leads to the disruption of the target signatures.

Thus more sophisticated approaches to the clutter characterization are developed. A characteristic example of such developments is reported in [36] where the scattering associated to background and targets are represented with damped exponential models. Differences in the model parameters for the cases of surface roughness and localized objects are successfully used to suppress the background clutter better than average elimination.

Another approach has been suggested in [37] where a Gaussian model for surface roughness was assumed and used for construction of the algorithm clutter suppression. The algorithm uses the times of arrival of clutter/target wavelet phenomena for optimal projection of them onto ‘ideal flat surface’ space. The differences in the resulting projections between the ‘clutter alone’ and ‘clutter and target’ situations are used for suppressing the former.

Despite significant successes achieved inside the clutter model approach there exist a principal problem, which they cannot overcome. Namely, regardless of how successful the surface clutter selection is, the algorithms constructed based on its model cannot suppress the electromagnetic phenomena associated to localized objects. Hence the responses of APM and friendly objects alike are not suppressed by the algorithms. This often leads to the inflation of false alarm rate. A possible solution can be found by constructing the clutter suppression algorithms operating from the ‘target model’ approach.

1.2.2 Focusing algorithms

Additive noise itself can be a problem for detection of plastic-cased APM due to their small size and weak scattering contrast. On the other hand, it is well known that electromagnetic phenomena associated to any localized object including APM leave hyperboloid-like traces in C-Scans. Exploiting this information it is possible to collapse these traces into localized bulbs using some kind of a focusing transformation [4]. The focusing is a common technique which ultimately uses a sort of a radon transformation [38] to coherently sum the signals scattered by localized objects. The improvement in signal to noise ratio (SNR) is caused by self-cancellation of the non-coherent noise phenomena, whilst object-related phenomena are summed coherently and thus enforced. Synthetic Aperture Radar (SAR) technique is a closely related concept from a remote sensing [39] that uses similar transformation to increase the images resolution. It can be shown that the SAR formulation implements the optimal filtering technique for imaging of a point object on the basis of a B-Scan or a C-Scan [40]. In [40] SAR 2D technique had been successfully applied to GPR data to improve resolution of the images of elongated objects. The generic form of a focusing algorithm in time domain can be represented by:

$$F(\vec{r}) = \iint\limits_{\xi,\gamma \in A} C_{\xi,\gamma}(T)\, d\xi d\gamma \tag{1.1}$$

where $\vec{r} = (x, y, z)$, the point being imaged, $C_{\xi,\gamma}(\cdot)$ and $F(x, y, z)$ represent initial and focused C-Scans, A is the 2D aperture of the radar to be synthesized, and T is the time needed for a probing pulse to travel from the transmit antenna to the point being imaged and backwards to the receive antenna. Techniques of same type can be applied in frequency domain, which leads to the similar formulations [13, 41]. Other developments in this direction include the combination of the delay-and-sum approach techniques with those originated in wave equation [42] and attempts to speed up the computation process by a technique resembling FFT in Cooley-Tukey formulation [43].

Another approach to the focusing is a wave-equation based migration. The wave-equation based migration is a technique originating from geophysics [44] where it used as a primary imaging tool. Some connections between the migration and SAR – based techniques were established [45, 46] but the former is lesser known in APM detection.

As it is shown in number of publications, the use of focusing techniques is a highly desirable step in GPR data processing chain for detection of APM. These algorithms by themselves do not separate the targets from friendly objects, but they a) suppress the noise very effectively, b) transform the data from time- to depth-domain, which greatly helps interpretation of the images, and c) allow more effective use of feature-based detection algorithms. The drawback is the high computational load and hence the time consumption, which makes them inconvenient if not impossible to use when a real-time processing is demanded.

1.2.3 Feature based target detection algorithms

As already discussed, the detection of APM mines with GPR on the basis of energy threshold alone leads to unacceptably high false alarm rate. Therefore, the detection must be made on the basis of one or more *features*. A feature in this context means any scalar number parameter f , which can be associated to any object (or set of coordinates) suspect for being (or hosting) a target. This definition describes a generic target detection algorithm in a hypothesis testing theory terms:

$$\begin{cases} H_0(f): & \text{target signature} + \text{clutter} \\ H_1(f): & \text{clutter only} \end{cases} \tag{1.2}$$

This is a fairly common definition of the detection problem to target detection, so most of the publications referred above describe their approaches in these terms. It is understood that the more distinguishable the distribution densities of a feature f are for the classes of target and clutter, the better detection level is achievable. It is also understood, that more than one feature is employed for the decision making. However for the two-class hypothesis testing problem (1.2) the optimal decision is made on the basis of exactly one feature [45]. This means that the generic fusion process takes as an input an arbitrary amount of scalar features and results in a single fused (decisive) one.

A vast variety of features is used to detect the APM. In every particular case the features are selected taking into account the nature of the problem and the characteristics of the targets and the hardware. Hand held devices require very robust approaches. In [6] the detection with hand held GPR is considered in depth. As mentioned before, only a limited set of features is robust enough to be used in this set-up. In the reference a measure of the deviation of measured data from what is predicted by a background model is used as a numerical parameter. Obtaining quite promising results in terms of detection the authors had to settle with quite high rate of the false alarms. They developed a more sophisticated technique [8] combining the hand held GPR with metal detector. The main feature used to discriminate between targets and clutter was the closeness of the observed figure in a frequency domain to a predefined ‘target pattern’. This feature has shown supremacy over energy detection in the presence of friendly objects.

Detection of APM using vehicle-mounted and simulating them scanner mounted devices provides the possibilities of using thinner features. For example in [22] the background model is defined and then updated considering consequent A-Scans. The list of features suggested for the mine detections include: ‘amount of innovation’ introduced by a tested A-Scan into the Kalman filter; the difference between a background signal and a tested A-scan measured using pulse deconvolution, wavelet decomposition, and trimmed average power. The Kalman filter based technique is demonstrated to have the superiority over the other three. As the work is solely based on the background model the robustness of the approach to the presence of friendly objects is not covered.

In [17] a fuzzy logic approach is used to detect hyperboloid traces left by targets. The detection is quite successful but since any localized object can be characterized with hyperboloid traces no robustness to the presence of friendly objects is outlined in this reference. Analogous results are obtained with the use of the level of polynomial fitness of the object traces as a primary feature [11]. Further developments of the algorithms based on the hyperbola-distributed phenomena include the use of hidden Markov models [18, 19] and higher order statistics [12].

Almost entirely different features are used when the detection is made in focused GPR images. In this case all localized objects are represented in images with bulb of various shapes and intensity. In [43] the time-frequency analysis apparatus is employed to distinguish between the targets and friendly objects. Coefficients of Choi - Williams distribution are used to form the decisive feature (see subchapter 1.2.4 on the details of the fusion process). In [44] essentially the waveform of the object image in focused A-Scan is used to distinguish between the targets and clutter.

Seemingly in all cases described in the references the detection of the plastic cased APM is achievable. On the other hand, achievement of an acceptably low rate of false alarm is much more challenging and an open problem. It is also quite visible that this problem cannot be solved by one measured feature. Therefore: a) methods of clutter suppression should be further developed and b) feature fusion techniques should be studied.

1.2.4 Feature Fusion

It has been seen already that the problem of detection of APM requires the use of multiple features. The optimal way of combining the information these features provide is called feature fusion. Besides, the problem of fusion of different features for target detection always arises when any multi-feature system is used. A system may comprise sensors of different nature, or just independently acting radars, or the same radar operating in different modes, or even the same flow of the raw data from the radar can be processed by different algorithms, which produce different features.

Three of the examples considered in the previous subchapter required the fusion of the used features. In particular, the hand-held GPR combined with an EMI sensor in [19] utterly provided the set of two confidences coming from each of the sensors. In that reference the fusion is organized by simple take of a geometric mean. In [43] the coefficients of time-frequency distribution taken as individual features are combined into the decisive feature by means of linear discriminant analysis [45]. The waveform based detection in [44] is organized via maximum deflection criterion based quadratic classifier [46].

The fusion of the features obtained from cooperating sensors is a separate and actively investigated topic. Here I mention the main direction of its development in application to the detection of APM. In [47] a feature and decision-level fusion of infrared camera, GPR, and metal detector is treated. The authors apply generalized

maximum likelihood theory to the problem. A multivariate target and clutter feature distributions are evaluated from training data by means of Monte-Carlo like modeling. The performance of the resulting classifier is quite high when evaluated via leave-one-out method (all of the data except for one target are used for training and this one target is then detected). As no blind test is provided it is impossible to assess the robustness of the algorithms.

On of the two main alternatives to the generalized likelihood ratio approach in feature fusion is the use of the Dempster-Shafer evidence theory [48]. In [49] this theory is used to build-up a two-level belief function model for EMI/GPR/IR sensor array. The result of the fusion clearly demonstrates the superiority of the sensor array over any given sensor. It is difficult to judge the robustness of the algorithm to the change of the environment and targets as no blind test is provided. In [50] the same theory is used to fuse the data from EMI/GPR sensor array. Although the belief system in this case has one level, the gain given by the use of the fusion is clearly demonstrated. The research is done in laboratory conditions and this prevents the assessment of the robustness of the algorithms

In [51] the problem of data fusion in polarimetric IR/GPR sensor array data fusion is considered. The author uses the second main alternative to the generalized likelihood test, which is a development of the k-NN (k nearest neighbors) approach. A learning vector quantifier (LVQ) classifier provides very impressive results when tested by leave-one-out approach. But the performance was less impressive when the blind test is done. The variability of the feature from the training to the test site is given as the main reason for the deterioration of the performance. But the overtraining of the algorithm may also occur as the k-NN based algorithms often have quite complex decisive border [45].

Use of the generalized likelihood ratio approach (or Bayesian approach) is the optimal way for the feature fusion [45]. However, it is embarrassed by the necessity of evaluation of complex integrals to compute the feature densities. Moreover, the approach can also be plagued by the overtraining issue. At the same time the cheap alternative provided by the maximum likelihood based quadratic classifier is only optimal for the normally distributed features and fails when the feature distributions are skewed. However there exist methods of quasi-normalization of distributions [52] and these methods will be adapted in the thesis to help the mine detection with GPR.

1.3 Conclusion for Chapter 1

As it is seen from the description above the Ground Penetrating Radar can and should be used in mine detection. The main difficulty on this way is the high false alarm rate. As it can be seen from the introductory chapter a wide range of questions remain open in the research on the APM detection using GPR. In this thesis I shall take on the problem of reducing the false alarm rate in APM detection using multi-waveform full-polarimetric video-impulse GPR. The two main instruments that will be developed and used to achieve this goal are:

- Statistics based multy-feature detection;
- Waveform based clutter suppression

Suggested approach is sound since it is based on the firm theoretical basis both in feature-fusion [45] and clutter suppression [53] aspects. At the same time the approach is novel since the algorithms of feature pre-normalization and feature fusion are not found in the literature in application to land-mine detection. Also the importance and perspectives of the wave-form analysis in landmine detection is mentioned in several published papers [26, 43] but this aspect of GPR data processing is not yet explored.

The following statements will be substantiated in the thesis:

1. An open automated framework of the multi-feature based detection of APM with use of GPR can be developed
2. This framework should use Bayesian approach to the feature fusion expressed by means of the linear-quadratic classifier
3. In order to enforce effectiveness of such classifiers certain measures should be undertaken to ensure the (quasi) normality of the decisive features
4. The current state-of-the art approach to the clutter suppression is based on the concept of decrypting the clutter and detecting any deviation from it. This approach is important but in itself unsatisfactory for lowering the false alarm rate.
5. The wave-form based clutter suppression algorithms can be developed. In such an approach the clutter suppression would operate from the target model and suppress all waveforms, which cannot represent targets. It is supposed that such an approach when paired with the classical can significantly improve detectability of targets and suppress the false alarm rate.

The present thesis is built on the following assumptions:

1. It is supposed that any given decisive feature forms a confidence map in which the targets may be detected independently. Auxiliary features may be constructed using such a map.
2. It is supposed that an optimal set of features representing targets can be devised from a training site and then used at a blind test site.

The thesis is organized in the following way. The core of the statistical approach and feature normalization techniques are described in the Chapter 2. The Waveform based clutter suppression techniques are discussed in the Chapter 3. The process of forming of confidence maps is treated in the Chapter 4. Also in that Chapter the procedure of the selection of the best features to detect the targets in the given conditions is discussed. The algorithms suggested and described in the Chapters 2 -4 are tested on the measured data in the Chapter 5. The Chapter 6 represents the Conclusions for the thesis. The descriptions of technical character, such as details on the operating hardware, data pre-processing, measurement sites and set-ups are given in the Appendix.

The construction of the data processing framework presented in the Chapter 2 constitutes a novelty. The algorithms of simultaneous quasi-normalization of the

feature distributions for the classes of target and clutter discussed in Chapter 2 are also novel. The entire scope of the Chapter 3, i.e. waveform based clutter suppression/target detection techniques described in the chapter, is original. The projection techniques presented in Chapter 4 were also developed by the author.

Chapter 2 Statistical Approach to Feature-based Mine Detection Using GPR

As it has been shown in the Chapter 1, GPR technology can be successfully used for detection of plastic cased APM. However, the false alarm rate, which corresponds to a 99.6% detection level, may be unacceptably high for any single feature or even single sensor. Therefore it is necessary to come up with a framework that would allow detection of APM on the basis of several different features extracted from the GPR data. The GPR data in turn can be processed in several different ways to allow the extraction of various features.

In this chapter I suggest such a framework. It represents a statistics based approach to the mine detection incorporating a set of features, each having its own distribution for the classes of mines and clutter. The feature characterization approach is based on sample probability density functions for classes of targets and clutter learned from a training set. In this approach for each feature map the sample probability density functions are modeled either parametrically or non-parametrically based on the data acquired at a training site.

A short description of the framework reads: a 3-D GPR dataset is processed to produce a 2-D map of certain decisive feature; each point on the resulted map represents a confidence of a mine being present in (or underneath) the given location according to the given feature; the probability of the mine or clutter presence in the location is computed on the basis of confidences and their distributions learned from a training dataset. Using the probability distributions of individual features a quadratic classifier is built based on either maximum likelihood (ML) or maximum deflection (MD) criterion. In order to ensure that the quadratic classifier does indeed correspond to one of the criteria the individual features are transformed in such a way as to ensure their normal distribution. The resulting classifier is used as a plug-in rule on a test site.

Unlike the approaches suggested in [50-52, 54-60] the current one makes use of quadratic classifiers [45]. These classifiers stem from generalized likelihood test approach and are more robust than nearest neighbor based approaches when used as plug-in rules. The approach is illustrated in the Figure 2.1 in the form of a flow diagram. Following the diagram, one starts acquiring the data with one or multiple data acquisition scenarios, thus producing P_R *raw* C-Scans. These raw C-Scans undergo a data pre-processing step, which enhances the quality of the data in the technical sense (for the details see Appendix A.2). One or several Data Processing Schemes are applied to each of the pre-processed C-Scans thus yielding:

$$P_D = \sum_{i=1:P_R} \sum_{DPS_i=1:D} CM \tag{2.1}$$

confidence maps. The initial detection is made in each of these maps. The confidence value found in each detected location constitutes a scalar feature. Collection

of these features, each possibly supplemented with some additional co-features derived from its map, constitutes the output of the data processing scheme. Together they form the pool of decisive features. The features constituting this pool are independently transformed in such a way that their distribution densities become (quasi) normal for training data. The normalized features are used for feature fusion resulting in one fused decisive feature. The final decision is made comparing this feature against a threshold.

Therefore the suggested approach is the non-supervised one in which any available data are processed independently to form the feature pool, then are normalized, and then are subjected to the classification by a quadratic classifier.

Further in this chapter I shall detail on the processes encapsulated in the diagram in Figure 2.1. Namely, the Chapter is organized in the following way: I shortly describe a generic automated data processing scheme (DPS) developed by myself in the subchapter 2.1; the feature fusion techniques are addressed in the subchapter 1.1; and a very important notion on the feature normalization is discussed in the subchapter 1.1.

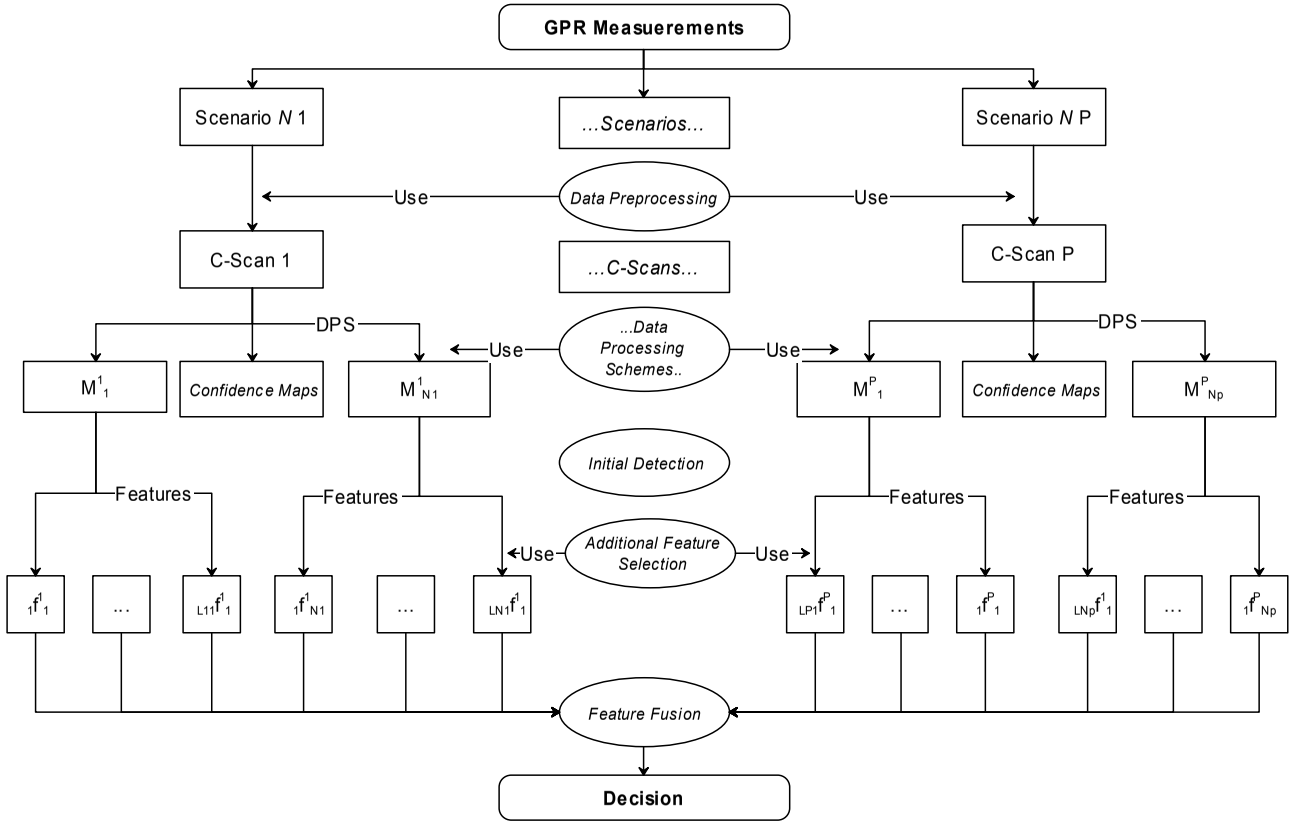

Figure 2.1 Diagram of the suggested approach to mines detection

2.1 Automated data processing schemes

As it was shown in the Chapter 1.1, data processing schemes for automated detection of APM typically contain steps aimed at the clutter suppression, feature extraction, amplification and feature based target detection, labeling of the locations suspect for the presence of the targets, assigning a decisive feature value associated to each suspect spot, and finally target/clutter dichotomy by means of a threshold. Thus a generic DPS follows the paradigm:

$$\begin{aligned} &\textit{Clutter Suppression} \rightarrow \\ &\textit{Feature Extraction} \rightarrow \\ &\textit{Confidence Mapping} \rightarrow \\ &\textit{InitialDetection} \end{aligned} \tag{2.2}$$

Further in this subchapter I describe the particular steps of (2.2) as they are developed for this thesis.

2.1.1 Clutter suppression

As it was discussed in the subchapter 1.2.1, the state of the art in the clutter suppression for mine detection with GPR is set on the background removal. The successful clutter suppression means removal of the direct wave, ground bounce, and background scattering phenomena which are not connected to localized objects. For the purposes of this study I select a cylindrical moving window average (MWAE, [23]) as the background clutter suppression tool. The MWAE operator is given by:

$$\widetilde{C}_{xy}(t) = C_{xy}(t) - \frac{1}{N} \sum_{\alpha\xi^2+\beta\gamma^2\le 1} C_{\xi\gamma}(t) \tag{2.3}$$

where $C_{xy}(t)$ is an A-Scan measured at the location <x, y>, and the parameters α and β define the circular window in which the averaging is made. The values of the parameters are selected in such away that the circle they form defines a 'fairly constant' area on the ground. The opposing criterion is that (2.3) should least disturb the responses of targets. The factual radius of this circle is a subject to change from site to site depending on ground roughness and the size of the mines to be detected. For example, for sandy minefield simulation sites considered in this study a 16cm radius is shown to produce good results. This radius is used in the examples throughout this thesis unless explicitly stated otherwise.

The operation defined by (2.3) has been producing acceptable results in removing the direct wave and air/ground interface [32]. However, being a single clutter suppression measure filter (2.3) allows significant amount false alarms. These false alarms may come from any localized object and will be counted as a target. More sophisticated algorithms of background suppression are considered in [36,37,61] but they also fail to suppress the false alarms originated from scattering by friendly

objects. The non-trivial issue of the suppression of this kind of clutter is treated separately in the Chapter 0.

2.1.2 Feature extraction and construction of a confidence map

As discussed in 2.1 some kind of the focusing algorithm is usually applied in a DPS unless a requirement of the causality is posed. In the case when the real-time and/or causality condition is imposed other hyperbola detection algorithms are used [11, 13, 62-64]. All these algorithms just like focusing exploit the hyperbola-like spatial distribution of electromagnetic waves scattered by a localized object. In this research no causality restriction was in place and therefore I am using a scalar stack migration SAR algorithm for the data focusing in the thesis.

The SAR procedure used here takes into account the refraction of the probing pulse at the air/ground interface. A spatial interpolation of the raw A-Scans is also used to ensure that the smaller objects are correctly imaged [65].

An optimal construction of a confidence map from a focused C-Scan is a topic for a separate discussion, which takes place in Subchapter 4.1. Here I confine to the note that the energy contained in a focused A-Scan with coordinates <x, y> is a robust feature to determine whether or not an object is placed in this location at some depth [8]. The energy based map is obtained from simple integration along the depth direction:

$$E_{xy} = \int_{z_0}^{z_1} F_{xy}^2(z)dz \tag{2.4}$$

using some kind of approximation of an integral. In (2.4) called Energy Projection (EP) $F_{xy}(z)$ represent focused A-Scans, which are smooth and quite slowly changing functions of depth. This approximation therefore does not represent any difficulty. In the thesis these types of integrals are obtained by a trapezoidal numerical integration.

In the suggested approach I treat the output of (2.4) E_{xy} or any other projection discussed later as a confidence map. Namely, the value taken by E_{xy} in any location <x, y> represents a confidence that a target is placed in it. Note that the confidence may or may not linearly correspond to the probability of a target presence in the given location [51]. If the definition of the confidence level is reduced to the sensor output value (e.g. 2.4) it requires introduction of a specific tool for the initial target detection.

2.1.3 Local Maxima Automated Detector

The tool for the initial target detection in confidence maps must label the locations in which a target is possibly placed. This problem is solved in this thesis by introduction of the Local Maxima Detector (LMD). The LMD calls the detection

in each point of a confidence map where the confidence feature finds its local maximum:

$$B_{xy} = \begin{cases} M_{xy}, \ if \ M_{xy} = \max\limits_{\chi,\gamma\in\Omega} M(\chi,\gamma) \\ 0, \qquad\qquad otherwise \end{cases} \tag{2.5}$$

where B_{xy} is the resulting detections map, M_{xy} is the energy or any other confidence map, and Ω is the vicinity defining the system resolution.

The <x, y> coordinates of non-zero entries of the map B_{xy} form the initial detection list. The values of B_{xy} represent the scalar feature value or the sensor output. As it is discussed later in Chapter 4.2 a few additional scalar parameters may be computed from the statistical properties of the immediate vicinities of the initial detections. The list of the initial detections and one or more scalar feature associated with each entry of the list constitute the output of a data processing scheme.

The effective performance of the LMD is guaranteed for the projection (2.4) or any other type of a confidence map construction provided that a decisive feature takes non-negative values. Use of the LMD is of great importance when dealing with high resolution GPR data. As it is discussed in Chapters 1.1.3, Chapter 1 and Appendix 1.1 a typical confidence map consists of approximately 40000 pixels. It is obvious that no testing that requires considerable computations for each pixel is possible before their number is severely reduced. The LMD provides this reduction producing 15-30 labels per square meter. This number is also unacceptably high for a human expert testing but it allows a fast automated processing of polynomial level of computational complexity.

2.1.4 Parameters of a decisive feature distributions

If a 99.6% detection requirement is relaxed or the amount of false is allowed to be arbitrary high, the mine detection problem can be solved using any one particular map with one decisive feature. To predict the quality of such a solution, one has to possess a knowledge of the distributions of the decisive feature for the classes to separate. Application of a DPS results in an independent random variable *x* that can be described in terms of its probability distribution function

$$\Pi(f) = \Pr\{x \le f\} \tag{2.6}$$

or its probability density function

$$\pi(f) = \partial\Pi(x)/\partial f \tag{2.7}$$

In the training phase the functions (2.6) or (2.7) must be estimated from the measured data for the two classes separately. In the unlikely case where a good model exists for a prediction of a feature density, the training data are used to fit the parameters of this distribution. In this case only a few numbers describing the parameters of the distribution must be fitted. In other cases the distribution density may be described non-parametrically using techniques like normalized histograms

[66] or non-parametric kernel estimation [67]. In the latter case the probability density of a feature f is estimated from the measured dataset $\{x_i\}_1^n$ via:

$$\hat{\pi}(f) = \frac{1}{nh}\sum_{i=1}^{n} K\left(\frac{f - x_i}{h}\right) \tag{2.8}$$

where $\hat{\pi}$ is the estimation of the density, n is the number of samples taken for the estimation, h is the window width, and $K(\ )$ is a differentiable kernel function satisfying

$$\int_R K(x)dx = 1 \tag{2.9}$$

Gaussian or Epanechnikov kernels are used the most often. The kernel estimation technique is more robust than the one based on the normalized histograms. Moreover, it produces a result that is differentiable, which is of importance for some algorithms.

The most important for this study feature distribution parameters are conveyed in its first 4 moments. They can be estimated after the feature distribution function is described or alternatively computed directly from the measured data. The first two moments are estimated via:

$$\mu_1 = \frac{1}{N}\sum_{k=1}^{N} x_k \tag{2.10}$$

$$\mu_2 = \frac{1}{N}\sum_{k=1}^{N} (x_k - \mu_1)^2 \tag{2.11}$$

where N is the size of the dataset. These moments define centrality and spread of the data and the data itself if they are normally distributed. If the latter is not the case the higher order moments must be taken into account. In this study considerations will be confined to the moments of the third and forth order. These moments will be used in the normalized on the variation form in which they are called skewness and kurtosis. Their sample estimation are defined by

$$Sq = \frac{1}{N}\sum_{k=1}^{N} \frac{(x_k - \mu_1)^3}{\mu_2^{3/2}} \tag{2.12}$$

$$Kr = \frac{1}{N}\sum_{k=1}^{N} \frac{(x_k - \mu_1)^4}{\mu_2^{4}} \tag{2.13}$$

The quantity Sq defines how much a distribution is skewed ($Sq = 0$ for symmetrical distributions), while Kr determines the sloping of the distribution's shoulders ($Kr = 3$ for the normal distribution). These quantities are used for the pseudo-normalization of the feature vector distributions as described in the Section 2.3.

2.1.5 Target/clutter dichotomy and ROC curves

It follows from the Bayes theorem that the optimal separation of L classes can be achieved using *L-1* features [45]. For our two-class case this means that a) feature fusion must result in exactly one fused feature and b) measure of classes' separability can be assessed in 1D case. The feature fusion is addressed in the separate subchapter 1.1. This subchapter addresses the issue of representation of the separation achieved.

Several possibilities exist to measure the separation of two classes provided by a feature. If the distributions of the decisive feature for the two classes are given by functions $p_i(x)$ one can obtain the Bayes error, which is the quantity describing the amount of misclassification errors in the case of the optimal separation:

$$\varepsilon_B = \int_{-\infty}^{x_*} p_2(x)dX + \int_{x_*}^{\infty} p_1(x)dX \tag{2.14}$$

where x_* is an optimum decision boundary and p_i are the probability densities of the classes to separate. This is illustrated in the Figure 2.2, where the probability densities for the classes of target and clutter are shown. The densities are computed using kernel estimation approach (2.6) – (2.7) from samples of actually measured data. The optimal decision point x_* is at the intersection of the densities and the Bayes error for the given case is $\varepsilon_B \approx 0.027$. The decision point is marked with black line in the figure.

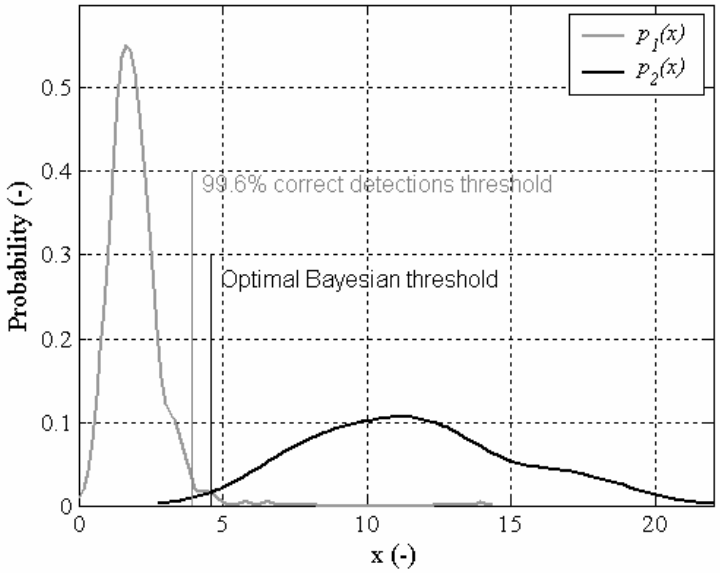

Figure 2.2 Separation of two classes on the basis of one feature.

For the humanitarian demining, however, the decision point is preset to be at 0.996 detection probability and therefore the error should be calculated via

$$\varepsilon_{HD} = \int_{x_0}^{\infty} p_1(x)dX \tag{2.15}$$

where x_0 is the point corresponding to the 99.6% detection level. The point x_0 is marked with a pale line in the Figure 2.2; the corresponding error $\varepsilon_{HD} \approx 0.022$ for the example given. Note, that the definition (2.15) does not include the error due to 0.04% of the missed targets.

Chapter 1. The numbers given by (2.14) and (2.15) are only estimates since they are computed on the basis of estimation of the probability density functions, which oftentimes are only given in measured samples. Alternatively one may obtain bounds for the Bayes error using first two moments estimated from the measured samples without making any assumptions about the distributions. Namely, generalized deflection

$$d(\alpha) = \frac{\left(\mu_1^T - \mu_1^C\right)^2}{\alpha\mu_2^C + (1-\alpha)\mu_2^T} \tag{2.16}$$

and Bhattacharyya distance

$$B = \frac{1}{4}\frac{\left(\mu_1{}^T - \mu_1{}^C\right)^2}{\mu_2{}^T + \mu_2{}^C} + \frac{1}{2}\log\frac{\mu_2{}^T + \mu_2{}^C}{2\sqrt{\mu_2{}^T\mu_2{}^C}} \tag{2.17}$$

also represent the separation of the classes provided by the feature. It is of importance, however, that these estimates are optimal only when the distributions under the test are normal. For the example given above these estimates are equal to 57 (for $\alpha = 0.5$) and 5.7 respectively, which correspond to the high separability. It must be taken into account though that these estimates are optimistically biased since they do not take into account the skewness of the distribution of the class 1 to the right.

The deflection criterion (2.16) is used further in the thesis for optimization of mask parameters in projection algorithms (Section 4.1) while the Bhattacharyya distance is used for the optimization of the parameters of s clutter suppression algorithm (Section 3.1). These numbers should in general be used to compare different features and their discriminative power to each other. The performance of a classifier is better described by a functional called Receiver Operator Characteristics (ROC) curve. There are two distinctive types of ROC curves:

- The parametric curve (threshold is the parameter) for which the probability of false alarm and probability of detection are the X- and Y- coordinates.
- The parametric curve (threshold is the parameter) for which the amount of false alarms is the X- coordinate and amount of correct detections is the Y-coordinate.

The former definition represents the theoretical approach, which can be widely found in the signal processing and detection textbooks [4, 45, 68, 69]. The

latter approach is used wider in the characterization of the demining systems: most papers describing the mine-detection devices include the ROC curves of this type [6-14, 17-28 etc.].

The construction of the probability-probability (PP) ROC curve is only possible if one knows the distributions of the clutter and mines. In other words, to build such a curve it is necessary to characterize the probability density functions of the distributions of false alarms and mines. Then moving a threshold one obtains the theoretical ROC curve integrating the probability density functions from threshold value until infinity:

$$\begin{aligned} x &= \int_{\theta}^{\infty} f_{\text{clutter}}(\xi) d\xi \\ y &= \int_{\theta}^{\infty} f_{\text{target}}(\xi) d\xi \end{aligned} \tag{2.18}$$

where θ is the threshold value. Such ROC curve can be built using the densities estimated using kernel estimation approach or straight from the histogram. The advantage of this definition is that it allows prediction of the classifier performance on other sites provided that the classes to separate would be drawn from the same distribution as the corresponding classes in the training site. The disadvantage is the necessity to estimate the distributions for the classes.

The second definition of the curve does not require distribution modeling and the performance of the classifier is judged on the site, counting the amounts of correctly and incorrectly classified objects:

$$\begin{aligned} x &= Amount\{O_{clutter} \mid f(O) > \theta\} \\ y &= Amount\{O_{\text{target}} \mid f(O) > \theta\} \end{aligned} \tag{2.19}$$

where O_{class} represents objects from the classes of clutter and target and $f(O)$ is the corresponding value of the decisive feature. Often the amount of correct detections is given in percents to the total number of targets, while and the false alarms amount is normalized on a scanned area unit to yield a frequency of occurrence. Even though the normalized entities on the axes are sometimes called 'probabilities' in the literature [6-14], in fact these normalizations do not change the nature of the approach. It is of importance that the curve defined by (2.18) does not allow a comparison of performances of different demining systems unless the tests are made on the same ground. Moreover even prediction of the performance of the system on a test site is difficult on the basis of this curve built for a training site. This is due to the fact that in this curve the information on the mutual distributions of the decisive feature for mines and clutter is mixed with the information on the *amount* of false-alarm generating objects present in the given lane.

The ROC curves built on the basis of (2.17) and (2.18) for the data shown in Figure 2.2 are plotted in Figure 2.3.

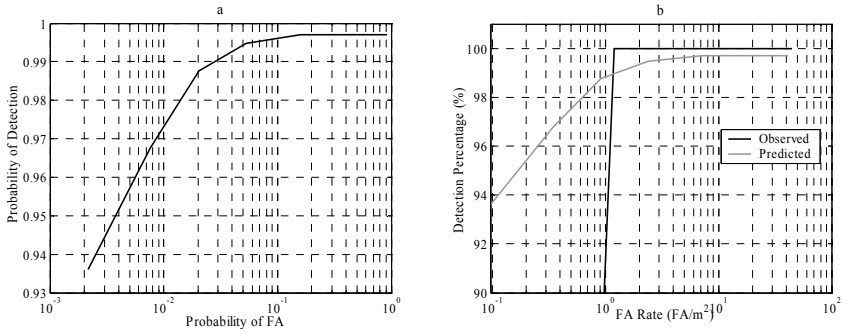

Figure 2.3 Probability-probability (a) and detection percentage-FA rate (b) ROC curves

The practical curve may be predicted from the theoretic one using appropriate scaling and mean density of false alarms. In this thesis the curves built according to (2.18) are used to characterize algorithm performances on training sites. The curves built according to (2.19) are used mostly on the training phase for building detectors.

The following scalar parameters are used in the literature to characterize how good a theoretical ROC curve is: area above the ROC curve and probability of FA corresponding to 0.996 probability of detection. The latter parameter is introduced straightforwardly for practical curves, while the former requires rescaling of the FA rate axis [70].

2.2 Feature Fusion Techniques

In this subchapter I introduce a feature fusion technique in application for the landmine detection using GPR. The subchapter covers the reconciliation of the individual detection maps and determination of a fusion rules to be applied to the reconciled map.

The feature fusion procedure is slightly different for the phases of training and testing. In the training phase the process consists of 3 main steps:

1. The detection lists following from the different measurement scenarios and DPS are reconciled. This means, that each detected location in the lists is associated with the locations in the other lists. The procedure is equivalent to a decision level fusion and is detailed in subchapter 2.2.1. It results in two sets of vectors representing the classes of target and clutter by features.
2. The random vectors resulting from the step 1 are described parametrically or non-parametrically. Possible ways for descriptions of feature vectors are briefed in 2.2.2.
3. Based on the descriptions obtained on the previous step Bayesian classifier is built. In practice linear or quadratic fusion rule is defined

based on the first two moments of the multivariate distributions. These steps are described in 2.2.3.

In testing phase steps 2 and 3 are omitted. The step 1 results in only one set of vectors. The separation of classes of target and clutter is made by application of the fusion rule defined in the step 3 of the training phase and comparing the result against a threshold.

2.2.1 Maps Reconciliation and Hard Fusion

A set of local coordinates must be imposed on the (training or testing) site and a linear mappings are established between it and each of the confidence maps. Once these preconditions are met, the confidence maps resulting from several measurements and/or several DPS can be reconciled. The process of reconciliation although technical by nature may present a significant challenge, as noted in [47, 50, 51, 55]. To resolve this challenge in my study I apply the following strategy.

The initial detection by LMD (2.5) applied to each of the confidence maps at hand, produces several detection lists. These must be reconciled resulting in the initially empty list of the reconciled feature vectors. The vector is filled according to the reconciliation algorithm depicted in Figure 2.4.

As a starting point in the reconciliation I define a hello radius R_H and a fusion $Rule$. The hello radius is a scalar defining the maximum distance between the coordinates of two detections found in two different confidence maps that allows to associate them to the same physical object. Introduction of the hello radius in necessary due to a) unavoidable imperfectness of the local $\leftrightarrow$ computer coordinate mappings and b) the fact that different measurement scenarios (MS) and DPS produce object images which maximum intensity varies in a range of several pixels. Throughout this Thesis I allow 3 cm hello radius, which is about the radius of the smallest target. The fusion $Rule$ is a number: $1 \le Rule \le P_D$. It defines the minimal amount of the detection lists in which any particular detection must be present in order to be retained in the reconciled list. Introduction of the $Rule$ makes the reconciliation process equivalent to the decision-level fusion. Obviously, setting the $Rule$ equal to P_D makes the reconciliation equivalent to the hard fusion where only the detections appearing in all MS and all DPS are retained. In the same time $Rule=1$ is equivalent to unconditional merging of the lists.

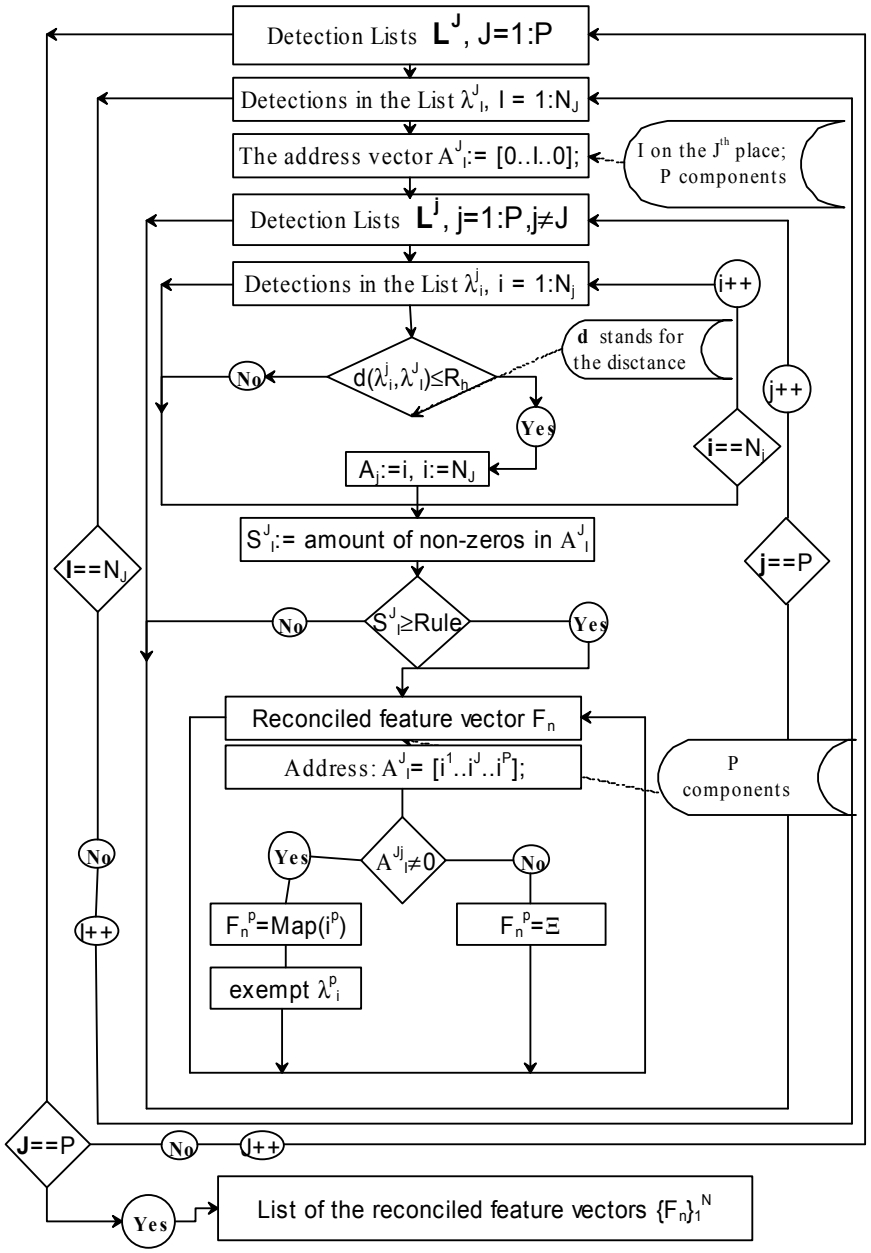

Figure 2.4 Algorithm of the reconciliation of confidence maps.

The core of the reconciliation process is wrapped in 4 nested loops, as it is seen from the Figure 2.4. Hence one starts with any one of the detection lists (arbitrary, $L^J, J \in \{1:P_D\}$) and for each detection l_I^J, $I = \overline{1:N_J}$ in this list forms an address vector $A^{JI} \in R^{P_D}$. The vector is zeroed except for the J[th] position, where the index I appears. One then checks whether or not a detection appears inside the hello radius in all other lists, $j = 1:P_D, j \neq J$. For each hit the address vector is updated by insertion to the j^{th} position the index of the detection in the corresponding list. Once all the lists are checked the quantity S of non-zero components of the address vector is compared against the *Rule*. If the *Rule* is surpassed the detection must be retained and the featuring detections discarded from the lists using their indexes. The retained detection is added to the list $\{F_n\}_1^N$ of the reconciled detections.

Definition of those elements of the resulting feature vector $F_n \in R^P$ that correspond to the confidence maps where a detection was found is straightforward. For the elements of the vector corresponding to maps in which the detection was not found virtual detection coordinates must be constructed:

$$(\xi, \gamma) = \underset{p=1:P}{mean}\{(x_p, y_p)\} \tag{2.20}$$

where (x_p, y_p) are the detections coordinates in those maps where the detections are present. Once (2.20) is established, the corresponding element of the feature vector is taken to be

$$\Xi^j = M^j(\xi, \gamma) \tag{2.21}$$

The procedure (2.20) – (2.21) finalizes the forming of the reconciled detection. The algorithm continues the loop by detections l_i^J found in the J[th] list until it is exhausted and then by the detection lists themselves. After all P lists are checked the retained vectors are supplemented with the additional features computed in the confidence maps as it mentioned in 2.1.2 and detailed in 4.2.

The described algorithm of maps reconciliation results in the list of detections represented by feature vectors. In this list all detections are represented by their optimally measured features. That is, all the features take the locally maximum values. Let P be the total number of the features used. Then each element of the list of reconciled detections can be treated as an independent observation $X \in R^P$. In the training phase certain amount of information must be inquired about the distribution of X knowing its class affiliation. In the testing phase the affiliation of X must be inquired on the basis of the knowledge gained in the training phase.

2.2.2 Parameters of feature vector distributions

The discussion in the previous subchapter resulted in the observation vector X associated to each location where a possibility for a target exists. This vector can

be treated as a random variable and thus can be described in terms of its probability distribution function

$$\Pi(f_1,..f_P)=\Pr\{x_1 \le f_1,...,x_P \le f_P\} \tag{2.22}$$

or its probability density function

$$\pi(f_1,..f_P)=\partial^P \Pi(X)/\partial f_1..\partial f_P \tag{2.23}$$

Just like in the 1D case treated in 2.1.4 the functions (2.22) or (2.23) must be estimated from the data measured in the training phase. A problem of mathematically sound description of these functions could be more difficult than mine detection per se. As it was discussed in the 1.2 no theory is available for adequate modeling of the behavior of at least some of electromagnetic-bound features peculiar to targets in an arbitrary medium. This generally prohibits parametric description of the multivariate feature distributions in the form of (2.22) or (2.23) for the case under consideration. In principle, the non-parametric approaches like kernel estimation techniques of (2.6)-(2.7) allow their expansion to *P*-dimensions. However, serious and often prohibitive difficulties arise as *P* grows. Firstly, the training set must grow significantly for the procedures to be effective. Secondly, technical problems of computation of high dimensional integrals may arise. And lastly, if the procedure of representation of the training site was successful, the effect of overtraining may arise due to which the performance on a test site becomes unpredictable.

On the other hand the moment parameters of the multivariate distributions can be easily estimated from the measured data without assuming any particular model. The following are the unbiased and consistent estimates [45] for centroids and covariances:

$$\mathrm{M}=\frac{1}{N}\sum_{k=1}^{N} x_k \tag{2.24}$$

$$S=\frac{1}{N-1}\sum_{k} F_k' F_k \tag{2.25}$$

where that $F_n \in R^P$ is a string-vector and therefore the product in (2.25) is a matrix. The parameters given by (2.24) and (2.25) are not enough to build Bayes classifier in general case but constitute sufficient data to build linear-quadratic classification (fusion) rules.

The quality of separation that might be achieved with these rules can be predicted with the use of the multidimensional analog of (2.16) with $\alpha = 0.5$ and (2.17) become Mahalanobis and Bhattacharyya distances given by:

$$F=\left(M^T-M^C\right)'\left(\frac{S^T+S^C}{2}\right)^{-1}\left(M^T-M^C\right) \tag{2.26}$$

and

$$B = \frac{1}{8}\left(M^T - M^C\right)'\left(\frac{S^T + S^C}{2}\right)^{-1}\left(M^T - M^C\right) + \frac{1}{2}\log\frac{\left|\frac{S^T + S^C}{2}\right|}{\sqrt{\left|S^T\right|\left|S^C\right|}} \tag{2.27}$$

respectively.

2.2.3 Linear and quadratic fusion rules

The solution of the problem of definition of the optimal classification of the random vector X on the basis of its probability density follows from the Bayes' theorem. This solution relays X to the class of either target or clutter on the basis of the likelihood ratio test [45]:

$$\ell\left(\vec{f}\right) = \frac{p_1\left(\vec{f}\right)}{p_2\left(\vec{f}\right)} \underset{H_1}{\overset{H_0}{\gtrless}} \frac{P_2}{P_1} \tag{2.28}$$

where ℓ is the likelihood ratio, $\vec{f} = f(X)$ is the feature vector, p_i are the a-posteriori and P_i are a-priori probabilities of X belonging to the i^{th} class. The a-priori probabilities are normally not known to us in the humanitarian demining and will be assumed equal to ½ unless specified differently. The discriminant function associated with likelihood test (2.28) is then defined as

$$-\log \ell\left(\vec{f}\right) = -\log p_1\left(\vec{f}\right) + \log p_2\left(\vec{f}\right) \underset{H_1}{\overset{H_0}{\gtrless}} 0 \tag{2.29}$$

These equations define the so-called Bayesian test for a minimum error, which also gives the optimal solution for our problem. But as it was stated above, we rarely possess adequate knowledge about the distributions p_i. Since our knowledge about these distributions is confined with its first two moments estimated from the samples, the fusion rule must be based solely on them. Such rule exists and is given by the following expression [45]:

$$\left(\vec{f} - M_T\right)' S_T^{-1}\left(\vec{f} - M_T\right) - \left(\vec{f} - M_C\right)' S_C^{-1}\left(\vec{f} - M_C\right) + \log\frac{|S_T|}{|S_C|} \underset{H_1}{\overset{H_0}{\gtrless}} \theta \tag{2.30}$$

where θ is a threshold. Moreover, this rule represents the Bayes solution itself in the case where both classes are normally distributed. If, further, the classes share the covariance $S_1 = S_2 = S$ the quadratic rule (2.30) reduces to the following linear one:

$$\left(M_T - M_C\right)' S^{-1}\vec{f} + \frac{1}{2}\left(M_T' S^{-1} M_T - M_C' S^{-1} M_C\right) \underset{H_1}{\overset{H_0}{\gtrless}} \theta \tag{2.31}$$

A linear rule can be also introduced for the case of unequal covariances: defining $S = 0.5(S_2 + S_1)$ one obtains linear Fisher mapping:

$$S^{-1}(M_2 - M_1)^T \vec{f} \underset{H_1}{\overset{H_0}{\gtrless}} \theta \tag{2.32}$$

If the rather restrictive condition of normality of both target and clutter classes is not held the quadratic rule defined by (2.30) becomes suboptimal. Moreover, if the corresponding distributions have significantly skewed marginals, the performance of this classifier may become unpredictable. In order to come up with a linear-quadratic classifier with reliably acceptable performance the maximum likelihood criterion is loosened and substituted with maximum deflection criterion [46]. Namely, setting in (2.15) $\alpha = 1$ one obtains a measure of the separation between the classes [13, 71]:

$$d(\alpha) = \frac{\left(\mu_1^T - \mu_1^C\right)^2}{\mu_2^T} \tag{2.33}$$

for which the optimal quadratic classifier can be built analytically. Assuming that one of the classes (say – clutter) is described by standard normal features ($\vec{f} \sim N(0, I)$) this classifier is given by [13]:

$$\vec{f}^T (S_T - I)\vec{f} + 2\vec{f}^T M_T \underset{H_1}{\overset{H_0}{\gtrless}} \theta \tag{2.34}$$

Note that $S_C = I$ and $M_C = 0$ in this case. A notable difference of (2.34) from (2.30) is that the covariance does not appear in the inverse form in the former. It also should be noted that the generality is not lost by imposing the $\vec{f}_C \sim N(0, I)$ requirement because each multivariate normal distribution with non-singular covariance may be whitened to this form [72]. The classifier (2.33) is suboptimal in general but coincides with the Bayes test if the statistics of the second class is exactly known [73, 13].

The expressions (2.29) – (2.33) define the toolkit for the construction of linear and quadratic classifiers, which have optimal or at least predictable performance when both or at least one of the classes to separate is distributed normally. However, the nature of the features obtained with (2.4)-(2.5) is such that their distributions rarely follow normal low. These distributions are skewed and their kurtosis varies not in the vicinity to 3. Thus for these methods to produce good results a technique of normalization the data must be found. These techniques are discussed below.

2.3 Feature normalization

2.3.1 Johnson's Transform

A method of normalization of a distribution of 1D data has been known in the statistical community during decades. Namely, a system of statistical distributions that covers all unimodal distributions, which are described with four or less parameters have been suggested by Norman L. Johnson in 1949 [52]. This system consists of 3 distinctive families of distributions each of which is connected to a standard normal distribution with its own transformation. These distributions fill a so-called squared skewness-kurtosis (KS) plane, which is illustrated in Figure 2.5.

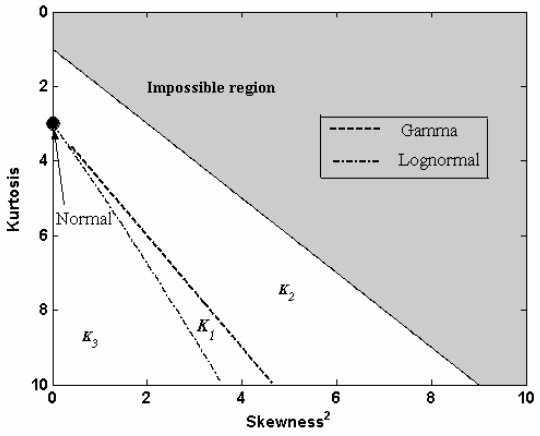

Figure 2.5 The squared skewness-kurtosis plane

Namely, as it can be seen from Figure 2.5 the log-normal line starts at (0, 3), which corresponds to no shift, and is drawn almost straightly downwards and to the right. Another example for the 3-parametric distribution is represented by the line corresponding to the gamma family. The line is described by

$$Kurtosis = 3(1+\frac{Skewness}{2}) \tag{2.35}$$

Those distributions, which have 4 or more parameters, cover whole regions in the plane. E.g. members of beta family lie in the region above the gamma-line and below $1+\text{Skewness}$ line. The latter line defines the limit for all possible distributions [74]. A normalization of the distribution in this context means its transformation to the shape, where its skewness is zero and its kurtosis is equal to 3. Distributions that meet these requirements are sometimes called 4^{th} order normal [71].

The 3 subfamilies of the Johnson's system lie in the KS plane on the sides of the log-normal line. The distributions lying above the line (such as beta family) are called bounded or S_B distributions. The distributions lying below this line are called unbounded or S_U distributions. Finally, the dividing line itself constitutes the third subfamily S_L. The standard normal distribution can be obtained from each of these distributions using a transformation of one of the three types [74]:

$$K_L = \alpha + \beta \ln(x - \varepsilon) \tag{2.36}$$

$$K_B = \alpha + \beta \ln \frac{x - \varepsilon}{\lambda + \varepsilon - x} \tag{2.37}$$

$$K_U = \alpha + \beta \sinh \frac{x - \lambda}{\varepsilon} \tag{2.38}$$

where, α, β, λ, ε are scalar parameters, and K_R , $R \in \{L, B, U\}$ is a transformation functional chosen in dependence of the region in the SK plane into which the distribution falls.

As a premise, the practical choice of the Johnson's normalizing functional requires the knowledge of the skewness and kurtosis of the distribution to be normalized. Sample estimates of these values are inadmissible to the task due to their biasedness and instability for small and medium sized datasets. Shaprio and Gross [74] provided an alternative technique that is based on the matching of percentiles of the measured data and of the standard normal distribution. The technique on selecting the Johnson's subfamily is given in Figure 2.6 in the form of a diagram. As it is seen from the figure, the method starts with calculating the percentiles of the given random data, which correspond to the values of a cumulative distribution of a standard normal variable. The latter is given by:

$$\Phi(z) = \frac{1}{\sqrt{2\pi}} \int_0^z e^{-\frac{t^2}{2}} dt \tag{2.39}$$

Taking an arbitrary $0 < z < 1$ and calculating $\Phi(-3z), \Phi(-z), \Phi(z)$, and $\Phi(3z)$ one obtains reference points for percentiles of the given data. Matching the percentiles $x_P(\Phi_i)$ one then obtains the discriminative parameters:

$$m = x_P(3z) - x_P(z), n = x_P(-z) - x_P(-3z), p = x_P(z) - x_P(-z), \tag{2.40}$$

which are used to form the discriminative ratio:

$$R_J = \frac{mn}{p^2} \begin{matrix} < \\ =1 \\ > \end{matrix} \Rightarrow \begin{cases} S_B \\ S_L \\ S_U \end{cases} \tag{2.41}$$

The ratio (2.41) provides zero probability for choosing the S_L system and in practice a tolerance is allowed when R_J does not diverge from 1 too much. This technique is proven in [74] to be stable and unbiased.

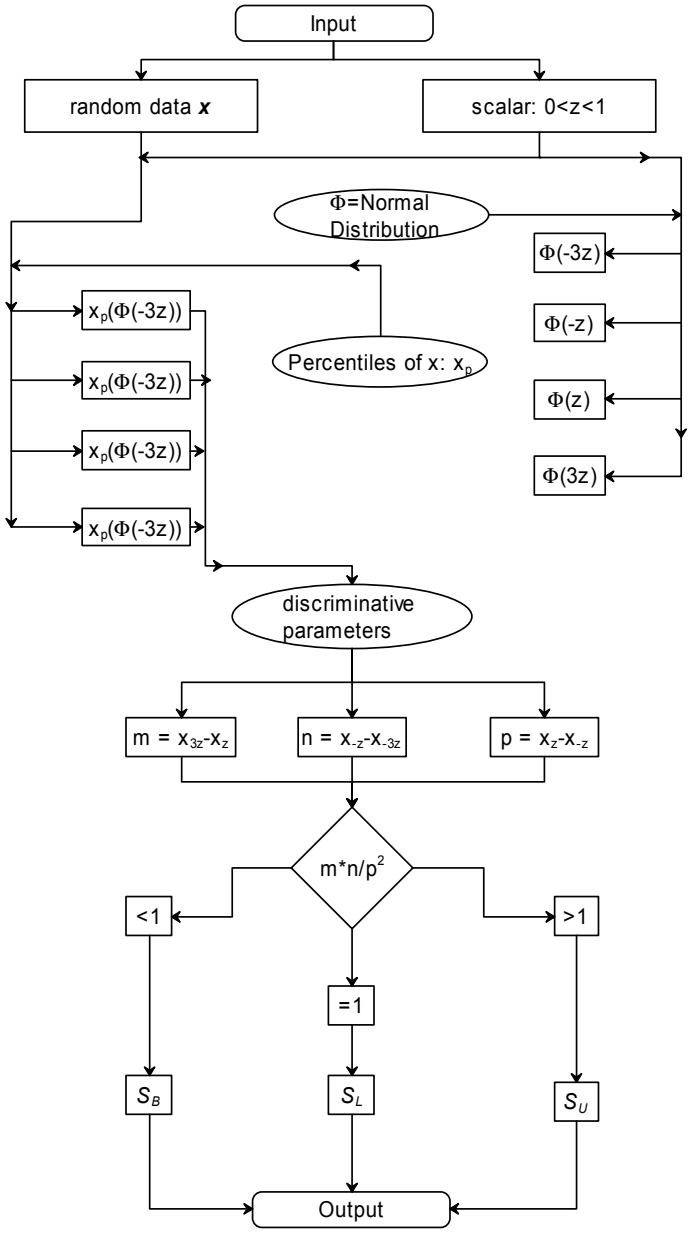

Figure 2.6 Procedure to determine the Johnson's subfamily

Once the family of the Johnson's distribution is selected from (2.41), its parameters can be estimated matching the percentiles of the measured data and the standard normal distribution. The following system of nonlinear algebraic equations arises when fitting the S_L subfamily:

$$Z_i = \alpha + \beta \log(x_i - \varepsilon), i = 1,2,3 \tag{2.42}$$

where Z_i is the inverse of the standard normal distribution function and α, β, and ε are the sought parameters of (2.36). The system (2.42) can be solved analytically for the case of specially selected percentiles: median and an arbitrary taken symmetric pair. In this case (2.42) is reduced to:

$$\begin{aligned} Z_{1-p} &= \alpha + \beta \log(x_{1-p} - \varepsilon) \\ 0 &= \alpha + \beta \log(x_{0.5} - \varepsilon) \\ Z_p &= \alpha + \beta \log(x_p - \varepsilon) \end{aligned} \tag{2.43}$$

which is solvable. The solution yields the following estimates:

$$\begin{aligned} \hat{\varepsilon} &= \frac{x_p x_{1-p} - x_{.5}^2}{x_p + x_{1-p} - 2x_{.5}} \\ \hat{\beta} &= \frac{Z_{1-p}}{\log\left(\frac{x_{1-p} - \hat{\varepsilon}}{x_{.5} - \hat{\varepsilon}}\right)} \\ \hat{\alpha} &= -\hat{\beta} \log(x_{.5} - \hat{\varepsilon}) \end{aligned} \tag{2.44}$$

The set of expressions (2.36) and (2.44) completely defines the transformation of a (quasi)lognormal distribution to the standard normal one.

For the case of S_B subfamily the procedure is ideologically same, but uses the explicit form of the density of the distribution and involves more algebraic transforms. The explicit form of the density is obtained from (2.37) and the following theorem about functionally transformed density [75]:

If Y is a continuous random variable, f(y) is its density function, and h(.) is a monotonic differentiable transform, then X=h(y) has distribution

$$g(y) = f(y)\left|\frac{dy}{dx}\right|, \tag{2.45}$$

provided that $|dx/dy| \neq 0$.

Application the theorem to (2.37) yields the following density for the S_B distribution:

$$g_B(x)=\frac{\beta\lambda\exp\left\{-\frac{1}{2}\left[\alpha+\beta\log\left(\frac{x-\varepsilon}{\lambda+\varepsilon-x}\right)\right]^2\right\}}{\sqrt{2\pi}(x-\varepsilon)(\lambda+\varepsilon-x)} \tag{2.46}$$

The parameters of the distribution (2.46) and thus of (2.37) are obtained matching the percentiles of the measured data and a standard normal distribution. Following from (2.46) four percentiles yield a system of 4 nonlinear algebraic equations for the selection of parameters α, β, λ, and ε. Again, the special selection of the percentiles to match, namely [-3z, -z, z, 3z], $0<z<1$, allows an analytic solution of this system. The solution provides the following estimates for the parameters:

$$\begin{aligned}
\hat{\beta}&=\frac{z}{\cosh^{-1}\left\{\frac{1}{2}\sqrt{(1+\frac{p}{n})(1+\frac{p}{m})}\right\}}\\
\hat{\alpha}&=\hat{\beta}\sinh^{-1}\left\{\frac{\left[\frac{p}{n}-\frac{p}{m}\right]\sqrt{\left(1+\frac{p}{n}\right)\left(1+\frac{p}{m}\right)-4}}{2\left(\frac{p^2}{mn}-1\right)}\right\}\\
\hat{\lambda}&=\frac{p\sqrt{\left[\left(1+\frac{p}{m}\right)\left(1+\frac{p}{n}\right)-2\right]^2-4}}{\frac{p^2}{mn}-1}\\
\hat{\varepsilon}&=\frac{x_z+x_{-z}}{2}-\frac{\hat{\lambda}}{2}+\frac{p\left(\frac{p}{m}-\frac{p}{n}\right)}{2\left(\frac{p^2}{mn}-1\right)}
\end{aligned} \tag{2.47}$$

The set of expressions (2.37), (2.39) where *p*, *m*, and *n* are the parameters are defined, and (2.46) explicitly defines the transformation of a S_B-distributed variable to the standard normal.

For the subfamily S_U the process of normalization follows the steps of the previous consideration. The probability density of this distribution is obtained using the same theorem:

$$g_U(x) = \frac{\beta \exp\left[-\frac{1}{2}\left\{\alpha + \beta \sinh^{-1}\left(\frac{x-\varepsilon}{\lambda}\right)\right\}\right]}{\sqrt{2\pi\left[\lambda^2 + (x-\varepsilon)^2\right]}} \tag{2.48}$$

and from it the following estimates are obtained analytically for the parameters of the transformation:

$$\begin{aligned}
\hat{\beta} &= \frac{2z}{\cosh^{-1}\left[\frac{1}{2p}(n+m)\right]} \\
\hat{\alpha} &= \hat{\beta} \sinh^{-1}\left[\frac{n+m}{2\sqrt{mn-p^2}}\right] \\
\hat{\lambda} &= \frac{2p\sqrt{mn-p^2}}{(m+n-2p)\sqrt{\frac{m}{p}+\frac{n}{p}+2}} \\
\hat{\varepsilon} &= \frac{x_z + x_{-z}}{2} + \frac{p(n-m)}{2(m+n-2p)}
\end{aligned} \tag{2.49}$$

The derivations given above complete the Johnson's method of transformation of an arbitrary unimodal 4-parametric distribution to the standard normal one. This theory will be used for normalization of the data prior to the application of linear-quadratic classifiers as it is described in the next subchapter.

2.3.2 Pseudo-normalization of the clutter distribution

As it was discussed in subchapter 1.1, performance of linear and quadratic classifiers (2.30)-(2.32) is guaranteed only if both classes of target and clutter are described by normal distribution. If this condition is not met the classifiers may perform poorly or break down altogether. On the other hand, performance of the maximum deflection quadratic classifier (2.34) is guaranteed if just one of the classes (say clutter) is described by the standard normal distribution. Distributions of the elements of feature vectors, which are obtained in measurements, are often non-normal for both classes. The use of Johnson's family of distribution techniques discussed in 2.3.1 allows the transformation of arbitrary 1-D distributions to the standard normal one. These transformations applied independently to all features that constitute the feature vector result in a multivariate distribution whose marginals are normal. This does not guarantee that the distribution of the feature vector X becomes multi-normal unless the features can be considered independent. One cannot guarantee independency of the features and the next best thing is to

guarantee that they are not correlated. A linear transformation yielding this called whitening is widely known. It is given by [72, 45]:

$$X_W = \Lambda^{-\frac{1}{2}} \Psi X \tag{2.49}$$

where Λ is a diagonal matrix having the eigenvalues of the covariance of X on the diagonal and Ψ is a matrix consisting of the corresponding eigenvectors.

Let

$$\widetilde{X}_c = \begin{pmatrix} \widetilde{x}_1 \\ \dots \\ \widetilde{x}_P \end{pmatrix} = \begin{pmatrix} K_{1_i}(x_1, \pi_1) \\ \dots \\ K_{P_i}(x_P, \pi_P) \end{pmatrix} \tag{2.50}$$

be the result of independent feature normalization of (2.36)-(2.38) applied to the class of clutter. In (2.51) K_{j_i}, $j=1:P$, represents corresponding normalizing functional, and π_j are vectors of their parameters obtained via (2.44), (2.47), or (2.49). Then applying (2.50) to $\widetilde{X}_c$ (using the correspondingly computed Λ and Ψ matrixes) one obtains vector X_c^N, which components are normal and non-correlated. In training phase these vectors constitute the clutter class. Computing its centroid and shifting it accordingly one obtains a class described by a zero-mean non-correlated distribution, whose all marginals are normal. Then the same transformations with the same parameters are applied to the vectors representing the class of target. If the features constituting the feature vector can be treated as independent variables, the performance of the maximum deflection classifier (2.34) is guaranteed. In any case, the un-skewness of the marginals of the resulted distributions improves the performance of the detector in comparison to non-transformed case.

In practical realization of the approach only the parameters λ and ε that define the shape of the transformed marginals must be estimated. At the same time the parameters α and β defining spread and centrality of already normalized distributions may be taken 0 and 1 respectively as they are redefined during the whitening (2.48).

This situation is illustrated in the Figure 2.7 and Figure 2.8 where a real data examples are shown. The data used in the example had been acquired during a mine detection testing campaign [77] with the video-pulse GPR of IRCTR. For the sake of representability I restrict the feature vector dimensionality with two scalar values corresponding to a pair of mutually orthogonal polarized receive channels, each processed with its own processing scheme (these data processing schemes are detailed further in the thesis). The subfigure a) of the Figure 2.7 represents their 2D distribution. Their marginals are given on the sides of the subfigure as normalized histograms. The skewness is equal to {8, 14} for the clutter and {42, 58} for the target classes respectively. The significance of the skewness of the data distribu-

tion is evident from both these values and the histograms shown in the figure. The kurtosis vectors are equal to {3.7 3.4} and to {9.5 9.2} for the clutter and target respectively.

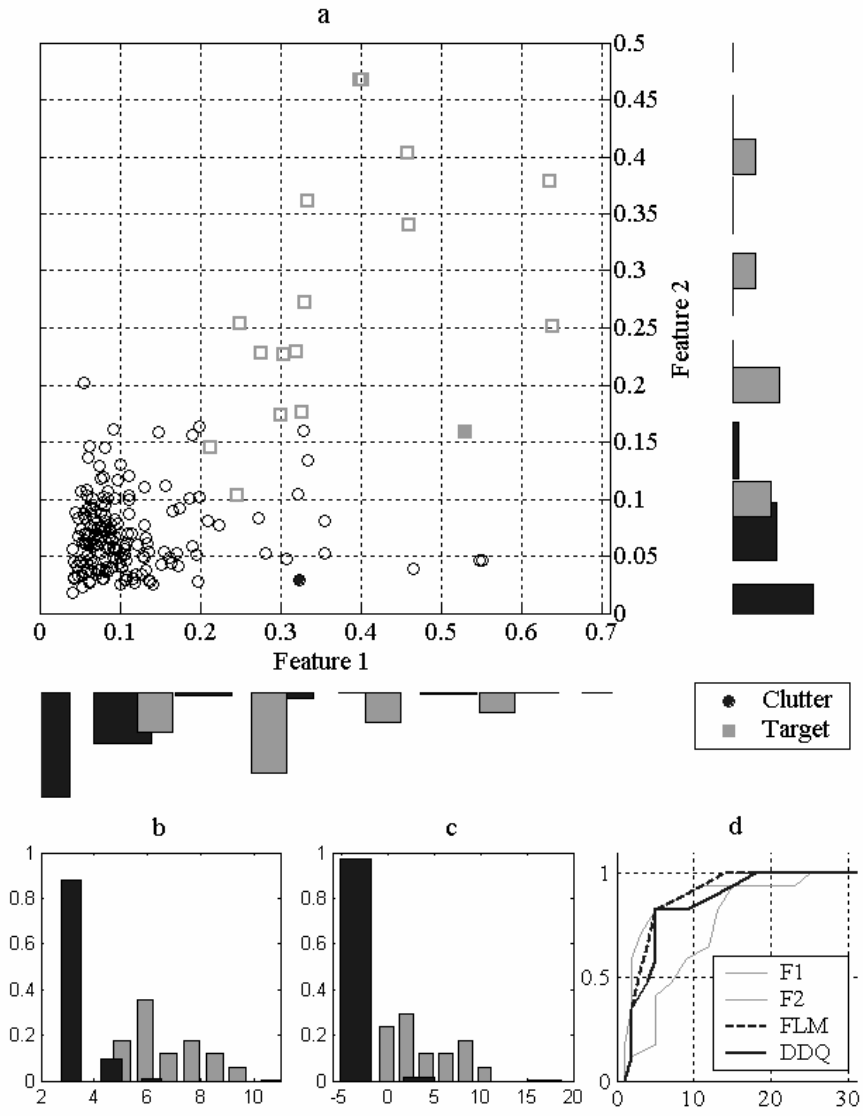

Figure 2.7 Application of the quadratic classifier to the real data represented by two features: a) scatter plots of the classes with marginals on the sides, b) distribution of the decisive feature resulted from the linear fusion, c) distribution of the decisive feature resulted from the quadratic fusion, d) the ROC curves

As it is seen these distributions cannot be reasonably approximated with the normal low. It does not come as a surprise then that applying the fusion techniques (2.32) and (2.34) do not produce a significant improvement in separation of the classes. This is illustrated in the subfigures b) and c) where the normalized histograms for the fused features describing the classes of target and clutter are shown. Finally, subfigure d) presents ROC curves built for the individual and fused by the way of (2.32) marked as Fisher linear mapping (FLM) and (2.34) marked as decorrelated distance classifier (DDQ) features. The fusion performance is suboptimal as the curves corresponding to the fused features mostly run in between the ones corresponding to the individual detections. Fused features in this case never surpasses the performance of the better of the individual features.

On the other hand the data normalization applied to this dataset improves the target detectability as it is shown in Figure 2.8. In this particular case the normalizing functional K_1 was found to be acceptable. Its application resulted in diminishing of the skewness of the distributions of the decisive features for the clutter to {0.6 0.4} and for target to {0.3 -0.3}. The un-skewness of the transformed data can be seen from these values. In the same time the kurtosis vectors were moved to {3.6 5.2} for the clutter and to {2.2 2.3} for the target. Not all 4 of the values are close enough to 3 and therefore the optimal threshold in (2.32) and (2.34) cannot be estimated from the ML criterion. Nonetheless, the classification results sufficiently improve for both classifiers as it can be seen from Figure 2.8.

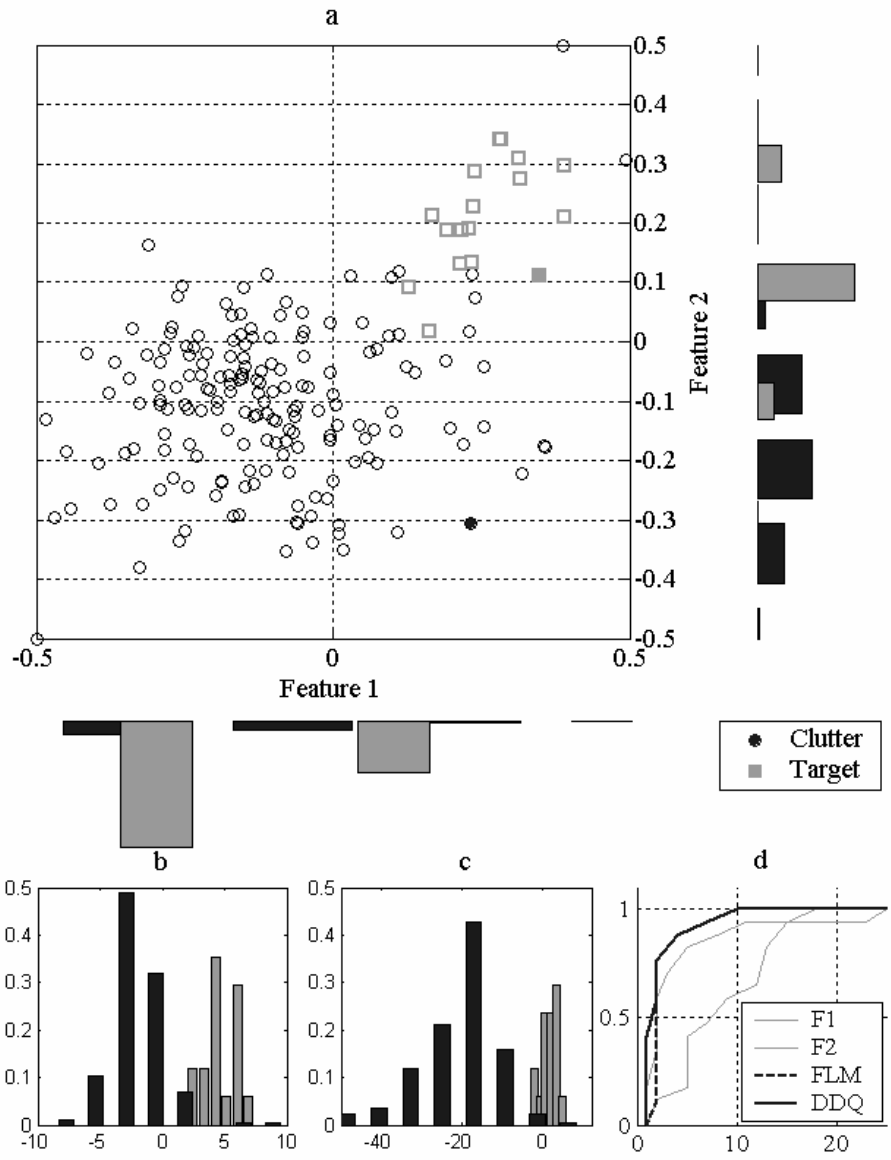

Figure 2.8 Application of the quadratic classifier to the real data represented by two features after clutter normalization: a) scatter plots of the classes with marginals on the sides, b) distribution of the decisive feature resulted from the linear fusion, c) distribution of the decisive feature resulted from the quadratic fusion, d) the ROC curves

2.3.3 Simultaneous pseudo-normalization of the distributions of target and clutter classes

As it was discussed in 2.2.3, the maximum deflection classifier is suboptimal to the maximum likelihood one. The latter allows a linear-quadratic form (2.29) if both classes of target and clutter are described by normal distribution. In previous subsection we discussed results of pseudo-normalization of one of the classes not imposing any demands on the other one. In these conditions the best MD classifier performed well in most cases. If we, however, want to use the optimal maximum likelihood classifier, the classes must be pseudo-normalized simultaneously.

Suppose that $f_C(x_j)$ and $f_T(x_j)$ are the densities of a j^{th} feature x for the clutter and target respectively. Separately applying the procedure shown in Figure 2.6 to these densities and not allowing any tolerance we can come to only two different results: either both densities can be approximated by one of the S_B or S_U families, or one of the densities belongs to the S_B and another to the S_U. In the former case we check how far the R_J ratio deviates from unity for both classes. If the deviation is outside of the tolerance limits we fit the parameters of the relevant distribution. If the opposite is the case or if the densities belong to the different subfamilies the attempt to fit the S_L subfamily is made. The procedure is outlined in the diagram in Figure 2.9.

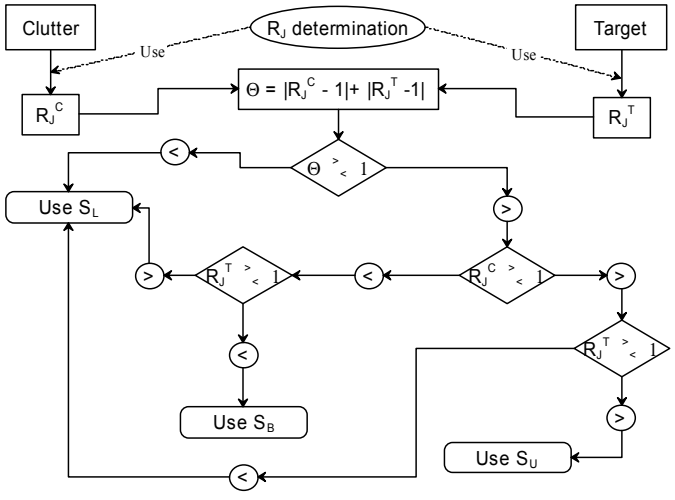

Figure 2.9 Selection of the subfamily for simultaneous pseudo-normalization

Contrary to the case considered in the previous subchapter, in the case under consideration the normality for the output cannot be guaranteed. An attempt to ensure the un-skewness and normal shoulders of the output is made instead. To this end the following goal functional is defined:

$$G(\pi; f_C, f_T) = a_1\{Sq[K_*(f_C, \pi; x)]\}^2 + a_2\{Sq[K_*(f_T, \pi; x)]\}^2 + a_3\{Kr[K_*(f_C, \pi; x)] - 3\}^2 + a_4\{Kr[K_*(f_T, \pi; x)] - 3\}^2 \quad (2.52)$$

where *Sq* and *Kr* are skewness and kurtosis as defined by (2.12) and (2.13) respectively, K_* represents the normalizing functional, π is the vector of the paramers, and a_i are weights. The weight are chosen to account for the fact that (2.52) operates with the sample estimates of the skewness and kurtosis and the estimates of the latter are much less stable. We have to find the optimal parameres π minimizing (2.52):

$$\pi = [\alpha, \beta, \lambda, \varepsilon] = \arg\min G(\pi; f_C, f_T) \quad (2.53)$$

Again, the parameters α and β are taken as 0 and 1 respectively and only the shape-parameters λ and ε must be found from (2.53). They are varied in an elliptical vicinity of $(\hat{\lambda}_C, \hat{\varepsilon}_C)$ and $(\hat{\lambda}_T, \hat{\varepsilon}_T)$, which are defined from (2.47) or (2.49) depending on the form of the functional. The case where the S_L functional must be fitted is the easiest since only one parameter ε is varied.

Once the optimal parameters are determined, the simultaneous digitalization procedure is applied to the clutter and target classes. Namely, the training set corresponding to the clutter is transformed analogously to (2.50)-(2.51), and then additional orthonormal transformation is applied to de-correlate the target class:

$$\widetilde{X}_C = \Psi_T' \Lambda_C^{-\frac{1}{2}} \Psi_C X_C$$
$$\widetilde{X}_T = \Psi_T' \Lambda_C^{-\frac{1}{2}} \Psi_C X_T \quad (2.54)$$

where as in (2.20) Ψ_* are the matrixes of eigenvectors of the covariance matrixes of clutter and target respectively and Λ_C is the matrix of the eigenvalues of the clutter covariance. Transformation (2.54) results in $S_C = I$ and $S_T = \Lambda_T I$, where Λ_T is the diagonal matrix of the eigenvalues of the target covariance. As a last step in the whitening process the centroid for the clutter is computed and both classes are compensated for it.

The quadratic and linear classifiers (2.31) and (2.33) then become:

$$\sum_{i=1}^{P} \sigma_i^T \left[\widetilde{x}_i - (\mu_1^{T_i} - \mu_1^{C_i})\right]^2 + \|\widetilde{x}\|^2 \underset{<}{\overset{>}{}} \theta \quad (2.55)$$

$$\sum_{i=1}^{P}\left(\frac{2}{1+\sigma_i^T}\right)\left(\mu_i^{T_i}-\mu_i^{C_i}\right)\tilde{x}_i \begin{matrix} > \\ < \end{matrix} \theta \tag{2.56}$$

respectively, where $\mu_1^{Q_i}$ are components of the centroid vectors of the transformed and whitened classes of target and clutter, and σ_i^T are the eigenvalues of the target covariance. If the transformation defined by (2.51) provides the distributions that are un-skewed and have 'normal shoulders', and features constituting the feature vector can be treated as independent variables, the performance of the classifiers (2.55) and (2.56) is guaranteed.

2.4 Conclusion for Chapter 2

In this chapter I have discussed the statistical approach to mine detection that will be used throughout this Thesis. We defined the general data processing scheme shown in Figure 2.1 and described the main steps of this scheme. We have shown the procedures leading to creation of confidence maps and initial detection in them. Then the algorithm of maps reconciliation has been suggested; the algorithm ultimately results in the list of P-dimensional observations. The task is then reduced to the binary hypothesis testing, which is solved by statistical inference techniques. These techniques and linear and quadratic detectors to which they reduce in the case of normality of observation have been discussed. Since the observation as they are obtained here are unlikely to produce normally distributed features outright, I discussed two different procedures to mitigate the problem of non-normality. I also established the criteria by which the results of mine detection will be judged. These include two distinctive types of ROC curves and parameters associated to them.

The following aspects of the above considerations are novel (in order of appearance):

- Multiple scenarios of data acquisition, data processing, and feature formation are combined in a single the data processing scheme
- Local maxima based detector.
- Improvement of the performance of quadratic classifiers via simultaneous pseudo-normalization of features for classes of target and clutter application with use Johnson's transformation

The chapter results in an open concept of a statistically based mine detection. Virtually any type of observation may be added to it provided that the training of the observation-based technique can be made on the same training data and its features form a confidence map.

The following questions remain open and are treated in the consequent chapters: clutter suppression, aspects of better confidence maps, reduction of dimensionality and cases when features are known to have functional-statistical connection beyond the second moment.

Chapter 3 Waveform Based Clutter Suppression Algorithms

As it was discussed in subchapter 1.1, most of APMs are very weak scatterers and their radar response is often masked by clutter. This is true due to their small size, low metal content and low dielectric contrast with dry soils. Therefore meeting the 99.6% detection rate set as a standard for the humanitarian demining is either impossible or leads to unacceptably high rate of false alarms (FA). The situation is somewhat improved using several features and/or several data acquisition and processing scenarios followed by feature fusion. The approach based on this idea is described in Chapter 1. As it was mentioned there, the step of clutter suppression is necessary in any data processing scheme.

As discussed in the Introduction (subchapter 1.2) the mainstream approach for the clutter suppression is definition and removal of a background signal. This approach does indeed help to reduce false alarms rate but often leaves it unacceptably high. The main reason is that any localized object is counted as detection by such algorithms. In this chapter I present a distinctively different approach based on the target model. Clutter suppression algorithms based on it may operate in conjunction with the background removal and focusing algorithms producing significant reduction of the FAR.

3.1 Target response waveform as a feature

Generally, there are two distinctive approaches to the problem of landmine signature detection in clutter. In the first approach a background model is defined and all objects, which significantly deviate from this model, are detected as targets. These approaches were briefly described in the Introduction (subchapter1.2.1). The mainstream method for the background/object dichotomy in this approach is a statistical binary hypothesis testing: the detection is called when the background hypothesis must be rejected. This approach allows development of real time causal algorithms but has a significant drawback: any localized scattering object (not only a target) results in a detection declaration thus inflating a FA rate. The output of this type of the algorithms can be described as a GPR dataset without background. The separation between targets and friendly objects should be made in further processing.

Within the second approach a target model is defined and then looked for in the GPR data. In 3D GPR data (C-Scans) object's radar returns show up as hyperboloid-like traces. The features associated to each particular object are spread in the C-Scans along these traces. The signal processing within the second approach uses a target's feature vector for the target detection. As it was discussed in the introductory chapter, the algorithms of this type result in detection lists analogous

to ones described in subchapter 2.1. The algorithms of this type are successful when they provide at their output significant separation of clutter and target classes. The separation can be measured by any of the means described in subchapter 2.1.4.

In this chapter I present a set of novel clutter suppression/target detection algorithms based on the target model approach. The generic algorithm operates as a two-stage signal processor after the background removal and prior to SAR focusing. In the output A-Scans it marks target responses with sharp monocycles. In C-Scans it preserves the hyperboloid-like traces left by targets in 3D data and thus its output is well suited for SAR processing. The SAR or another technique that uses spatial distribution of the features is supposed to be applied to the data after the processor. As a target detecting feature the algorithm uses a local similarity between a predefined reference wavelet and a part of an A-Scan under test. The measure of similarity is calculated on the first stage of the processing and its deviation from the expected score is penalized on the second stage. The reference wavelet is a representation of a target response to the probing radar pulse and is derived from a set of data acquired in controlled environment conditions.

The two most important features of the algorithm are: it tolerates certain changes in the target responses caused by variations of targets and environment, and it discards the energy information from the input A-Scan under test. The former feature increases the robustness of the algorithm, allowing for its usage for the data acquired in somewhat different conditions using the same reference wavelet. The latter one equalizes the responses from mines of different sizes and depths of placement and suppresses the influence of some very strong sources of clutter, like pieces of shrapnel or barbed wire. These two features distinguish the proposed algorithm from the normalized cross-correlation and determine its novelty.

The suggested algorithm relies on the assumption that the resemblance between the once-determined reference wavelet and target responses is held from target to target in certain environment conditions. Waveform consistency of target returns has been observed empirically by the author while analyzing data acquired during three measurement campaigns [77, 79, 80] at two different sites. A theoretical base for the observed consistency can be found e.g. in [53] where the response from a dielectric cylinder target is analyzed.

Although the formulations given in [53] provide the basic means for the modeling of the expected target responses, accurate and robust modeling of the mines under different soil and radar conditions is difficult [12, 13]. Thus I rely on the presence of the training site for derivation of the algorithm parameters. I use a training dataset measured in the controlled environment conditions to obtain the reference wavelet and the parameters of the penalty functional of the processor. By the controlled environment I mean a portion of a minefield where the positions and parameters of the mines are known exactly and soil conditions can be closely inferred. I demonstrate that the reference wavelet and penalty functional built at such

training site can be successfully used for detecting the antipersonnel mines of the same or very similar shape/composition in the data acquired over a site with similar but not the same soil properties and radar conditions.

I include the new algorithm as an additional processing step into a baseline data processing and object detection scheme discussed in 2.1. In this case the scheme consists of background removal, SAR focusing, construction of a confidence map, and automated detection. The algorithm is inserted into this scheme before the SAR focusing. The performance of the data processing schemes is measured both in terms of ROC curves and segregation of target and clutter classes they offer.

The rest of the chapter is organized in the following way. The core concept of the algorithms, the local similarity measure is introduced further in the subchapter 3.1, the penalty functional concept is discussed in subchapter 1.1, the superposition (as opposed to sequence) of the algorithm with SAR focusing is given in subchapter 3.2.

3.1.1 Amplitude of APM responses to GPR probing pulse

As it was mentioned above, the clutter objects are bright in comparison to the target we are trying to detect. Moreover, the scattering by APM is often difficult to detect in presence of the direct wave of the radar and even surface roughness. A quantitative analysis of the signal to clutter ratio typical to several radar scenario have been made in [76]. The data have been acquired during a Joint Measurement Campaign of IRCTR and TNO DS&S [77] (see the detailed description of the campaign in the Appendix 0) held at the Waalsdorp facilities for demining equipment [78]. It is assumed that the clutter for an object is any signal, which is not related to the object's own scattered field, present in the vicinity of the object's response. From this perspective the clutter level depends on the way the object response is observed. For example, the clutter level for B-Scans is defined as the maximum peak-to-peak magnitude of parasite signals in the vicinity of object's responses in the B-Scan [76]. Main peak-to-peak magnitude ratios of target responses to the clutter defined above way are shown in Figure 3.1 for dry and wet sand and quasi-monostatic and bi-static radar scenarios[1]. Descriptions of the mines measured in this experiment can be found in the Table B.2 and Table B.3 of Appendix B .

Figure 3.1 a) represents ratios of the magnitudes of mine responses to the clutter for the dry sand. It can be seen that the bi-static channel has larger values of the object response. This is due to the fact that these receivers are placed aside of the

[1] The antenna configurations are indicated as m for mono-static and b for bi-static scenarios in legends of the figure.

main beams of the transmitter and thus have the lower value of the magnitude of the direct wave, which is a main source of clutter in this situation. According to the expectations the maximum values are produced by the relatively large PMN-2mines. The magnitudes of the responses of very shallow buried mines are the lowest because of the strong influence of the ground reflection in this time window. The wavelets caused by local inhomogeneities are involved in (2.3), which decreases the magnitude of the responses. However, responses of all mines are well inside the dynamic range of the radar, which is 82 dB [29].

The signal/clutter ratios for the wet sand scenario evaluated for the given above definition of the clutter produced the results shown in subfigure b). As it can be seen from the figure, the general trend remains the same as the flush buried mines are the most difficult to detect. Again the dynamic range of the radar allows detection of all targets.

The detection of the mines placed in the grass lane is even more difficult. Due to the structure of the soil with vegetation on it there are plenty of week scatterers, which sometimes embarrass detection of the objects. Moreover, the soil in places, in which the mines had been buried, is significantly disturbed, which also sometimes embarrasses detection of the mine response itself. The subfigure c) represents magnitude ratios of the target responses in these conditions.

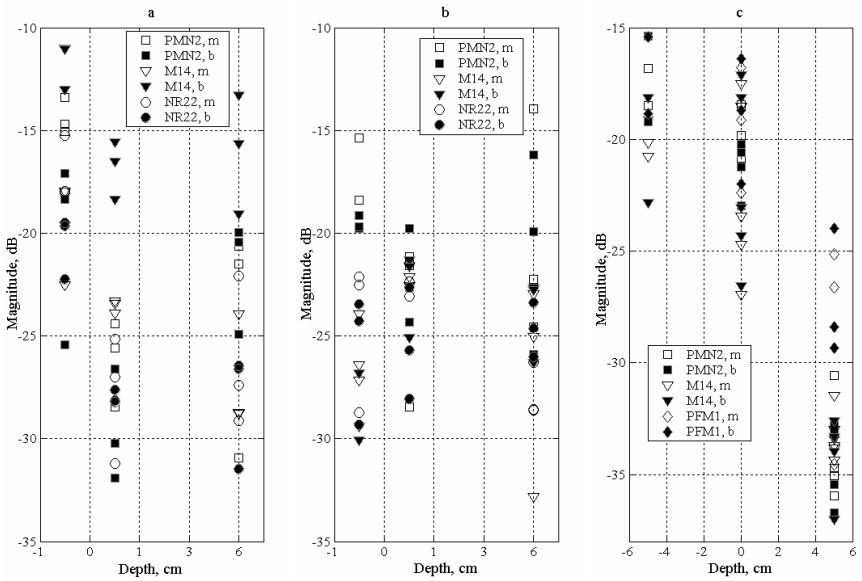

Figure 3.1 Peak-to-peak magnitude ratio of target responses to the direct wave of the radar, dry sand a), wet sand b), grass c)

As it visible from the graph the largest values correspond to the PFM1mines, which contain significant amount of metal. Again, bi-static antenna configuration provides higher signal to clutter ratio. The lowest energy returns in this case are observed for the deeper mines rather than for the flush buried ones. This attributes to the fact that the hosting medium in this experiment has higher losses and the effect of these losses is stronger than the effect contamination of a background signal with target response peculiar to the flush buried mines.

The above analysis shows, that the responses of APM are very week indeed in comparison to most other electromagnetic phenomena recorded during the measurements. Therefore the main ambition (and in the same time difficulty) is to find a feature, which distribution for the target class is energy independent. Moreover, the distribution of the ideal feature for the class of targets should be a) compact and b) shifted from the distribution for the class of clutter. If such a feature is identified, the data can be transformed in such a way, that only the objects exhibiting it would be underlined, while the rest of objects suppressed. If successful, this type of clutter suppression – to the contrary of background model – would allow suppression of the clutter associated with compact objects.

3.1.2 Shape of APM responses to GPR probing pulse

It has been observed by the author during analysis of the data collected over several test sites that the responses of plastic cased antipersonnel mines of certain types, namely PMN2, M14, and NR22, are represented in raw A-Scans by very similarly shaped wavelets [79]. These wavelets while retaining a similar shape differ from each other primarily in magnitude. The latter depends on the type of the mine, depth of its placement and type of the hosting soil. Similarity of mine responses may be explained theoretically on the basis of the following impulse response operator of a cylindrically shaped dielectric target [53]:

$$H(t) = -\frac{v_t^{\,eff}}{4\sqrt{\pi}c^2}\Delta\varepsilon_r S_{xy}\left(\dot{\delta}(\tau_1) - \Gamma\dot{\delta}\left(\tau_1 - \frac{2l_{trg}}{v_t^{\,eff}}\right)\right) \tag{3.1}$$

In (3.1) $v_t^{\,eff} = v_t^{\,eff}\left(\varepsilon_r^i, \varepsilon_r^e, l_{\mathrm{trg}}\right)$ is an effective target velocity (the entity introduced in [53] to describe the speed at which the electromagnetic wave propagates in and around target); $\Delta\varepsilon_r$ is the target/soil contrast, S_{xy} is the target cross-section (a circle here), τ_1 is the time delay corresponding to the turnaround travel time to the top of the mine, Γ is attenuation constant, l_{trg} is the target height, and $\dot{\delta}(\cdot)$ is a derivative of a delta function, hence the derivative operator. Given that the interiors of the PMN2, M14 and NR22 mines are similar (TNT and possibly a small metal pin), the waveform resulting from application of $H(t)$ to a probing pulse is

determined by the height of the cylindrical target, permittivities of the hosting medium and the target, and the bandwidth of the probing signal.

The probing pulse of the IRCTR GPR operating with 0.5 ns generator is shown in Figure 3.2.

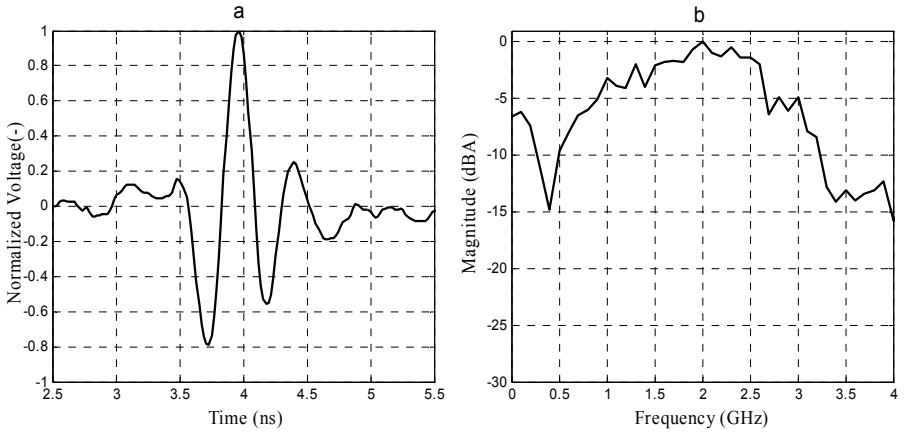

Figure 3.2 The probing pulse of the radar: a) the wavelet, b) the spectrum magnitude

As mentioned in the subchapter 1.1.3, the probing pulse of has a triplet shape with an approximate duration of 0.9 ns and possesses a 2.8 GHz bandwidth on 10dB level spanning from ~0.5 to ~3.2 GHz. Referring to the Table B.1 in the Appendix B one can see that while the diameters of the PMN2, M14, and NR22 mines vary (12, 5.8, and 5.2 cm respectively), they indeed retain cylindrical shape and their heights fluctuate only within a range from 4 for M14 to 5.5 centimeters for NR22.

The responses of these mines to the radar probing pulse modeled using (3.1) are shown in Figure 3.3 a). As it can be seen from the figure the probing pulse with 3GHz bandwidth does not result in a significant difference in the response wavelets of the cylindrical objects, which heights vary in the range from 4 to 5.5 cm. The actual A-Scans taken over the tops of the PMN2, M14, and NR22 mines are shown (after background removal) in Figure 3.3 b).

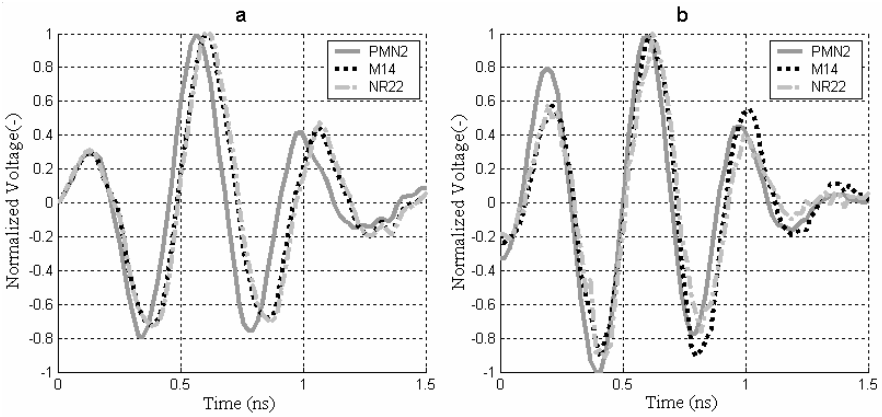

Figure 3.3 The responses of the PMN2, M14, and NR22 mines to the probing pulse of the radar: a) modeled, b) measured

It can be seen from the figure that the actual measurements correspond well to the prediction of a rather simple model (3.1): both the shapes of the responses and their similarity for the different mines are confirmed.

The observed consistence of the mines signatures provides an exploitable feature. It is possible now to construct an algorithm, which would successfully reject reflections of objects having different geometry and/or scattering mechanism irrespective to their reflection magnitudes. To this end a relevant measure of similarity must be introduced to quantify the similarity between an A-Scan under test and a target.

3.1.3 Similarity Measure

A well-established measure of similarity between an input signal $u(t)$ and a reference $h(t)$ is given by their cross-correlation:

$$X[t;u,h]=\int u(t-\tau)h(\tau)d\tau \tag{3.2}$$

It can be seen from (3.2) that the cross-correlation linearly depends on the amplitude of the input signal $u(t)$. However, in our case neither the amplitude of a signature nor its energy represents a feature, which could help in discrimination of a target from clutter. A normalization of the input via

$$u_N=\frac{u(t)}{\|u(t)\|_\infty} \tag{3.3}$$

does not discard the energy information from (3.2) since it is made to the highest amplitude in an A-Scan. That is the output (3.2) depends on the amplitude ratio between the object wavelet and the clutter present in the signal. The normalized correlation [81], which is commonly used in pattern recognition and is given by

$$X_N(t) = \frac{\left|\int h(t)u(t-\tau)dx\right|^2}{\left|\int u(t-\tau)Supp(h(x))dx\right|^2 \left|\int h(x)dx\right|^2} \tag{3.4}$$

does not discard the energy content either, since again the normalization is done outside of the integration.

To overcome this difficulty we introduce here an alternative measure of similarity i.e. Local Similarity Measure (LSM) between the input A-Scan and the reference wavelet:

$$L[t;u,h] = \int (\hat{u}(\tau;t) - h(\tau))^2 \, d\tau \tag{3.5}$$

where $h(t)$ is again the reference waveform (its selection is discussed below) and $\hat{u}(\tau;t)$ is windowed and normalized version of the input:

$$\hat{u}(t,\tau) = \frac{u(\tau)}{\max\limits_{t-d<\tau<t+d}\{|u(\tau)|\}} W(\tau;t,d) \tag{3.6}$$

In (3.6) $W(\tau;t,d)$ represents a rectangular window of width *d* centered on the moment *t*:

$$W(\tau;t,d) = \begin{cases} 1, & t - \frac{d}{2} < \tau < t + \frac{d}{2} \\ 0, & otherwise \end{cases} \tag{3.7}$$

The width *d* of the window in (3.6) and (3.7) is chosen to coincide with duration of $h(t)$. As it can be seen from (3.5) - (3.7), the LSM calculates for each time moment t the Euclidian norm of the difference between a portion of an input A-Scan centered on this moment and normalized to its maximum and a reference waveform. Therefore, the LSM marks the presence of a wavelet similar to the target signature with a close to zero value and takes arbitrary positive values elsewhere. Note that for each moment *t* the LSM $L(t;u,h)$ is computed for the portion of an A-Scan normalized by (3.7) and centered at the moment *t*. In this way the normalization is performed inside the integral comparison of the shapes and thus the energy-bound information is totally discarded at least in noiseless situation.

The input and output of the first stage of the algorithm, where the LSM is computed, are illustrated in Figure 3.4 for two different mines: surface placed PMN2 (a) and 6 cm deep buried M14 (b). The first case is characterized by a high value of signal to clutter ratio (SCR) and this mine is easy to detect with any conventional method. In the second case negative SCR prevents from detecting the M14 mine on the energy basis. The Figure 3.4 shows the A-Scans (after removal of the ground bounce) acquired over a top of the mines and their LSM scores to same predetermined reference wavelet. The positions of the mine signatures in the input

A-Scans are marked by arrows and the inlet shows the reference wavelet $h(t)$. As it can be seen from this figure, the presence of the target signature is indeed marked by global minima of their corresponding LSM score.

The clutter wavelets present in the input A-Scans are also marked by local minima. Their values differ from those of interest and they must be suppressed during the second stage of the processing.

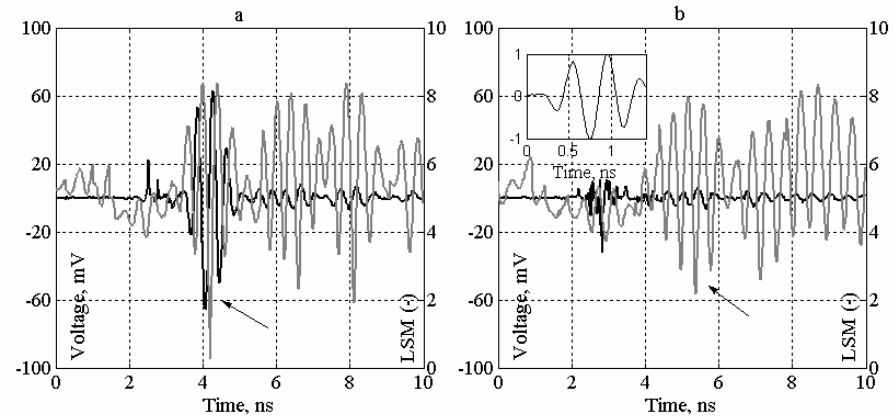

Figure 3.4 A-Scans (darker lines) acquired at the tops of a PMN2 (a) and M14 (b) mines and their LSM scores to the same reference wavelet given in the inlet in subfigure b; mine response positions are marked with arrows

To this end the range in which the LSM scores of the objects of interest are expected to take values must be found. This prediction for the mines having slightly different heights and placed in slightly different media can be done using the model (3.1). The curve representing the dependence of the minimum of the LSM scores for targets with different height is shown in Figure 3.5 a) for the probing pulse used in the radar and a reference wavelet computed for a 5 cm height target.

As it can be seen from the figure, in the noiseless case the best LSM score varies from nearly zero (for the exact height match) up to 1 for the targets with 3.5 to 6 cm height and grows further with the height difference. The tolerance of LSM score to the volatility of the target height depends of course on the bandwidth of the probing pulse: the wider the bandwidth (hence the narrower the pulse) the faster the minimal LSM score grows with deviation of the target height from the reference. This phenomenon is also shown in Figure 3.5 a) where the dependence of the LSM score on the target height is shown in gray color for the case of the probing pulse with 6.5GHz bandwidth. In the latter case the minimal LSM grows from 0 to the level of 2.5 with the only 1 cm height discrepancy.

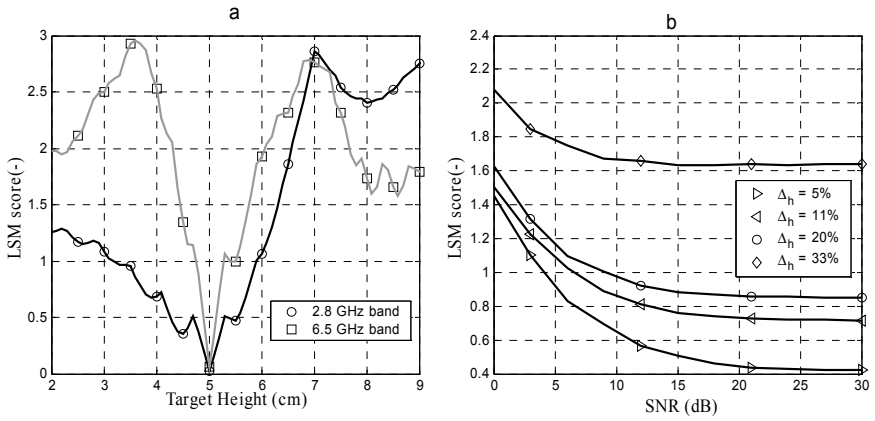

Figure 3.5 Dependence of the best LSM score from the parameters of target and hosting medium: a) varying target height, reference computed for h = 5 cm, probing pulses with bandwidth of 2.8 GHz and 6.5 GHz; b) varying target/reference height discrepancy and SNR, probing pulse with bandwidth of 2.8 GHz

It can be seen in the equation (3.1) that target effective velocity and target height are irresolvable from the shape of the response. The effective velocity depends on values of permittivity of target interior, the hosting medium, and the target height. As a result the influence of an inexact match in medium velocity manifests itself in the same way as a mismatch in the target height.

Another factor which influences the LSM score is the presence of the noise. In practice after the background removal the mine responses in A-Scans are corrupted with some random noise even if no clutter signal is present. The level of this noise is fairly constant for the whole measurement site while the energy reflected by mines differs depending on the type of the mine, depth of its placement, hosting medium parameters and roughness of the air/medium interface. Hence the signal to noise ratio (SNR) of the response varies from mine to mine. The influence of SNR on the LSM score is shown Figure 3.5 b) where the minimal LSM scores simulated for PMN2, M14, and NR22 mines and a 5cm high reference target are plotted. The figure demonstrates a general trend of the LSM score to grow when SNR gets lower and/or the height discrepancy gets larger. It turns out that the distribution of the minima of the LSM scores (as simulated for the fixed reference waveform and varying SNR and target height) tends to be un-skewed and its kurtosis varies in the range of 2.7 to 3.3. Therefore it may be reasonably approximated by a normal distribution, which is used on the second stage of the processing.

3.1.4 Procedure to determine the reference wavelet

As it can be seen from (3.5)-(3.7), the performance of the algorithm is largely dependent on the correct choice of the reference wavelet $h(t)$. On the other hand, no modeling is feasible in this case beyond a very general approach determined by

(3.1). Therefore I rely on the presence of a training dataset acquired in the controlled environment conditions to determine the parameters of the algorithm. In order to determine the reference wavelet I select a training subset in the training data. This subset (it is referred to as inner training subset) comprises a few A-Scans (after background removal) acquired over the tops of several well-visible PMN2 and M14 mines buried in different depths in sand. The reference wavelet is then defined as an un-weighted mean of the responses of these mines normalized to their maxima and shifted to the common midpoint. The process is illustrated in Figure 3.6, where these responses are overlapped and the resulting reference wavelet is given in the thicker line.

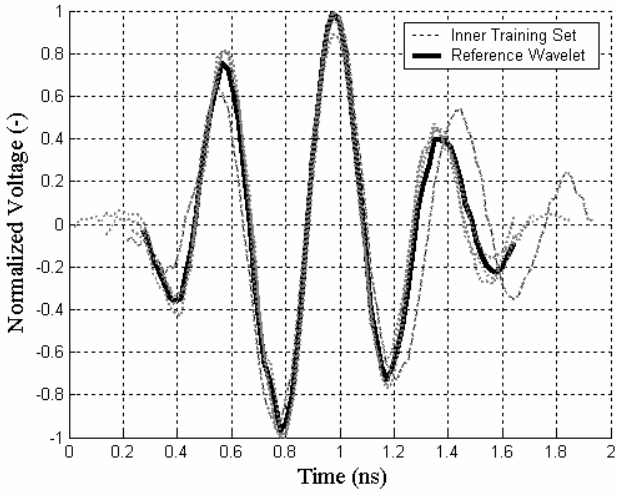

Figure 3.6 The A-Scans comprising the inner training dataset (dotted lines) and the resulting reference wavelet (solid line)

The width of the window in (3.6) and (3.7) is determined automatically to be equal to the duration of the reference wavelet. As it can be seen from the figure, the reference wavelet is restricted to the central parts of the mine responses where their shape is retained most thoroughly. This is done to avoid degradation of LSM scores corresponding to the responses of different mines.

3.2 Penalty Functional

The second stage of the algorithm performs suppression the unwanted reflections represented by local minima in the LSM score. Because in the LSM the presence of the target is marked by the minimum it is natural to apply a penalty term that would assign higher values to the time instances where the LSM gets the values close to zero and vice versa. This strategy is detailed in 3.2.1. Taking into ac-

count additional information on the distribution of the LSM scores it is possible to further elaborate the penalty functional for better representation on the target responses. This issue is considered in 3.2.2. Lastly, it would be of advantage for the SAR processing if the output of the penalty functional would have no DC content. The procedures to ensure that are described in 3.2.3.

3.2.1 Exponential penalty functional

Let $L[t;u,h]$ be the LSM score to the input A-Scan $u(t)$, i.e. output of (3.7). Then assigning the exponential penalty to it one obtains a penalized local similarity measure (PLSM):

$$P_{\exp}[L(u;t)] = e^{-L[t;u,h]} \tag{3.8}$$

The Figure 3.7 shows output defined by (3.8) to the input defined by A-Scans shown in Figure 3.4.

As it is seen from the figure the, the presence of the mines is indeed marked by maxima in the outputs of the PLSM (3.8). Moreover, these maxima represent the highest magnitudes present in the given A-Scans. The problem, however, is that the exponential penalty functional assigns drastically different scores to the different mines. In the given examples the weaker M14 mine is assigned a score which is 8dB lower than the larger PMN2 mine. This effect is caused by the slight deviations in the shapes of the responses and by the change in the SNR ratio, which is significantly lower for the case of the M14 mine. Such a discrepancy in the LSM scores within the same class of target may embarrass the application of feature fusion algorithms. Therefore ways to mitigate the problem should be found.

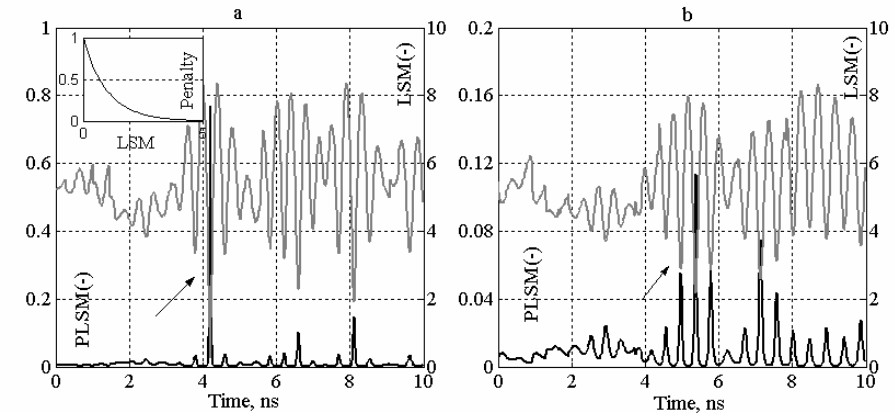

Figure 3.7 The LSM (pale lines) and PLSM scores (black lines) computed for the PMN2 a) and M14 b) mines; targets are marked with arrows; the penalty functional is shown in the inlet to the subfigure a).

3.2.2 Gaussian penalty functional

The problem of drastically unequal PLSM scores encountered in the previous subchapter can be met using the information about the distribution of the LSM scores expected for the given site. This distribution has been found nearly normal for the modeled data in 3.1.3. Taking this into account it is natural to assume the Gaussian shape for the penalty functional:

$$P_G[L(u;t)] = e^{\frac{(L[u(t)]-m_0)^2}{m_1^2}} \tag{3.9}$$

where m_i are yet to be defined parameters. Such penalty functional corresponds to the expected distribution of the LSM score for the targets of interest. It assigns larger scores to the time samples where the LSM gets values close to the expected for targets and suppresses the LSM scores, which significantly deviate from it. The centrality of the functional is defined with m_0 and selectivity by m_1.

To define these parameters an additional training dataset is employed. This *outer* training subset U is used to build up statistics from which the parameters m_i of the penalty functional are determined. This subset comprises collections of A-Scans acquired above several specimens of different targets and false alarm objects, and supplied with A-Scans acquired above presumably empty regions of the ground:

$$U = \{U_M \bigcup U_{FA} \bigcup U_{BG}\} \tag{3.10}$$

where U_M is the mines subset, U_{FA} is the false alarms subset, and U_{BG} is the subset of the A-Scans, which contain responses showing a large magnitude, but do not correspond to any particular object. The subsets U_M and U_{FA} are chosen to comprise the A-Scans that are likely to be coherently summed during SAR. The subset U_{BG} is never empty in test measurements due to factors like rough ground interface, pit borders, etc. Computing to the LSM scores for the A-Scans comprising U one obtains statistics of the $L[U]$ corresponding to the signatures of mines and clutter objects. In the resulting set we define two classes of LSM scores for targets (L_T) and clutter (L_C):

$$L[U] = L[U_M] \bigcup L[U_{FA} \bigcup U_{BG}] = L_T \bigcup L_C \tag{3.11}$$

An optimal pair of parameters m_i can be obtained maximizing the separation of the target and clutter classes in the output of (3.9). Due to the approximate normality of the distribution of the LSM scores for the target class the following choice of parameters guarantees that most of the target-relevant wavelets comprising L_T will obtain high score at the output of (3.9):

$$m_0 = \mu\{L_T\}$$
$$m_1 = 3\sigma\{L_T\} \tag{3.12}$$

where $\mu = \mu_1$ and $\sigma = \sqrt{\mu_2}$ are the estimates of the mean and standard deviation of the random process L_T computed via (2.9) and (2.10).

The output of (3.9) to the same input as for Figure 3.7 and the parameters defined by (3.10) – (3.12) is shown in Figure 3.8.

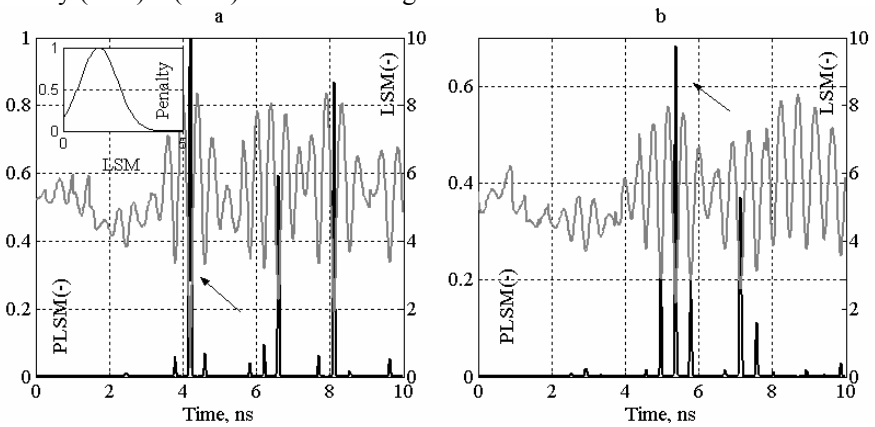

Figure 3.8 The LSM (pale lines) and Gaussian PLSM scores (black lines) computed for the PMN2 a) and M14 b) mine species; targets are marked with arrows; the penalty functional is given in the inlet to the subfigure a).

Just like in the output of (3.8) the mines are represented with sharp maxima, which are the largest values encountered in the respective A-Scans. Note however that this time the PLSM score assigned to the larger PMN2 mine is only 1.5 times higher than the one assigned to the smaller M14 mine. This equalization of the target response is important on the latter stage of the data processing.

At the same time the clutter is suppressed except for a few bursts, which are well separated from the images of the mines. Theses bursts are caused not by localized objects but by local similarity to the reference wavelet exhibited by portions of A-Scan. Because of that their spatial distributions do not represent hyperboloid shapes, as it is seen from Figure 3.9. The figure shows parts of B-Scans taken across the same mines as in the previous figures after application of PLSM (3.9). The traces of the mines are marked with arrows. The non-hyperbolic shape of the non-suppressed clutter traces is apparent and therefore one can expect successful suppression of these elements of clutter on hyperbola detection stage (e.g. SAR, as discussed in subchapters 3.2.3 and 1.1).

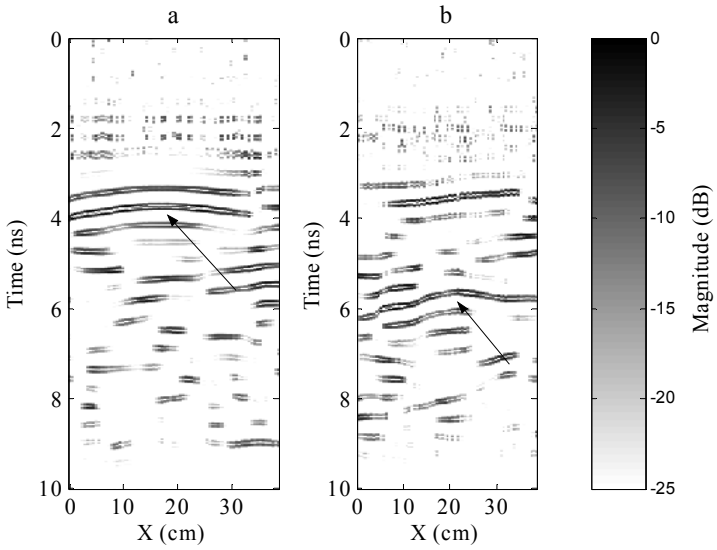

Figure 3.9 The B-Scans containing hyperbola traces of mines after PLSM: a) PMN2, b) M14. Mine-related hyperbolic traces are depicted with arrows

It is also important that the scores that both mines obtain at the output of (3.9) are very close to each other. Thus the clutter suppression is superimposed with target equalization by use of the Gaussian shaped penalty functional. This concept is further illustrated in Figure 3.10 where density distributions of critical scores obtained for the outer training subset are shown. By critical scores we mean the main peak-to-peak magnitudes of the target wavelet in the raw A-Scans, minima for the LSM score, and maxima for the PLSM scores in forms (3.8) and (3.9). The nonparametrical estimation of the densities is made via the kernel estimation method (2.9)-(2.10) with Epanechnikov kernel.

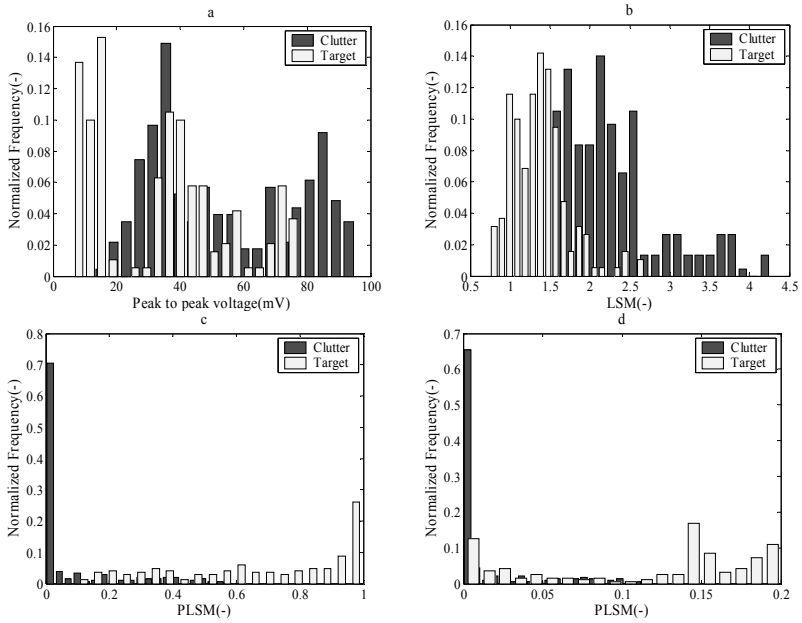

Figure 3.10 Sample Probability Density Functions for target and clutter classes in the outer training dataset for: input magnitude (a), LSM (b), and PLSM of the form (3.8) and (3.9) - (c) and (d).

It may be noticed from the figure that the densities of the distributions of the classes are strongly overlapped in the subfigure a), which illustrates the fact that the magnitude of the response wavelet does not constitute a good discriminative parameter for landmines. The densities of the LSM score shown in subfigure b) are well separated for the classes of targets and clutter. The wide spread of the scores resulted from PLSM (3.8) in the target class, which is visible in the subfigure c), causes worsening of the separation in comparison to the LSM. At the same time most of the wavelets relevant to targets are likely to receive higher scores at the outputs of (3.9), while the clutter related wavelets are concentrated near 0, as it is seen from the subfigure d).

Overall, application of any form of PLSM improves the separation of the clutter and target classes in comparison to a background model based algorithms operating alone. At that the Gaussian penalty functional demonstrated its superiority to the exponential one and should be preferred.

3.2.3 Modifications of PLSM as an input to SAR

In the case where the output of the clutter suppression algorithm serves as an input for the SAR focusing it should satisfy some additional requirements. Firstly, the output of the PLSM is desired to hold no DC content. And secondly, since

SAR is an efficient clutter suppression technique in itself it would be of advantage to optimize the parameters m_i taking into account the fact that SAR follows the PLSM in the DPS.

It can be seen from the figures and formulations above that both penalty functional (3.8) and (3.9) mark the position of the target with a sharp mono-pulse with values on the (0, 1] interval. This mono-polarity embarrasses the SAR focusing because the non-coherent energy, which presumably represents clutter, does not self-cancel in summation but adds up instead. This accumulation is slower than the accumulation of the coherent energy scattered by objects but still constitutes the clutter, which is significant for the smaller mines. To solve this problem the bi-polarity of pulses representing all the scattering phenomena must be ensured.

The bipolarity of the PLSM can be assured by high-pass filtering of the output of (3.9):

$$P_H[L(u;t)] = P_*[L(u;t)] \otimes F_H(t) \tag{3.13}$$

where $L(u;t)$ is the LSM score, P_* represents output of the penalty functional (3.8) or (3.9) and F_H is the impulse response of a high-pass filter. For example applying Butterworth filter of 7th order with cut-off frequency of 600 MHz to the PLSM one obtains the bi-polar signals in which the presence of the target is marked by sharp mono-cycles.

Alternatively, the high pass filtering may be organized through the time differentiation of the input. In this case $F_H(t) = \dot{\delta}(t)$ and (3.13) becomes:

$$P_D[L(u;t)] = \frac{d}{dt}\exp\left\{-\frac{(L[u(t)]-m_0)^2}{m_1^2}\right\} \tag{3.14}$$

The outputs of the (3.14) that correspond to the same inputs as before are shown in Figure 3.11.

The main characteristics of the outputs of (3.13) and (3.14) coincide. As it can be seen from the figure, the presence of the mines marked by maxima in the PLSM scores of (3.8) and (3.9) is clearly marked in this version of PLSM with sharp monocycles. It is worth noticing, that for both PMN2 and M14 mines the PLSM scores still receive roughly the same peak-to-peak magnitude.

At the same time, it is understood that introduction of this high-pass filtering step does not produce any additional separation for targets and clutter classes. However, this operation is necessary for the successful SAR focusing and therefore must be used only if the latter it supposed to be used.

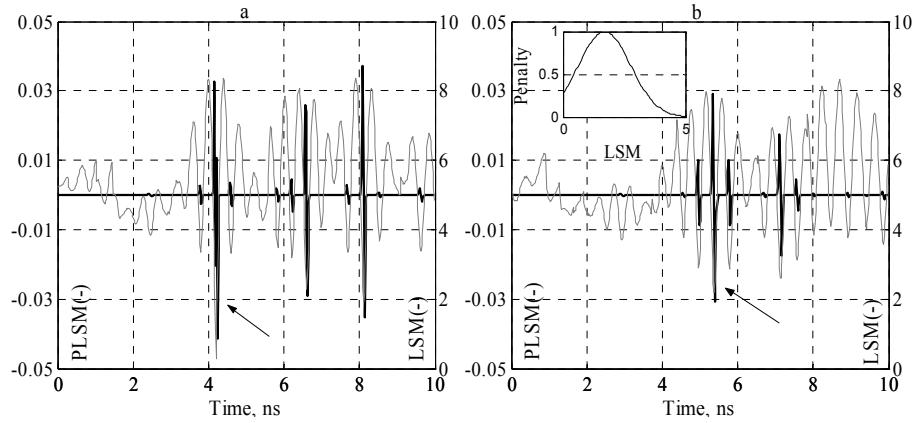

Figure 3.11 LSM scores for the A-Scans acquired at the tops of a PMN2 (a) and M14 (b) mines and their PLSM versions (darker lines). The penalty functional is given in the inlet on subfigure b); mine positions are marked with arrows

Addressing the second issue, one has to take into account all the A-Scans that will contribute to the image of every target. Ideally, all A-Scans falling into the antenna footprint area centered at the target should be accounted for. To this end I enlarge the outer training dataset (3.10) to include the A-Scans constituting these vicinities. Then the parameters m_i must be optimized to produce the best possible separation of the classes $P(L_T)$ and $P(L_C)$. Using the Fisher distance equivalent to the deflection (2.16) with $\alpha = 0.5$, one obtains the following goal function:

$$G(m_i) = \frac{\left[\mu_1\{P(L_t;m_i)\} - \mu_1\{P(L_t;m_i)\}\right]^2}{\mu_2\{P(L_t;m_i)\} - \mu_2\{P(L_t;m_i)\}} \tag{3.15}$$

where μ_i are the estimates of the first two moments of the corresponding sets. Then the parameters m_i are defined as:

$$m_i = \arg\max\{G(m_i)\} \tag{3.16}$$

In fact (3.16) constitutes a problem of non-linear optimization where exact connection between variables m_i and value of $G(m_i)$ is only given statistically. The rigorous solution of this problem is rather difficult but it is possible to take the values of m_i that maximize (3.16) in the vicinity of the initial guess defined by (3.12).

For the examples shown in the Fisher separations computed for the initial guess are {0.4, 2.8, 3.8, 2.5} for the input A-Scans, LSM, and two forms of PLSM respectively. The optimal values of the penalty functional parameters obtained optimizing the Fisher measure (3.15) are $m_0 \cong 1.5 mean\{L_T\}$ and $m_1 \cong 4.2 std\{L_T\}$. Using these parameters we obtain the improved separation of the target and clutter classes in the outputs of (3.9) and (3.14): {4.3, 2.9} for the two forms of PLSM respectively. These numbers confirm the notion that PLSM in the form (3.9) rather than

(3.14) should be used if target detection is organized by means which do not involve SAR. Note however, that the optimal parameters are data driven and must be recomputed for each training situation.

3.3 Superposition of SAR and PLSM algorithms

The considerations of the subchapter 3.2.3 allow for more effective optimization of the parameters of PLSM when it is used in sequence with SAR focusing. However, the following problem is connected to the consecutive application of PLSM and SAR algorithms. As transmit and receive antennas move further away from an object and the illumination becomes oblique the typical shape of the object's return changes due to the change of the illumination angle. Due to this, any particular target is marked with highest possible amplitude responses in the output of the PLSM algorithm only for the A-Scans, which correspond to a small range of illumination angles. This is illustrated in Figure 3.12 a) where the APM responses for different illumination angles are shown. This change leads to deterioration of the PLSM scores, as it is shown in subfigure b).

This shortcoming may diminish the performance of SAR focusing and following detection. The angle dependency of the reference wavelet can be established either by modeling or from a training dataset but it cannot be readily applied due to an angle ambiguity existing in a time-space C-Scans. More precisely, the illumination angle cannot be tracked in the <t; x; y> 3-D domain. That is a wavelet appearing at each time sample of an A-Scan taken from such a domain may correspond to any equidistant object and thus come from any illumination angle. In the present subchapter I resolve this ambiguity by *superimposing* the PLSM algorithm with the SAR migration technique. In SAR-focused image of an <z;x;y> domain for each imaged point there is only one object placed in it, which is considered as a possible source for the wavelet. Therefore the angle ambiguity can be resolved and it is possible to image the given point integrating over the accordingly delayed outputs of CROW algorithm with reference wavelets dependent on the illumination angle.

Recalling the formulation of the SAR procedure:

$$F(\vec{r}) = \iint\limits_{\xi,\gamma \in A} C_{\xi,\gamma}(T)\, d\xi d\gamma \tag{3.17}$$

where $\vec{r} = (x, y, z)$ is the point being imaged, it is seen that SAR provides focusing of a common-offset time-space GPR C-Scan by mapping it into a 3D space image. In (3.17) $C_{\xi,\gamma}(\cdot)$ and $F(x, y, z)$ represent initial and focused C-Scans, A is a 2D aperture of the radar to be synthesized, and T is the time needed for a probing pulse to travel from the transmit antenna to the point being imaged and backwards to the receive antenna:

$$T = T(x, y, z, \xi_T, \gamma_T, A_T, \xi_R, \gamma_R, A_R, \varepsilon_r) \tag{3.18}$$

where (x, y, z) is the point being imaged, (ξ_T, γ_T, A_T) and (ξ_R, γ_R, A_R) are the coordinates of the transmit and the receive antenna respectively, and ε_r is the ground's permittivity. Ray paths corresponding to one-way propagation of a probing pulse between the point being imaged and the antenna is shown in Figure 3.13.

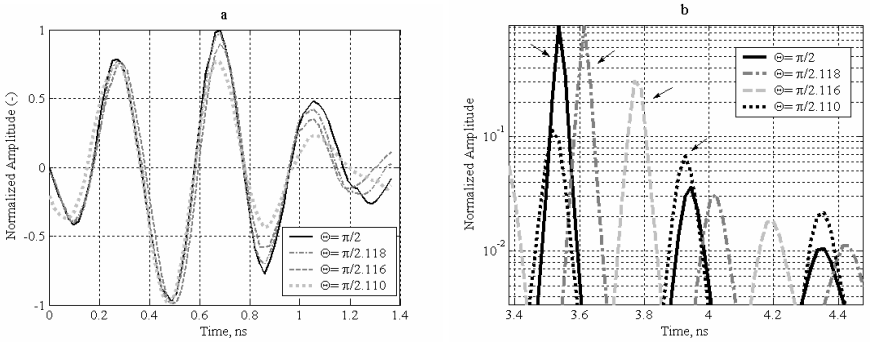

Figure 3.12 Change of the response of an APM mine versus angle of illumination Θ_1 (a) and PLSM deterioration caused by it (b); arrows denote the position of the mine's wavelet.

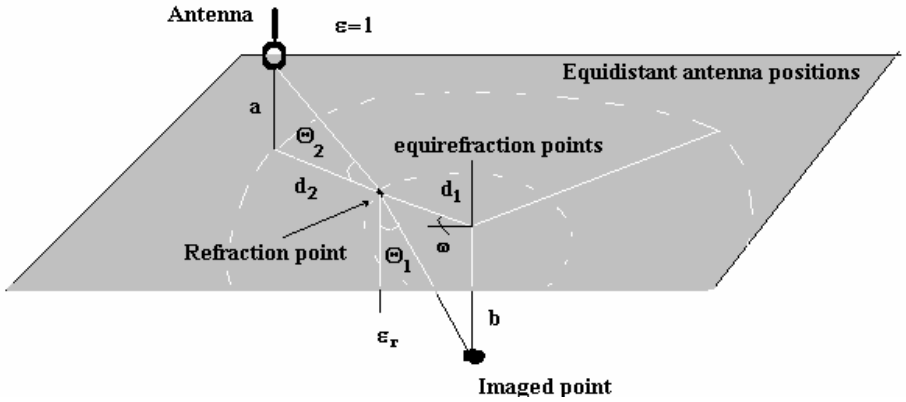

Figure 3.13 The SAR scheme

As it can be noted from the discussion of the IRCTR antenna system in 1.1.3 the ray bending due to the refraction must be taken into account in calculations of *T()*. These calculations may be done using the Snell's law, which fixes the values of the refraction angles. A fourth order equation for the optimal refraction may be devised from this low [82]. Alternatively a fourth order equation may be derived

for $\cos^2\Theta_1$. To this end one assumes that the fastest possible path that electromagnetic pulse follows lies in a single plane. Then using the triangulation shown in the figure and the Snell's law one obtains the equalities:

$$\begin{cases} \sin\Theta_2 = \sqrt{\varepsilon_r}\sin\Theta_1 \\ a\tan\Theta_2 + b\tan\Theta_1 = d_1 + d_2 \end{cases} \tag{3.18}$$

In (3.18) Θ_i are the refraction angles, a is the antenna height, b is the object's depth, and $\rho = d_1 + d_2$ is the horizontal projection of the distance from the antenna to the point being imaged. Substituting the first equality of (3.18) into the second one gets the equation

$$\frac{a\sqrt{\varepsilon_r}\sqrt{1-\cos^2\Theta_1}}{\sqrt{1+\varepsilon_r\cos^2\Theta_1-\varepsilon_r}} + \frac{b\sqrt{1-\cos^2\Theta_1}}{\cos^2\Theta_1} = \rho \tag{3.19}$$

which can be transformed to the following polynomial equation:

$$\begin{aligned} &\left\{\left(b^2+a^2+\rho^2\right)\varepsilon_r - 4a^2b^2\varepsilon_r\right\}p^8 + \\ &\left\{2\left(b^2+a^2+\rho^2\right)\left(b^2+\rho^2-\varepsilon_r b^2-\varepsilon_r\left(b^2+a^2+\rho^2\right)\right)\varepsilon_r + 8a^2b^2\varepsilon_r - 4a^2b^2\varepsilon_r(1-\varepsilon_r)\right\}p^6 + \\ &\left\{-2b^2(1-\varepsilon_r)\left(b^2+a^2+\rho^2\right)\varepsilon_r + \left(b^2+\rho^2-\varepsilon_r b^2-\varepsilon_r\left(b^2+a^2+\rho^2\right)\right)^2 - \right. \\ &\qquad \left. -4a^2b^2\varepsilon^2{}_r + 8a^2b^2\varepsilon_r(1-\varepsilon_r)\right\}p^4 - \\ &\left\{2b^2(1-\varepsilon_r)\left(b^2+\rho^2-\varepsilon_r b^2-\varepsilon_r\left(b^2+a^2+\rho^2\right)\right) - 4a^2b^2\varepsilon_r(1-\varepsilon_r)\right\}p^2 + b^4(1-\varepsilon_r)^2 = 0 \end{aligned} \tag{3.20}$$

where $p = \cos^2\Theta_1$. The order of the equation can be reduced to the fourth order and then it allows an analytical solution. This solution is of course impractical because it is not possible to decide which of its four roots is the closest to 1 without computing them all. On the other hand, despite its lengthy format, the equation (3.20) is quite easy to solve numerically. One knows beforehand that $p \le 1$ and it is the largest root of the equation he is interested in. This knowledge allows avoiding local minima and the Newton scheme [83] converges in 2-3 iterations due to the facts that 1) good initial guesses are provided by solutions in a neighboring point and 2) the exact form of the polynomial derivative is readily available. Finally, it will be of importance that the coefficients of the equation (3.20) stay constant for all antenna positions that are equidistant to the given imaged point.

Having determined the refraction angle lets note that the antenna coordinates (ξ_T, γ_T, A_T) and (ξ_R, γ_R, A_R) may be expressed via each other for common-offset data. Dropping the indexes redundant for this particular case (3.17) and (3.18) are combined into:

$$F(\vec{r}) = \iint\limits_{\xi,\gamma \in A} C_{\xi,\gamma}(T(\xi,\gamma;\Theta_i))d\xi d\gamma \tag{3.21}$$

The integration (3.21) coherently adds up appropriately shifted A-Scans, which presumably results in higher absolute values of these magnitudes in the regions occupied by contrast objects.

Substituting (3.6) and (3.14) into (3.21) one obtains the expression of a SAR operator applied to the output of PLSM:

$$F_P(\vec{r}) = \iint\limits_{\xi,\gamma \in A} P_\bullet\left\{\int\limits_S \left[\hat{C}_{\xi,\gamma}(\tau;T(\xi,\gamma;\Theta_i)) - h(\tau)\right]^2 d\tau\right\} d\xi d\gamma \tag{3.22}$$

where $\hat{C}$ has the same meaning as $\hat{u}$ in (3.7) and $P_\bullet$ is a penalty functional in one of its forms. In the formulation (3.22) the angular ambiguity mentioned above is resolved because the time delay is calculated for the specific direction fixed by the pair of coordinates ξ, γ. Thus the angle dependency of the reference wavelet can be exploited. Defining $H(t,\Theta)$ as an angle dependent analogue of $h(t)$ in (3.6) and introducing it into (3.22) one obtains:

$$F_{P(\Theta)}(\vec{r}) = \iint\limits_{\xi,\gamma \in A} P_\bullet\left\{\int\limits_S \left[\hat{C}_{\xi,\gamma}(\tau;T(\xi,\gamma;\Theta_i)) - H(\tau,\Theta_1(\xi,\gamma))\right]^2 d\tau\right\} d\xi d\gamma \tag{3.23}$$

Equation (3.23) represents the sought superposition of the PLSM and SAR algorithms. Recall now that the refraction angle is constant for all antenna positions equidistant with respect to the point being imaged:

$$\frac{\partial}{\partial \omega}\Theta_1(\xi(d,\omega),\gamma(d,\omega))\bigg|_{\rho=const} \equiv 0 \tag{3.24}$$

In this representation ω is the angle defining the direction from the projection of the point imaged onto the surface to the projection of the antenna onto the surface. With that in mind one can move to the polar representation of the integration (3.23):

$$F_{P(\Theta)}(\vec{r}) = \int\limits_0^{r_A}\int\limits_0^{2\pi} P_\bullet\left\{\int\limits_S \left[\hat{C}_{r\omega}(\tau;T(r,\omega)) - H(\tau,\Theta_1(\rho))\right]^2 d\tau\right\} d\omega d\rho \tag{3.25}$$

where r_A is the radius of the antenna footprint. SAR (3.25) can be further improved by introduction of a radius-dependent weighting factor that would assure that the closest A-Scans have more influence than the farthest:

$$F_{P(\Theta)}(\vec{r}) = \int\limits_0^{r_A} W(\rho)\left\{\int\limits_0^{2\pi} P_\bullet\left\{\int\limits_S \left[\hat{C}_{r\omega}(\tau;T(r,\omega)) - H(\tau,\Theta_1(\rho))\right]^2 d\tau\right\} d\omega\right\} d\rho \tag{3.26}$$

where $W(\rho)$ is a smooth function decreasing as ρ grows.

The practical implementation of (3.26) assumes replacement of the integrals with finite sums. The most straightforward discretization leads to:

$$F_{P(\Theta)}(x_i, y_j, z_k) = \sum_{r=r_{\min}}^{R_A} W_r \sum_{(\xi-x_i)^2+(\gamma-y_j)^2 \equiv r} P_{\bullet}\left(\left\|\hat{C}_{\xi\gamma}(\tau; T_{r,\omega}) - H_{\tau,\Theta_1(\rho)}\right\|\right) \tag{3.27}$$

This procedure uses only the A-Scans actually measured and present in the C-Scan being focused. Transformation to the polar coordinates manifests itself in the rearranging of the order of summation. The procedure is computationally effective and does not require much computational time. The more sensitive and more time consuming discretization implies using advanced integration techniques (say, Simpson rule) and, more importantly, virtual A-Scans. These are the A-Scans that are constructed rather than actually measured at the locations of the equidistant lines. Their construction is made via 3D Fourier interpolation of the A-Scans measured in the neighboring points. The resulting discretization reads:

$$\begin{aligned} &F_{P(\Theta)}(x_i, y_j, z_k) = \\ &= I\left(W_r I\left(P_{\bullet}\left(I\left(\hat{C}^i{}_{r,\omega}(\tau; T_{r,\omega}) - H_{\tau,\Theta_1(\rho)}; \tau, [0, S]\right)\right), \omega, [0, 2\pi]\right), r, [0; R_A]\right) \end{aligned} \tag{3.28}$$

where $I(g; \psi, [\psi_0, \psi_1])$ represents a procedure of the numerical integration of $g(\psi, ...)$ by the variable ψ on the interval $[\psi_0, \psi_1]$ and $\hat{C}^i_{\xi\gamma}$ is an interpolated A-Scan that would have been measured at the exact location (ξ, γ). The representation (3.28) yields results more accurate than those of (3.27) but requires lengthier computations.

As the final note it should be kept in mind that the formulations given in this subchapter have 2 drawbacks: the procedure is more sensitive to the shape of the object due to the fact that the waveforms of the responses to oblique illumination are considered; the bipolarity of the output of PLSM cannot be assured since the output of PLSM does not emerge in the explicit form. The advantages of the approach include more precise following of the response, which allows using of fairly sharp penalty functional. This, in turn, results in further suppression of the clutter and equalization of the target responses.

3.4 Conclusion for Chapter 3

In this chapter I have presented a novel generic waveform-based algorithm for clutter suppression, which improves detectability of a certain class of targets (i.e. antipersonnel landmines) with a video impulse ground penetrating radar. The algorithm (penalized local similarity measure) is demonstrated to possess the following features:

1. It detects a class of low-metal APM with a cylindrical shape (such as PMN2, M14, and NR22) using just a single reference target return;
2. The processor aims at suppression of the clutter responses from non-targets and leaves intact the spatial patterns inherent to localized objects;

3. As a result it operates best when the background clutter is removed *prior* to it and spatial pattern of targets is detected *after* its use;
4. The output of the processor is perfectly suited to be an input to a SAR focusing procedure due to its sharp bi-polar shape;
5. The output of the processor does not directly depend on the magnitude of the input providing equalization of the responses from mines of different sizes;
6. The core processor of the algorithm is insensible to the presence of clutter objects regardless of their size and/or reflectivity provided that their signatures wavelets are different from the one of the reference wavelet;
7. The algorithm is trained on datasets acquired in the controlled environment and is then successfully applied on the test site with similar but not identical soil conditions and data acquisition parameters;
8. The algorithm is shown to work with the GPR pulses having a 2.8 GHz bandwidth and the antenna system sufficiently (>20 cm) elevated over the ground. Such an antenna elevation ensures the consistency of target return wavelet, which is required by the algorithm. On the contrary, by close-in detection with a hand-held GPR a target is typically situated in the reactive near-field of an antenna system. Under such conditions a target return changes its waveform by variations of a target burial depth, antenna elevation and other factors.

The core algorithm is then superimposed with the SAR procedure. This superposition allows introduction of the angle-dependent reference wavelet. A real data example shows very promising results with this type of clutter suppression.

Chapter 4 Feature Generation and Selection

The considerations given in the Chapters 2 and 3 cover the issues of data processing and target detection in confidence maps. The present Chapter is dedicated to construction of confidence maps and definition of auxiliary features in the maps. The former task is considered in subchapter 4.1 and the latter one in subchapter 4.2.

4.1 Improved projection algorithms

As it was defined in 2.1 the data processing scheme results in a 2-D confidence map a construction of which from a 3-D processed dataset arises as a part of the mine detection problem. This construction often requires a projection of a confidence defining feature distributed in 3-D onto a flat surface. In 2.1.2 this concept has been exemplified with the simplest and intuitively understood energy projection. In the present subchapter I discuss two other projection techniques, each involving its own confidence defining feature:

1. The Windowed Energy Projection (WEP, 4.1.1)
2. The Alternating Sign Windowed Energy Projection (ASWEP, 4.1.2)

The latter projection technique is then extended to 2D and 3D cases (4.1.3) where confidence corresponding to each A-Scan is defined via the neighboring ones. This extension allows also construction of a mapping procedure for cross-polar radar (4.1.4).

4.1.1 Windowed energy projection

The energy projection defined in 2.1.2 is the most natural projection scheme where the confidence defining feature is just the energy scattered by the subsurface in the given location. Therefore the confidence maps constructed by this projection consist of pixels with clear mathematical and physical sense, which allows accurate characterization of the clutter and predictable performance of detectors. The disadvantage of the approach is that it often leads to a large number of false alarms present in the resulting map. Let me repeat its definition here for the sake of completeness:

$$E(x,y)=\int_{z_0}^{z_1} F_{xy}^2(z)dz \tag{4.1}$$

where z_i are the highest and the lowest depths present in the focused A-Scan $F(z)$. To lower the amount of false alarms in the map resulting from (4.1) the windowed version of the energy projected is introduced.

The WEP [85] is the 3D→2D mapping, which preserves as much information of the object responses as possible, while leaving the incoherent energy behind. It utilizes the fact that the image of an APM in a focused A-Scan occupies 3-6 cm (depending on the type of the processing), which represents 20-40% of the total length of the A-Scan. The rest of the A-Scan is contains clutter-bound energy, which is not caused by the target itself. Taking this into account, one can expect that replacing the energy projection (2.3) with the energy contained in the window corresponding to the target will better separate the target and clutter classes. More precisely, the windowed energy projection is defined via:

$$E_w(x,y) = \max_{z_0} \int_{z_0-w/2}^{z_0+w/2} F_{x,y}{}^2(z)dz \tag{4.2}$$

where w is the window in which the energy of the target is concentrated. The difference between the EP and WEP is outlined in the Figure 4.1where portion of two focused B-Scans are shown. The subfigure a) represents the output of the base-line data processing scheme and the subfigure b) represents the output of a DPS that uses PLSM. The images of the mines are depicted with arrows. The windows containing approximately 90% of the energy of the mines are also shown.

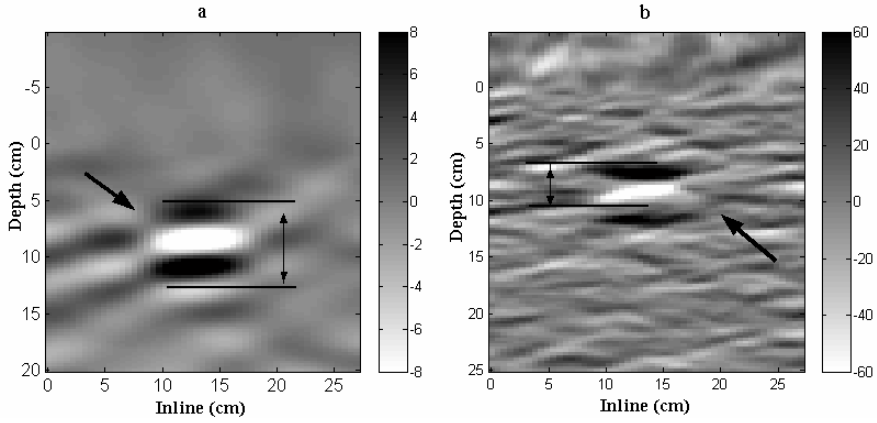

Figure 4.1 Windows containing the most of the energy of targets a) for base-line DPS, b) for a DPS using exponential penalty for clutter suppression

The choice of the window width is dictated by two contradicting factors: the window should include as much of the energy of the mine response as possible and be as narrow as possible to suppress the levels of the mine-free A-Scans. Finally, this should hold for all types of mines. To determine the optimal width for the given site one again relies on the training subset. This subset consists of a few fo-

cused A-Scans representing the target images (U_T) and a substantial amount of focused A-Scans that contain background clutter alone[2]:

$$U = U_T \bigcup U_{BG} \tag{4.3}$$

Applying (4.2) to the A-Scans comprising the set U_T one obtains the target brightness characteristics as a function of the window width w. Computing this function for the subsets U_T and U_{BG} it is possible to construct a discriminating functional $D(w; F_T, F_{BG})$:

$$D(w; F_T, F_{BG}) = \frac{E_w(w; F_T)}{E_w(w; F_{BG})} \tag{4.4}$$

where $F_T \in U_T$ and $F_{BG} \in U_{BG}$. Averaging D over the training subset one obtains the discriminating function $\overline{D}(w)$:

$$\overline{D}(w) = \frac{\overline{E}_w(w; U_T)}{\overline{E}_w(w; U_{BG})} \tag{4.5}$$

where $\overline{E}$ means the averaging made over the second parameter. This function represents a signal to background clutter ratio in terms of WEP. The optimal window width maximizes this function:

$$w_{opt} = \arg\max_w \overline{D}(w) \tag{4.6}$$

Alternatively, one can consider the ratio of the average target signal to background clutter. Maximizing each of these ratios with respect as a function of the window width one obtains a random process:

$$\varpi_k = \arg\max_w \frac{\overline{E}_w(w; U_T)}{\overline{E}_w(w; F_{BG}^k)} \tag{4.7}$$

where each ϖ_k corresponds to an A-Scan $F_{BG}^k \in U_{BG}$. In this case the optimal window width is given by the most probable value of the process $\{\varpi_k\}$.

Both ways of determining the optimal width of the WEP window are illustrated in Figure 4.2. The function $E_w(w; U_T)$ is plotted in the subfigure a) for the A-Scans comprising the training subset. Also the numerator of (4.5) is overlapped in the subfigure. The subfigure b) shows the same values for the training subset U_{BG} and the denominator of (4.5). All the functions in the subfigures a) and b) are normalized at their mean values with respect to w for the sake of compactness. The discriminating function $\overline{D}(w)$ is plotted in the subfigure c) overlapped with

[2] Note that this algorithm is not meant to suppress images of friendly objects but rather ensures that all small localized objects are visible in the resulting map.

the density of the process $\{\varpi_k\}$estimated from samples. As it can be seen from the subfigure, both procedures suggest the same optimal window width of 4 cm.

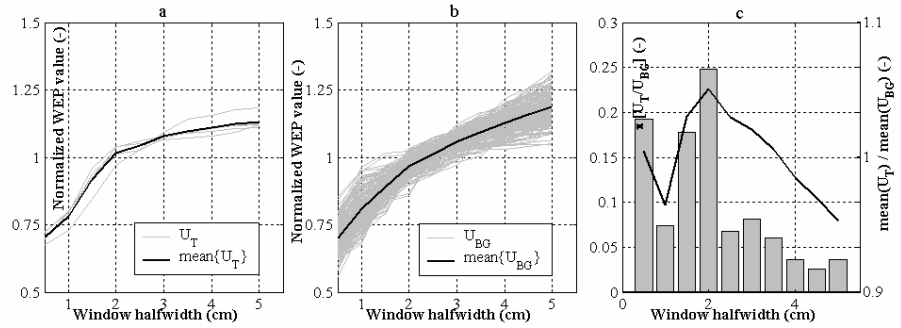

Figure 4.2 Determination of the optimal window for WEP: dependency of the WEP values on the window width for the subsets U_T (a) and U_{BG} (b); discriminant function (4.5) and probability density of the process (4.7)– c)

The application of the WEP with optimal window is exemplified on measured data in Figure 4.3. The measurements were made over a piece of a sandy minefield simulation site (Appendix B.1). The subfigures a) and b) represent the EP and WEP maps obtained with (4.1) and (4.2) respectively in which the targets are encircled. The contrast of the images is tuned in such a way that the weakest of the targets is just visible.

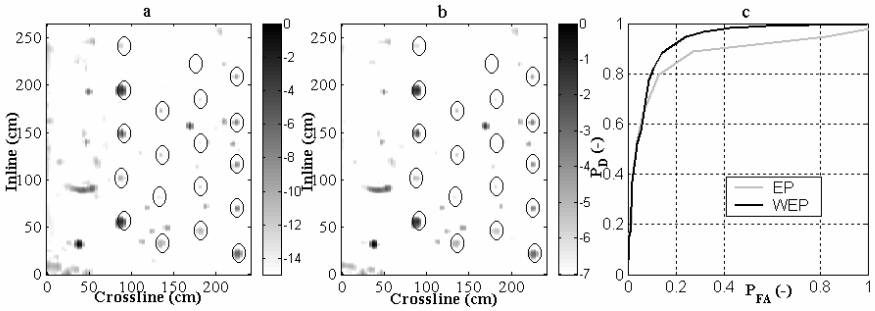

Figure 4.3 EP (a) and WEP (b) maps of a minefield and corresponding a-priori ROC curves

As it can be seen from the comparison of the subfigures a) and b), WEP allows much less clutter into the map. For example, the rough pit border along the first B-Scans is effectively suppressed. Although the pit border can be looked at as an artifact peculiar to the test site, analogous situation may arise on a real site due to the presence of large remote structures like logs or ruins etc.

Besides, the target distribution is more compact in WEP than in EP. That is the weakest target is 6.5 dB lower than the strongest one in WEP, whereas in EP this ratio is equal to 14.

These factors manifest themselves in the a-priori ROC curves built in the sub-figure c) according to the rule (2.17). The densities of clutter and target feature distributions are obtained using the kernel estimation technique. The clear superiority of WEP over EP for this particular case results in ~1.67 lower area above the curve.

4.1.2 Alternating sign windowed energy projection

The alternating sign windowed energy projection (ASWEP [70]) is a development of the idea of WEP. It further exploits the a-priori knowledge of the distribution of the energy of mines in focused C-Scans. As it can be seen from the Figure 4.1 a typical image of a mine in a SAR focused A-Scan consists of several bulbs of changing polarities. This shape is ultimately caused by the specifics of wavelets, which represent targets in A-Scans that are the input into SAR procedure. As it was pointed above, these inputs are either triplets for the base-line processing scheme or monocycles for the high-passed outputs of PLSM. The superposition of PLSM and SAR considered in Chapter 1.1 results in an exception from this general rule and therefore is inadmissible to ASWEP. These considerations are illustrated in Figure 4.4 for the case of a base-line processing.

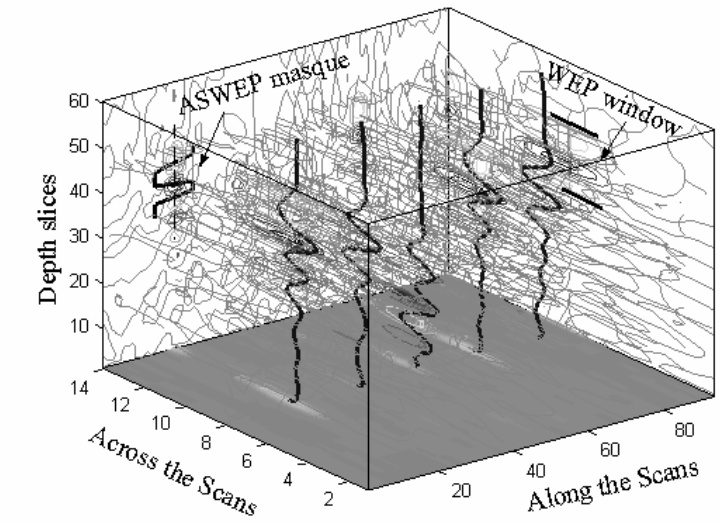

Figure 4.4 An isometric view of a portion of a focused C-Scan. The pale A-Scans are measured over the tops of several AP mines

The Figure 4.4 represents a portion of a focused C-Scan in an isometric view. The portion contains images of five AP mines placed in different depths. The A-Scans measured over the tops of these mines are shown in thicker lines and the EP map of this portion of the C-Scan is shown bottom of the image. The energy based images of the five targets are visible in the bottom map as spots with different brightness. Random iso-levels shown in gray lines correspond to the clutter energy. The transparency of the figure is tuned in such a way as to allow a clearest possible view onto the targets.

It can be seen from the figure that the shape of the target images remains approximately the same. Similar effect of shape consistency has been described in [13] for a forward-looking GPR. There this shape consistence has been used as a basic descriptor for construction of a maximum deflection-based mapping (short description is given in the introductory subchapter 1.2.3). Here I am planning to build an algorithm that would improve the detectability of the targets using the observed consistency of their image structure.

Low wave-number content of focused A-Scans prevents construction of a target/clutter separation technique similar to PLSM. Moreover, the energy content of a target image in the focused A-Scan may contain important information (e.g. in PLSM based DPS). Therefore a projection technique that does not exclude energy content should be built. Such a projection is given by:

$$E_{aw}(x,y)=\max_{z_0}\left\{\int_{z_0-w/2}^{z_0+w/2}F_{x,y}(z)\Theta(z)dz\right\}^2 \tag{4.8}$$

where $\Theta(z)$ is a mask representing a typical target image in the given C-Scan. Unlike WEP (4.2) the choice of *w* is not in our hands as it is automatically given by the support of the function $\Theta(z)$.

The definition of the mask $\Theta(z)$ is made using a training data. A simple triple valued mask can be defined using a single target image by [70]:

$$\Theta_{tv}(z)=\begin{cases}-1, z\in\{Z_i^-\}_i\\ 1, z\in\{Z_j^+\}_j\\ 0, z\notin\left(\{Z_j^+\}_j\bigcup\{Z_i^-\}_i\right)\end{cases} \tag{4.9}$$

where $\{Z^-\}$ and $\{Z^+\}$ are the collections of the positive and negative depth portions for the mask $\Theta_{tv}(z)$. Such a mask is plotted as a black line on the back wall of the isometric Figure 4.4 above. In that particular case $\{Z^+\}$=[1:6]+[14:17] and $\{Z^-\}$=[7:13]+[18:23]. The improvement yielded by use of ASWEP (4.8) – (4.9) can be judged from the Figure 4.5 where the same data as in Figure 4.3 are used.

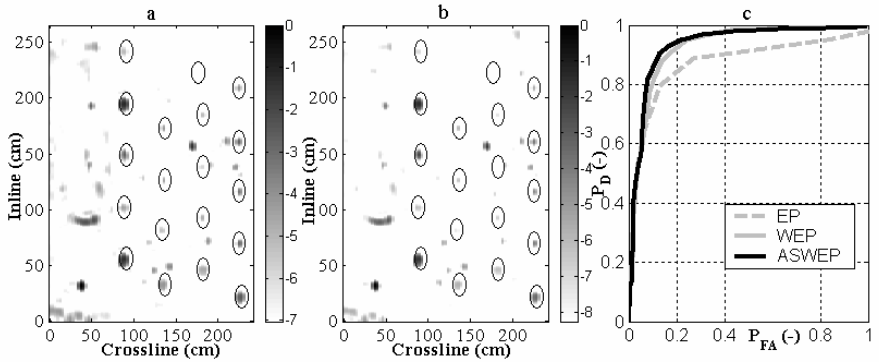

Figure 4.5 WEP (a) and ASWEP (b) maps of a minefield and corresponding a-priori ROC curves

As it can be seen from the figure, the ASWEP marginally outperforms WEP and significantly EP in this particular case. The use of the exchanging polarities rather than just gating like in WEP allows higher scores assigned to the A-Scans showing the behavior similar to what is expected of target images. As a result the corresponding ROC curve is better for ASWEP than for WEP at all levels of detection probability, which results in ~5% reduction of the area above the curve.

The performance of the ASWEP (4.9) can be improved with introduction of more sophisticated masks. For example, fitting a sinusoidal signal to the target image in a focused A-Scan yields a sinusoidal mask:

$$\Theta_s(z;k,w) = \sin(2\pi k z) W(z;w) \tag{4.10}$$

where k is the wavenumber, W is a window function similar to (3.7) and w is the window width. The optimal wavenumber of the mask is readily obtainable via Fourier transform. The transformation yields the spectral composition of the focused A-Scans containing a target image and its dominant wavenumber should be taken as the parameter k. This step is illustrated in Figure 4.6, where the A-Scan containing an image of a M14 mine put to the depth of 6 cm is shown. The subfigure a) represents the depth distribution of the brightness (voltage levels after SAR) and the subfigure b) gives its wavenumber magnitude spectrum. The fitted sine signal is shown in both subfigures with a pale line.

After the wavenumber parameter is established, the optimal duration of the mask is obtained via procedure similar to (4.4). Unlike the former case here I use the training subset (3.11) that contains also false alarms object images. Some of these non-mine object images are fitted with signals which wavenumber components and/or duration are different from those of the mines. This factor can be profitably used for the target/clutter dichotomy and is the reason for expansion of a training set.

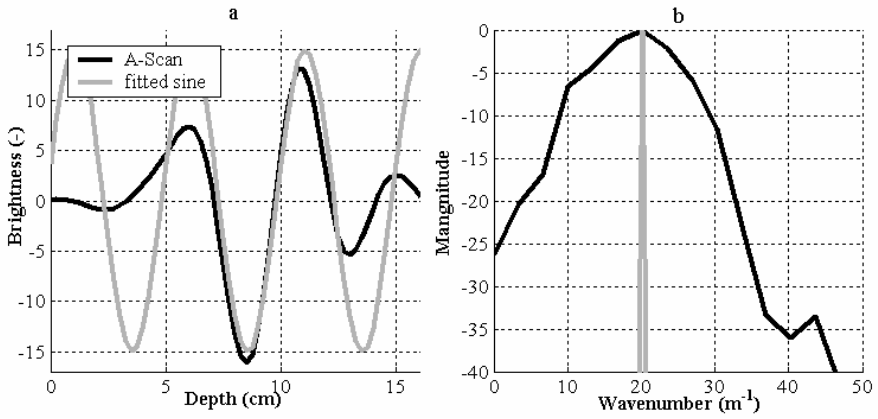

Figure 4.6 A Focused A-Scan containing an image of a M14 mine and fitted sine: a) depth-brightness representation; b) wavenumber – magnitude spectrum

More precisely, to determine the optimal duration of the sine signal one defines the training set

$$U = U_T \bigcup \{U_{BG} \bigcup U_{FA}\} = U_T \bigcup U_C \tag{4.11}$$

and the following functions on it:

$$D(w; F_T, F_C) = \frac{E_{aw}(w; F_T)}{E_{aw}(w; F_C)} \tag{4.12}$$

$$\overline{D}(w) = \frac{\overline{E}_{aw}(w; U_T)}{\overline{E}_{aw}(w; U_C)} \tag{4.13}$$

Like in previous considerations $F_T \in U_T$ and $F_C \in U_C$ are A-Scans representing the training subsets and $\overline{D}(w)$ is obtained by averaging D over the training subsets. After construction (4.11)-(4.13), (4.6) again yields the optimal duration of the mask. The process of selecting the optimal duration is shown in the Figure 4.7. Just like for the Figure 4.2 the figure shows function E_{aw} built for the target and clutter training subsets in the subfigures a) and b) and the discriminant ration (4.13) in the subfigure c).

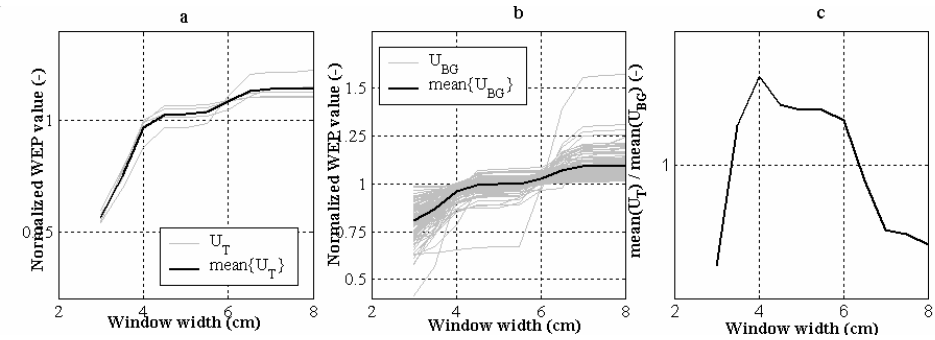

Figure 4.7 Determining the sine mask duration: a) target training subset, b) clutter training subset, c) discriminant ratio

Further improvement of the mask is obtained via introduction of a tapering factor. Let's consider a mask given by:

$$\Theta_G(z,k,w,m_i)=\sin(2\pi k z)W(z,w)G(z,m_1,m_2) \tag{4.14}$$

where $G(z;m_i)$ represents the Gaussian kernel with mean m_1 and variance m_2 and rest of the parameters are described above. The mask (4.14) is given by a sine signal tapered by a Gaussian window. This mask is able to better fit the shape of the 1D image of a typical target (see Figure 4.8).

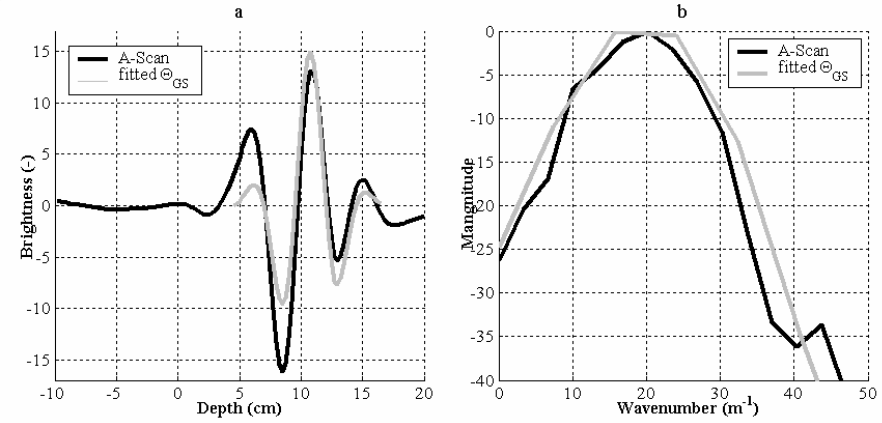

Figure 4.8 Fitting of a Gaussian tapered sine mask: a) depth-brightness, b) wavenumber-magnitude representations

On the other hand the rigorous fit of this mask requires simultaneous optimization of four parameters. This problem is difficult to solve when only a small training set is supposed. Moreover, a solution obtained in such conditions would not be robust with respect to the change of the dataset. To make the problem more tractable I introduce several simplifications. First, I assume that the parameter w

can be taken equal to the width of a typical image of a M14 mine[3]. Then two out of the three other parameters of (4.14) can be easily calculated. Namely, the wavenumber k is obtained independently of other parameters using the Fourier transform procedure described above and the Gaussian kernel is assumed to be centered at the center of the mask:

$$m_1 = \frac{w}{2} \tag{4.15}$$

Therefore I obtain just one parameter to fit:

$$\Theta_G(z;m_2) = \sin(2\pi k z) W(z,w) G\left(z, \frac{w}{2}, m_2\right) \tag{4.16}$$

Optimization of (4.15) with respect to m_2 follows the lines of the alternative way of definition of the optimal duration of the sine mask. Namely, one defines the decisive functional

$$D(m_2; F_T, F_C) = \frac{E_{aw}(m_2; F_T)}{E_{aw}(m_2; F_C)} \tag{4.17}$$

from which a random process of optimal values for $m_2\left(F_C^k\right)$ is obtained via averaging over the training subset U_T:

$$\varpi_k = \arg\max_w \frac{\overline{E}_{aw}(m_2; U_T)}{E_{aw}\left(m_2; F_c^k\right)} \tag{4.18}$$

The optimal value for the parameter m_2 corresponds to the expected value of the process (4.18). The selection of m_2 is illustrated in the Figure 4.9 which is built similarly to the Figure 4.2.

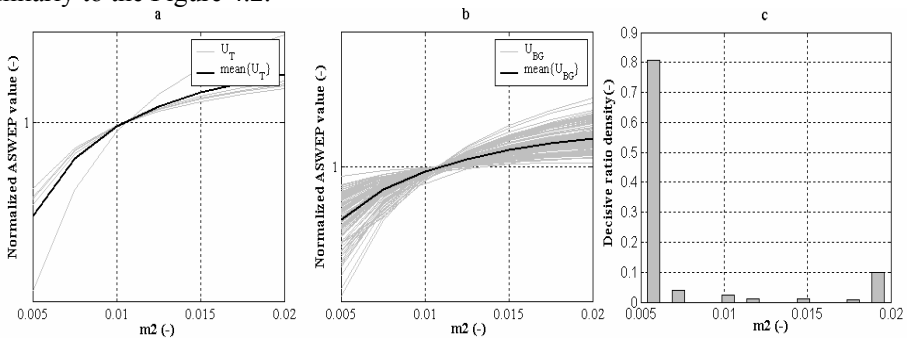

Figure 4.9 Determination of the optimal value for m_2

The following example allows to asses performance of different types of projections. For the example I shall use the same dataset as was used for construction

[3] Note, that w is not equal to the optimal width of the sine signal.

of the Figure 4.3. Applying to the same focused C-Scan different projection techniques one obtains different confidence maps. After application of automated detection and target/clutter dichotomy, the probability densities for classes of target and clutter are estimated via kernel estimation technique. On the basis of these densities a-priori ROC curves are built. These ROC curves are shown in the Figure 4.10 a).

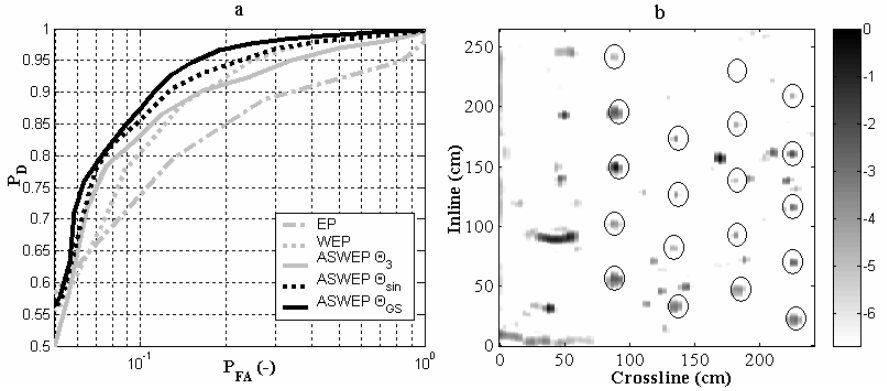

Figure 4.10 The ROC curves corresponding to different projection techniques a); and the confidence map corresponding to the best ROC curve b)

As it was expected, WEP outperforms EP and is outperformed by any ASWEP, including the one that uses the simplest triple-valued mask. The use of the sinusoidal mask produces a map, which marginally better than the one obtained with the triple-valued mask (4.9). The best performance is yielded by the Gaussian tapered sine mask. The confidence map corresponding to this projection is shown in the figure b). Comparing figure b) to the Figure 4.5 a) and b) one can note that the clutter is indeed better suppressed in this case.

4.1.3 Two- and three- dimensional ASWEP

As it can be seen from Figure 4.1and Figure 4.4, targets tend to retain shape of their images in 2D and 3D. To exploit this tendency an expansion of the ASWEP technique to these higher dimensions is needed.

It is possible to view the map resulting from a projection (4.1), (4.2) or (4.8) as L_∞ -norm of a convolution of a focused A-Scan and a kernel function:

$$M(x,y)=\left\|\left[F_{xy}(z)\otimes\Omega(z)\right]^2\right\|_\infty \tag{4.19}$$

where kernel function Ω is equal for the step function for EP, window of a width w for WEP, and a mask $\Theta(z)$ for ASWEP. From this representation of the

ASWEP the expansion to 2D and 3D cases follows naturally. Let us define two-dimensional masks operating in B-Scans:

$$L_y^{2D}(x) = \left\| \left[B_y(x,z) \otimes \Omega_2(x,z) \right]^2 \right\|_\infty \tag{4.20}$$

$$L_x^{2D}(y) = \left\| \left[B_x(y,z) \otimes \Omega_2(y,z) \right]^2 \right\|_\infty \tag{4.21}$$

In (4.20) and (4.21) $B_\alpha(\beta,z)$ defines a strip of a B-Scan along the spatial coordinate β with the spatial coordinate α fixed and $\Omega_2(\beta,z)$ is a two-dimensional mask. Both these operations result in confidence lines $L_\alpha^{2D}(\beta)$. A simple triple-valued 2D mask can be obtained as the direct expansion of (4.9):

$$\Omega_2(\beta,z) = \begin{cases} -1 \quad if \quad (\beta,z) \in B^- \\ +1 \quad if \quad (\beta,z) \in B^+ \\ \quad 0 \quad otherwise \end{cases} \tag{4.22}$$

where B^- defines the negative area and B^+ the positive areas in the mask. For example, consider a 2D ASWEP along the coordinate x with fixed $y = y_0$. Suppose a B-Scan is given and a training target image exists in this B-Scan at the location $x = x_t$ (Figure 4.11 a0). Then at each location $x_0 \in [x_{\min}, x_{\max}]$ the data strip of the width $2r_s$ is defined via:

$$B_y(x,z) = \{(x,y,z) \in C_F : x_0 - r_s \le x \le x_0 + r_s, y = y_0, z_{\min} \le z \le z_{\max}\} \tag{4.23}$$

where C_F represents the focused C-Scan.

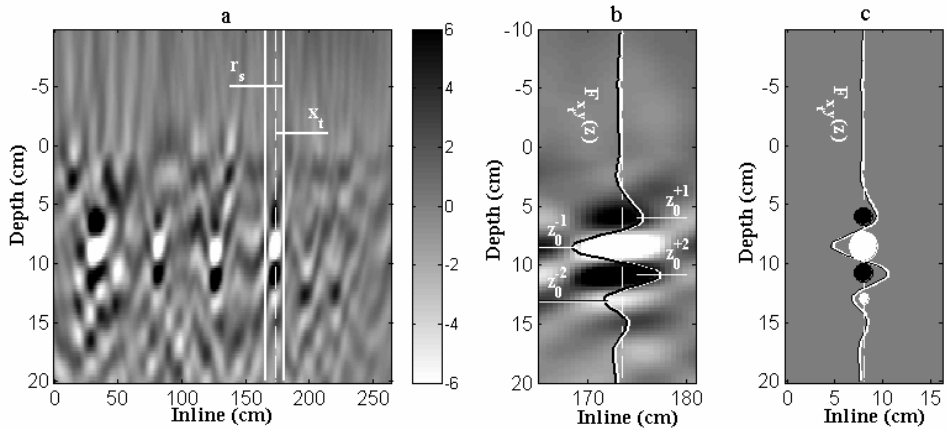

Figure 4.11 Selection of a 2D triple-valued mask: a) the initial B-Scan with a training target image, b) the target image zoomed with 1D representation overlapped, c) resulting mask

The positive and negative areas of the triple-valued mask (4.22) are then defined as collections of ellipses with semi-radiuses r_x^i and r_z^i:

$$B^{\pm} = \bigcup_i B_i^{\pm} = \bigcup_i \left\{ (x,z): \frac{(x-x_0)^2}{\left(r_x^i\right)^2} + \frac{\left(z-z_0^{\pm i}\right)^2}{\left(r_z^i\right)^2} \le 1 \right\} \tag{4.24}$$

In (4.24), x_0 is fixed by (4.23). The depth coordinates $z_0^{\pm i}$ are defined from the focused A-Scan measured at the top of the training target. They are set at the $z-$coordinates of the main extrema of the 1D target image (Figure 4.11 b)). The semi-radiuses $r_z^{\pm i}$ are set equal to the half of the distance between the zero crossings around z_0^i and the semi-radiuses $r_x^{\pm i}$ are set equal to the half-width of the training target. The resulting mask is shown in Figure 4.11 c).

In order to obtain the confidence map the operations (4.20) or (4.21) should be sequentially applied for all B-Scans compounding the C-Scan. This time consuming operation can be considerably speed up if 2D Fourier transform is applied.

The expansion of (4.20) to the 3D case is straightforward. For each point (x,y) one defines a rectangular cylinder $c(x,y,z) \subset C_F(x,y,z)$:

$$c(x,y,z) = \left\{ \begin{array}{l} (x,y,z) \in C_F: \\ x_0 - r_{sx} \le x \le x_0 + r_{sx}, y_0 - r_{sy} \le y \le y_0 + r_{sy}, z_{\min} \le z \le z_{\max} \end{array} \right\} \tag{4.25}$$

where $r_{s\alpha}$ define its spatial sizes and a three-dimensional map $\Omega(x,y,z)$. Then the 3D ASWEP mapping is given by:

$$M^{3D}(x,y) = \left\| \left[c(x,y,z) \otimes \Omega(x,y,z) \right]^2 \right\|_{\infty} \tag{4.26}$$

The definition of a triple-valued mask for the 3D case is made in the same manner as for 2D case. A training target is independently considered in two orthogonal B-Scans crossing at it. Because these B-Scans share the same training A-Scan the depth coordinates $z_0^{\pm i}$ and depth semi-radiuses $r_z^{\pm i}$ are equal for both of them. The semi-radiuses $r_x^{\pm i}$ and $r_y^{\pm i}$ are obtained from the same procedure as above. Then the triple values mask is given by:

$$\Omega_3(x,y,z) = \begin{cases} -1 & if \quad (x,y,z) \in B^- \\ +1 & if \quad (x,y,z) \in B^+ \\ 0 & otherwise \end{cases} \tag{4.27}$$

where

$$B^{\pm} = \bigcup_i B_i^{\pm} = \bigcup_i \left\{ (x,y,z): \frac{(x-x_0)^2}{\left(r_x^i\right)^2} + \frac{(y-y_0)^2}{\left(r_y^i\right)^2} + \frac{\left(z-z_0^{\pm i}\right)^2}{\left(r_z^i\right)^2} \le 1 \right\} \tag{4.28}$$

The computation of the 3D map is prohibitively expensive unless 3D Fourier transform is employed.

The ASWEP mapping made by (4.20) and (4.27) is exemplified on the same dataset as used above. The resulting maps and a-priori ROC curves are shown in Figure 4.12. As it is seen from the figure, the 3D version outperforms the less computationally expensive 2D sequence. On the other hand, both of these mappings are outperformed by the best of the 1-D procedures using the tapered sine mask. It should be noted, however, that not every dataset permits modeling of all targets with just one fine tuned mask. In such cases only simpler triple-valued masks are applicable and then 3D ASWEP produces the best results.

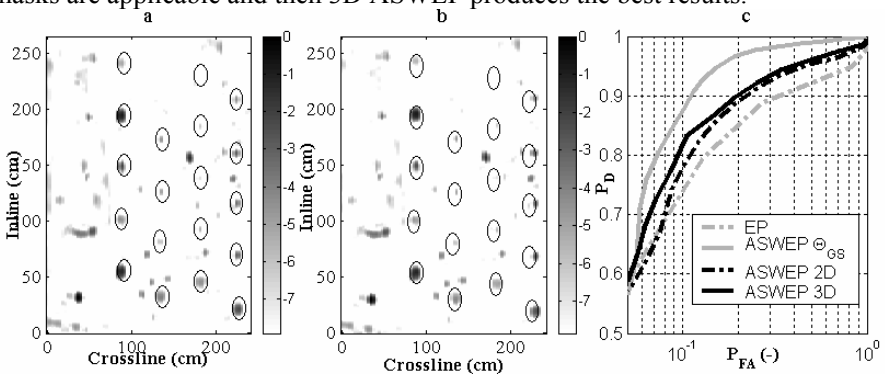

Figure 4.12 ASWEP mappings: a) 2D sequence, b) 3D, c) corresponding ROC curves

4.1.4 Modification of ASWEP for cross-polar radar

In this subchapter I consider a cross-polar C-Scan focused by the SAR given via (3.17). Most of the targets of interest (Table B1 and B3 Appendixes B.1 and B.3) are electromagnetically symmetric or close to symmetric and therefore their images obtained with (3.17) – (4.1) sequence have structure drastically different from co-polar channels. The difference is such that the construction of a confidence map complying with the definition taken in Chapter 2.1.2 from this C-Scan becomes a non-trivial task. This task can be resolved using the 3D extension of the ASWEP made in Chapter 4.1.3.

To explain the distinctive nature of the target images in cross-polar radar scenario consider a monostatic cross-polar B-Scan made over the top of a training target. Suppose the target is electromagnetically symmetrical. The probing pulse excites the target and it scatters back an electromagnetic wave with the same polarization. This wave is polarized exactly orthogonal to the receive antenna and in this case the electromagnetic scattering theory predicts [86] that no scattering would be recorded. Now take into consideration two aspects of imperfectness of the described model: a) transmit and receive antennas do not physically coincide and b)

the B-Scan is taken not exactly above the symmetry line of the target. In the case of the IRCTR radar the antenna separation in quasi-monostatic mode is quite small and the C-Scans are measure on a quite dense grid. As a result almost no scattering occurs when the transmit/receive antenna system is positioned over the top of the target. Nevertheless, the imperfect symmetry of the real system causes scattering phenomena to be recorded as the system moves away from the target. More precisely, the receive antenna records the portion of the energy scattered by the target. This energy is proportional to the cosine of the angle between the polarizations of the field scattered by the target and the receive antenna. This angle becomes nearly orthogonal as the antenna system moves across the target itself and the corresponding cosine changes the sine on the sides of it. This process is illustrated in Figure 4.13 a), where a portion of a B-Scan acquired over a PMN2 mine is shown. As it is seen from the subfigure, the typical hyperbola-like target traces have the following peculiarity: the wings of the hyperbolas have different polarity and their apexes are not visible. The B-Scan acquired in the orthogonal direction has the same nature. Application a SAR procedure defined by (3.17) to such data results in a very specific target image. As it is seen from b) there is no energy at the center of the target and the typical collections of bulbs are duplicated on the sides of it. A 3D image of a target then consists of four sets of bulbs of interchanging signs. Any one-dimensional projection of type (4.19) results in a map where the target images have the shape shown in c): no signal in the geometric center of the target and four local maxima placed on the diagonals of the four quadrants.

The LM detector introduced in 2.1.3 does not detect such targets. Moreover, the necessity to take into account four bright points per targets leads to complications since the detection result becomes non-unique.

Luckily, the 3D extension of the ASWEP allows construction of a mapping that constructs maps with typical target images. To this end one needs to construct a mask that computes the confidence in a given location (x, y) considering the brightness levels observed in the neighboring A-Scans. Such a mask would essentially repeat a typical 3D contour of a target image. For example, the triple-valued mask given the collection (4.27) can be successfully used. The ellipsoids of constant sign corresponding to the map are given by:

$$B^{\pm} = \bigcup_{j=1}^{4} \bigcup_{i} \left\{ (x, y, z) : \frac{(x - x_0 - x_s)^2}{(r_x^i)^2} + \frac{(y - y_0 - y_s)^2}{(r_y^i)^2} + \frac{(z - z_0^{\pm i})^2}{(r_z^i)^2} \le 1 \right\} \quad (4.29)$$

where x_s and y_s are shifts that compensate for the absence of the energy in the geometrical center of the target. As it is seen from (4.29) there are 4 collections of ellipsoids that constitute the mask.

Despite the fact that the discriminative power of the constructed map is not too high this feature adds valuable information due to the very peculiar covariation with corresponding co-polar channel.

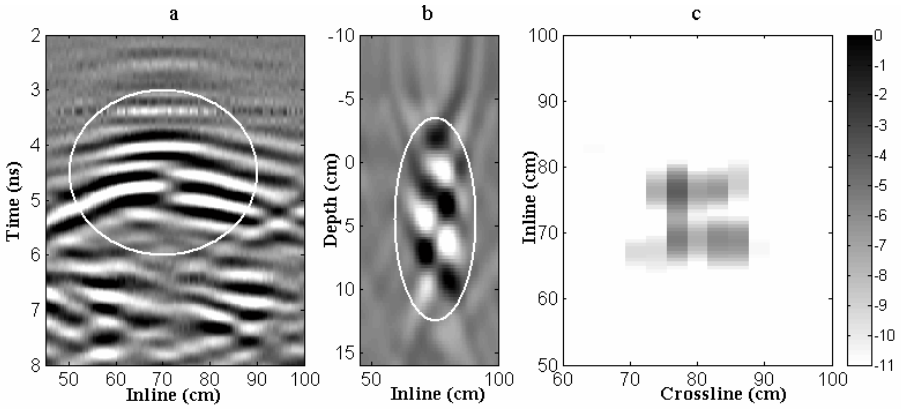

Figure 4.13 Cross-polar images of a symmetrical target: a) B-Scan after background removal; b) the same B-Scan focused; c) energy image of the mine

4.2 Auxiliary features

As it was mentioned in Chapter 2.1 where the data processing and target detection scheme was established, every confidence map built on the basis of some decisive feature may provide one or several additional features. In the present subchapter I consider the auxiliary features of two types: the ones based on the local statistics of the map and the ones defined from other sources of information using the exact location defined by the detection in the map.

4.2.1 Features based on local statistics of confidence maps

As it is often mentioned in GPR-related literature, the local statistics of the map M in the vicinity of a point (x, y) is capable to provide much more information than a single value $M(x, y)$ [13, 14]. The image histogram is a natural source of this information, which does not assume any model of brightness distribution. In order to use this source of information it is necessary to define the term 'locality' itself consistently for all targets. The data processing schemes considered above result in the confidence maps and lists of detection coordinates defined in them. The targets in these maps are normally imaged as spots where a decisive feature takes higher values. This, in turn, results in higher brightness in the vicinities of detections (for examples see projection maps given in several figures in Chapter 4.1). These spots have ellipsoidal shape and therefore the first task is to define the semi-radiuses of these ellipses.

The task cannot be solved by setting a hard threshold because of different sizes of the target images. To resolve this ambiguity I use *N-dB* elliptical vicinities of a detection point (x, y):

$$V_N(x,y) = \left\{ (\xi,\gamma) \in M : 20\log 10 \frac{M(x,y)}{M(\xi,\gamma)} \le N \right\} \tag{4.30}$$

The construction of detections by local maxima detector guarantees, that the vicinity defined by (4.30) is never empty for any detection and any chosen *N*. The most representative choice for the value of *N* depends on the processing applied and is made using the training set. The contradicting factors determine the value of *N* are: a) maximum coverage of target images; and b) minimal inclusion of the surrounding clutter for the target images. The former factor causes *N* (and physical dimensions of the vicinities) to grow, while the latter one bounds this growth. I use the following practical rule for selection of N:

$$N = \min_{U_T} \left\{ N_k : I_k \subset V_{N_k}(x_k, y_k) \right\} \tag{4.31}$$

where I_k is the image of the k^{th} target in the training target subset U_T; (x_k, y_k) are the coordinates of the corresponding detection. In most of the considered situations *N* has been taken in the vicinity of 4 to 8 dB to the local maximum. The definition of the elliptical *N*-dB vicinity is completed by computation of the corresponding semi-radiuses. Because most of the targets are symmetrical these radiuses depend mostly on the grid resolution in the in-line and cross-line directions. The statistics of the confidence map computed locally for elliptical vicinity defined by (4.30)-(4.31) produces some auxiliary features, that should improve the target detectability.

Median and inter-quantile range. The most robust description of the local statistics is confined to the centrality and spread of the local image brightness [88, 89]:

$$\eta_1^k = median\{db[M(V_N)] - db[M(x_k, y_k)]\} \tag{4.32}$$

$$\eta_2^k = IQR\{db[M(V_N)] - db[M(x_k, y_k)]\} \tag{4.33}$$

where $db[\ ]$ means transformation of the map to the amplitude decibels format relative to the local center. Expressions (4.32) and (4.33) represent the local centrality and spread of the image in the vicinity of the k^{th} detection by it median and inter-quantile range respectively. The latter is computed as a difference between 75 and 25 percentiles of the data. In principle, this information is also contained it the first two moments the local histogram. But it is known [87] that the measures I have chosen here are more robust when the outliers are probable on one of the ends of the histogram. In the case under consideration the right side of the histogram is

bounded to zero and the left is subjected to the random bursts, which may result in the outliers.

The application of the proposed technique of construction of auxiliary features is exemplified in Figure 4.14 where the same dataset as in Chapter 4.1 is used. The scatter plot of the medians of local histograms versus the inter-quantile range is given in the subfigure a). Despite the significant intersection of the classes, introduction of these auxiliary features improves the detectability of APM, as it can be seen from the subfigure b). The subfigure b) shows the obtained improvement in terms of the a-priori ROC curves computed for the energy (4.1) alone and the {energy, local median, local IQR} triple. The fusion is made via the quadratic rule (2.29). The data corresponding to the clutter and target classes were simultaneously quasi-normalized via the Johnsnons transform (see Chapter 1.1). The final distributions were obtained through the density estimation technique (2.7)-(2.8).

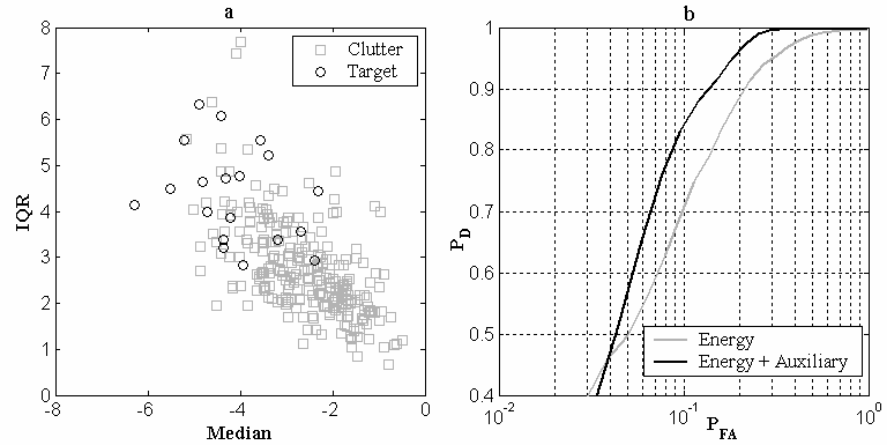

Figure 4.14 Auxiliary features: centrality and spread of the local brightness; a) scatter plot of the auxiliary features, b): a-priori ROC curves for the main and main supported by the auxiliary features.

Geometrical moments. The alternative to the described above way to take into account the local statistics of the target images is consideration of its local geometrical moments. The geometrical moments g_{pq} of the image bounded by the *N*-db vicinity around the point (x, y) are given [90] by:

$$g_{pq} = \iint_{V_N} (x - x_k)^p (y - y_k)^q M(x, y) dxdy \tag{4.34}$$

There is a principal difference of the information provided by geometrical moments defined by (4.34) from the information obtainable from local histograms as

described above. Namely, (4.34) takes into account distribution of the brightness on the surface of the map, i.e. it is essentially two-dimensional whereas (4.32)-(4.33) were one-dimensional entities. The full set of the moments computed according to (4.34) with $p,q = 0:\infty$ fully describe the image [90]. Each of them presents and auxiliary feature that can improve mines detectability. The question of optimal choice of the amount of features (moments in particular) is considered further in subchapter 4.3.

4.2.2 Non-statistical features

Another source of the additional information that can be obtained from the confidence map is consideration of values associated with coordinates of the primary detection. For example, such features were considered in the dissertation of Dr. Frank Cremer [51] as the basic feature vector for the GPR detection. In the given study the object depth z_0 (the value, which maximizes (4.2)), the radius of *N-db* r_N vicinity, and the LSM measure (3.5) corresponding to this depth are used as non-statistical auxiliary parameters for the WEP map. It is very important to take into account that the relationship between the WEP value, the object depth, and the radius r_N is not quadratic. A functional relationship describing the interconnectedness of these features is based on the physics of the scattering: the larger (or more contrast) objects are likely to produce larger values for r_N and WEP values. As it was observed in [76] the energy values associated with targets as a function of the burial depth has a local minimum near $z_0 \approx 0$. I.e. the observed energy of the flush buried targets is lower than the energy of the mines buried at the depth of ~6 cm (see the fig and the relevant discussion in subchapter 3.1.1). Of course the energy of the targets buried even deeper is lower still. The WEP value as the function of the depth has the same properties. The presence of the local minimum at around 0 depths precludes one from introduction of depth into a quadratic classifier. Indeed, fitted quadratic classifier with local minimum at 0 expects targets placed deeper into the ground to have larger EP and WEP values, which contradicts both electromagnetic theory and common sense. Therefore it is unreasonable to include the {depth; WEP value} pair of parameters into the feature selection list for a quadratic classifier. In order to take advantage of the available information on the burial depth it is necessary to build a model, which takes the depth and WEP (Or any other brightness-related parameter) value of the target as parameters and returns a scalar value representing the resulting confidence. Such a model can be constructed using typical brightness (WEP, ASWEP, etc.) values observed as a function of depth at training sites. If $w = f_M(z)$ is a target brightness value representation as a function of the burial depth, the model sought model is

$$W = P[w_o(z) - f_M(z)] \tag{4.35}$$

where P is a penalty functional similar to the ones described in 1.1 and w_o is the actually observed brightness of the target at the depth z. The resulting confidence $W(w_0, z)$ is a scalar value depending on the observed brightness and depth that can be profitably presented to a quadratic classifier.

4.3 Procedure to determine optimal features

The length of the final feature vector is a very important factor in the present problem. The optimal length is determined by the two contradicting factors. On one hand, presumably the more parameters are allowed into the classifier, the more information is fed and therefore the target/clutter dichotomy is better. On the other hand, introduction of each extra parameter into the classifier may negatively affect the classifier performance on the test site. I.e. the best possible target/clutter dichotomy achieved at a training site may mean overtraining of the classifier and its breakdown at a testing site where it becomes a plug in rule. Moreover, introduction of each new feature requires enlargement of the training site, including training targets and training friendly objects. As the very minimal requirement (necessary in a sense of linear algebra) one has to posses at least *K+1* training objects for building a quadratic classifier that uses a feature vector of the length *K*. As it is pointed in the statistical literature [45, 69] *3(K+1)* objects are desired. Therefore the length of the feature vector available for the user is very much limited with the size of the training site. The IRCTR GPR produces 8 or even 16 energy maps at one sweep [29] before any sophisticated data processing scheme has been applied. Therefore for the case of this study the main problem is the selection of the features that can be discarded and those which should be retained.

A Smith's procedure of forward selection [smith] is used here to determine the best possible feature collection. The procedure of selection of *k* best features to be retained from the initial pool of $p > k$ available ones reads:

1. Conduct *p* univariate target-clutter dichotomies and select the one that provides the best detection; fix the set of the retained variables as $\{v_1\}$

2. Conduct *p-1* bivariate target-clutter dichotomies using pairs $\{v_1, f_j\}$; select the pair providing the best detection and fix the set of the retained variables as $\{v_1, v_2\}$

3. Conduct p-2 trivariate target-clutter dichotomies using triples $\{v_1, v_2, f_j\}$; select the triple providing the best detection fix the set of the retained variables as $\{v_1, v_2, v_3\}$

4. Continue until achieving of the subset of length *k*.

This strategy provides the set of variables of the given size in reasonably fast time as $k\left(p-\frac{k-1}{2}\right)$ dichotomies should be provided and compared. E.g. for fairly typical values of $p = 25$ and $k = 4$ a total of *94* dichotomies should be searched. Of course a much more time consuming straightforward alternative exists. Given time it is possible to provide an exhaustive test of all possible combinations of parameters and select the best combination. The problem with this brute force approach is primarily the computational time: a total of C_p^k dichotomies should be performed, which for the same values as above results in *12650* tests. The total numbers in both approaches can be lowered considering some a-priori information available for the researcher, such as: usually similar features coming from both mutually orthogonal channels of the radar should be retained; the (AS)WEP applied to the results of the PLSM are typically the most informative features and should be retained etc.

The forward feature selection process is illustrated he with the set of data acquired at a sandy lane during the measurements campaign of summer 2002 [91-93]. The site and measurements set up can be found in the Appendix B.1 . Here I start with the dataset consisting of 3 co-polar C-Scans in two mutually orthogonal co-polar quasi-monostatic channels (T1R2 and T2R1) and an additional co-polar bistatic channel (T1R4). These data have been processed according to the two data processing schemes: in the scheme A the clutter was suppressed with MWAE (2.2), the data were SAR-focused, and the maps were obtained with the 3D ASWEP (4.27); in the scheme B after the MWAE the clutter was additionally suppressed with PLSM algorithm (3.14), the data were SAR-focused and the maps were obtained with the trimmed sine 1D ASWEP (4.14). The parameters for the PLSM procedure have been taken using the data acquired at the same spot as it is described above by expression (3.17). The goal of the FFS process is set here to come up with the optimal feature vector of the dimensionality four.

The 6 initial maps are shown in Figure 4.15 where the targets are encircled. The brightness of the figures is tuned in such a way the in each of the maps the weakest of the targets is just visible. The challenging false alarm objects here are the barbed wire centered at the 80 cm in-line and 15 cm cross-line, the metal disk at (28,10), the metal ball at (140,150), the brick at (170, 30) and to some extent various TDR sensor appearing at different coordinates. Note that this is an open field test which must result in the features that divide the targets from the friendly objects in the best way and it is not a target detection exercise.

Based on these maps one at a time I detect targets and build a-posteriori ROC curves for the individual detection schemes. These ROC curves are shown in Figure 4.16 a). As it can be seen from the figure, the best feature for this particular case clearly is the ASWEP map of the data coming from the quasi-monostatic co-polar channel T1R2 through the scheme B. This feature produces 6 false alarms at

the 100% level of detection, which is the minimal amount among the six. In order to ensure the optimal performance of the ML based quadratic classifier I normalize each of the features using Johnsons transform as in (2.50-2.51). After ensuring that all the individual features are normally distributed I organize the pairings of the best feature with the other five.

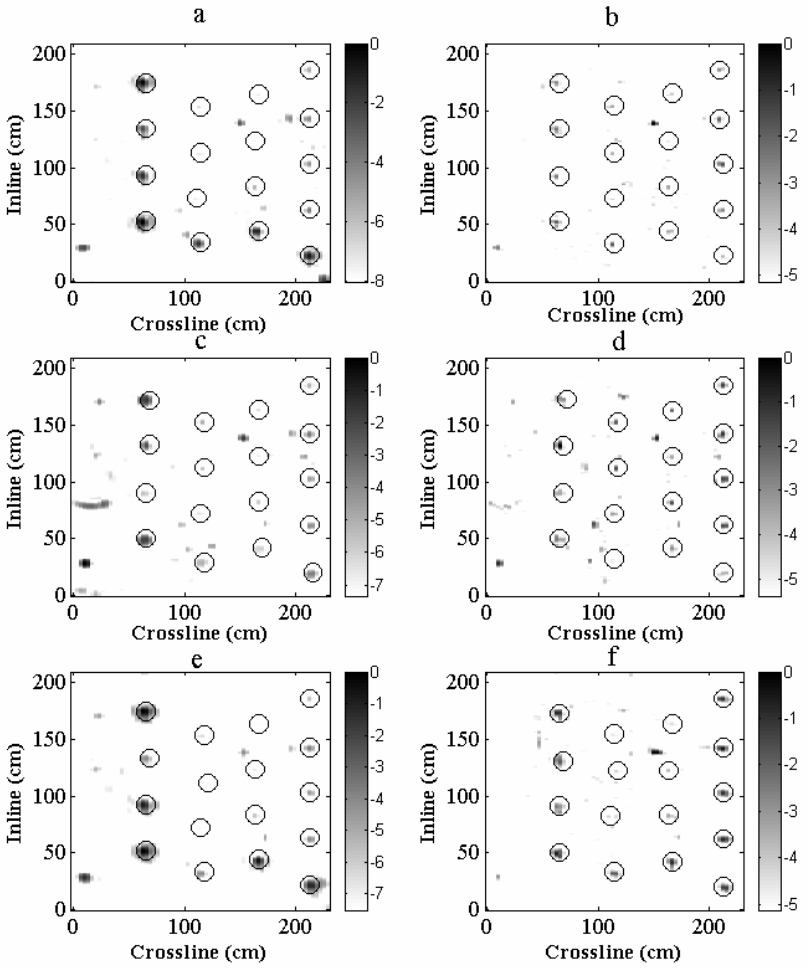

Figure 4.15 The individual feature based confidence maps: a) T1R2-A, b) T1R2-B, c)T1R4 – A, d) T1R4 – B, e) T2R1 – A, f) T2R1 – B

The ROC curves resulting from these operations are shown in Figure 4.16 b). Again the best pairing is easily selectable as the data coming from the bi-static co-polar channel T1R4 processed according to the scheme B. The best pair produces only 2 false alarms at the 100% level of detection. Fixing the best pair of features, I repeat the procedure of selecting the best possible triple of the features. The resulting ROC curves shown in Figure 4.16 c) allow the selection of the feature that forms the best triple. As it is seen from the figure the data coming from the quasi-monostatic co-polar channel T2R1 through the scheme A allows no false alarms on the 90% levels of detection and just one false alarm on the 100% level of detection. On the final step I check the three possible quadruples in attempt to define the optimal feature vector. However, as it can be seen from the Figure 4.16 d) all three possible ROC curves are indistinguishable. Moreover, these curves do not improve the best of the triple feature based ROC curves. This means that in the given case any or no remaining feature can be taken as the fourth producing the same result: one false alarm at the 100% level of detection and no false alarm if 16 out of 17 targets are detected.

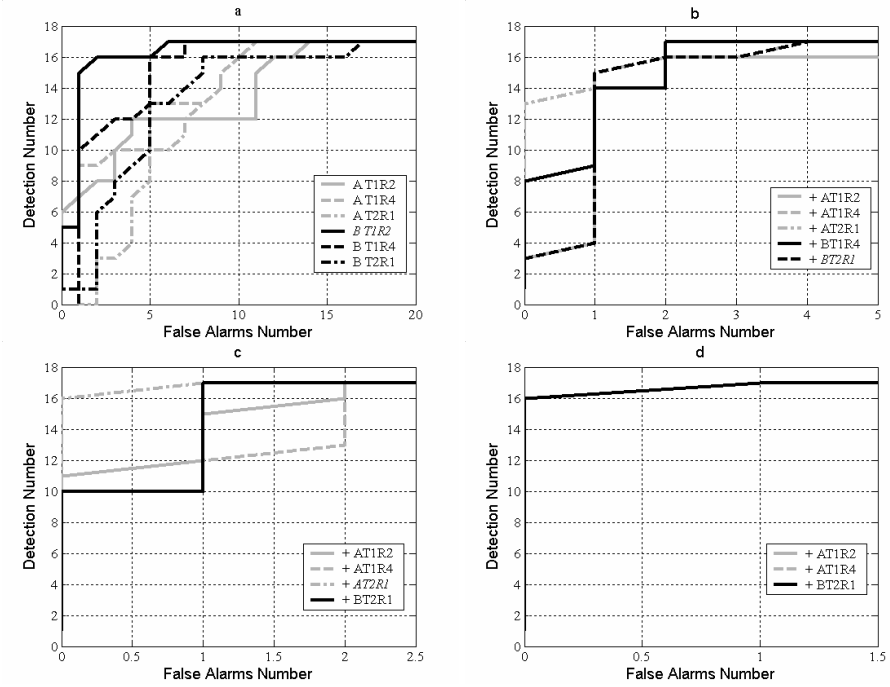

Figure 4.16 The a-posteriori ROC curves for a) individual features; b) pairs of features; c) triples of features; d) quadruples of features. The best (combination of) feature is depicted in italic in the legend.

4.4 Conclusion for Chapter 4

In this Chapter I have presented the ways of forming and selecting the decisive features for the target/clutter dichotomy. The scope of the chapter includes descriptions of the originally developed WEP/ASWEP projection techniques, which allow construction of the better confidence maps than those of the conventional energy projections. The 2-D and 3-D versions of the ASWEP are shown to provide the better maps in most of the circumstances except of 2 cases: a) 1-D when images of all the targets that can be encountered at the given site can be represented by a single wavelet, such as a tapered sine signal, this representation and 1-D ASWEP should be used; b) if a PLSM/SAR superposition has been applied to the dataset, 1-D WEP should be used.

Moreover, use of the WEP/ASWEP provides the most probable depth of the object burial as an auxiliary feature. The use of this auxiliary feature is described in 4.2. Besides other auxiliary features, which are statistically bound, are described in that subchapter. Finally, two alternative procedures for selection of the best features for the target detection are described in 4.3.

Chapter 5 Improvement of the Mine Detection Provided by the Advanced Techniques

In this Chapter I apply the methods described in the chapters 2 – 4 to the data acquired during the two measurement campaigns held in Summer 2002 and Autumn 2004 [77, 79] and compare the obtained results against the detection of the mines with conventional methods and where possible against the results described in the literature [49, 51, 94]. The measurement campaigns themselves are documented in the Appendixes B and C. In this chapter I describe the application of the techniques and methods presented in the previous chapters to the data acquired. The general paradigm of the data processing and target detection on a test site follows the description:

1. A training set is selected
2. A set of data processing schemes is applied to the training set
3. The forward feature selection scheme is executed to obtain a set of decisive features
4. A target detector is built on the basis of the data acquired over the training set using the features retained as a result of the selection process 3
5. The dataset acquired at the test site is processed to obtain the features of the step 3
6. The target detector is applied as a plug-in rule to detect the targets
7. An a-posteriori (detection percentage vs. FA density) ROC curve is built.

I always compare the obtained results to the ones obtainable using conventional energy-based schemes and to the results of other authors where it is possible.

5.1 Application to the data from MC'02

The measurement campaign of summer 2004 has been executed at the specifically designed measurement site built for the testing of mine-detection equipment. The description of the measurement sites and set-ups as well as the technical description of the execution of the campaign are described in the Appendix 0. In this subchapter I describe the results of the application of the techniques presented in the Chapters 2 – 4 to the data acquired.

5.1.1 Dry sandy lane

The case of a mine-field organized in dry sand is often referred to as an easiest possible scenario. This may be true in comparison to the more challenging types of soil. This means that the detection of all targets should be accompanied with as little as possible false alarms. As it is described in the literature, previous

attempts at this site resulted in quite promising results, surpassing which is set as the goal here.

The description of the sandy lane with the objects placed there and measurements set-up are given in the Appendix B.1 . As it is seen from the measurement setup description given in appendix, the following primary features can be obtained:

1. Target brightness (in the form of EP, WEP or ASWEP in 1D, 2D, and 3D) in mono- and bi- static co- and cross- polar channels;
2. Target brightness (WEP of ASWEP 1D, 2D, and 3D) in maps obtained from PLSM - processed data.

Moreover, the following auxiliary features are obtainable:

3. Depth of the target burial
4. Local geometrical moments of order [0,0] to [1,1] and histogram spread computed in the maps obtained in steps 1 and 2
5. Radiuses of the N-dB vicinities for the maps computed in 1 and 2.

Using 6 out of 8 receive channels (dropping bi-static cross-polar configurations) one obtains 60 primary features, each accompanied by 7 auxiliary parameters. The grand total of 420 features is unacceptable even for the forward selection procedure. In order to pre-select the most promising features the following initial set of features is considered at each time:

1. Geometrical moment of the [0, 0] order for the WEP-based maps are combined with the burial depths into the model parameter (4.35) for the base-line processed data. This results in 6 scalar parameters describing energy characteristics of detected objects.
2. Geometrical moments of the [0, 0] order for the 3D-ASWEP-based maps are computed for the PLSM-processed data from co-polar channels. This results in 4 scalar parameters relying mostly on the waveform of object responses

These ten scalar parameters are fed into the forward selection procedure with the goal to select the best four. The length of the feature vector is selected equal to four because of the limited size of the training set I have available. More precisely, the training set may consist either from certain amount of mines that are placed at the sandy lane itself or from the nine mines used at the subsequent measurement campaign held in 2004, or their mixture. All three cases model different practically important research situations:

1. A researcher has no access to the measurements in the controlled condition but has limited training set acquired in the conditions identical to those of the test site;
2. A researcher has only the training data obtained in the controlled conditions, which are similar but not identical to those peculiar to the test site;
3. A researcher has both a dataset acquired at similarly conditioned site and a small dataset identical to the training site.

The resulting best features and the results of the detection themselves could be different for these cases and therefore I am exploring all three possibilities.

To model the first case I use a second of the spots measured at the sandy lane (S2, see the details in Appendix 5.1.1) as training data. This dataset contains 6 specimens of mines of the same type as in the test site and a large number of false-alarm generating objects, both specifically and sporadically placed. The selection of this dataset provides a very good approximation for the reference wavelet and allows the use of fairly strict penalty functional in the PLSM-based clutter suppression. On the other hand, the limited size of this dataset makes it difficult to build a well-performing maximum likelihood quadratic detector. Therefore it is expected that maximum deflection detector should perform better at the test site. These assumptions tested on the measured data provided the following results. The fitting procedure (3.10)-(3.12) for penalty functional parameters definition for the PLSM processing (3.14) resulted in the values of $m_0 = 1.4$ and $m_1 = 0.9$ for all four co-polar channels.

Application of the PLSM-SAR-3DASWEP sequence with these parameters and base-line to the training data acquired in results in the four initial features (scheme B). Application of the SAR-WEP/Depth Model sequence to the co-polar and the mono-static cross-polar channels adds 6 more features to the initial pool (scheme A). The a-posteriori ROC-curves resulting from individual detection based on these features are shown in Figure 5.1 a).

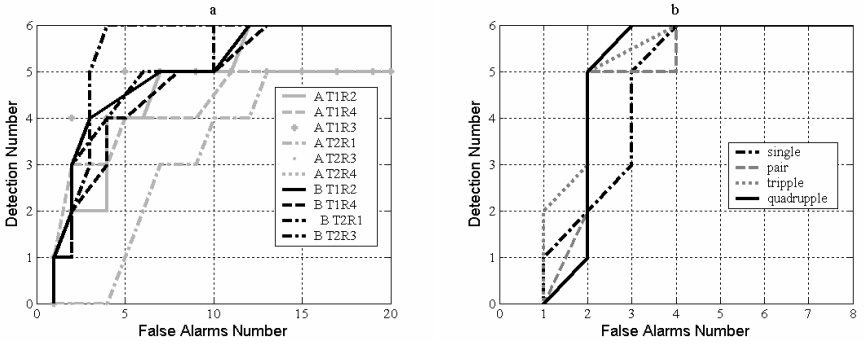

Figure 5.1The ROC curves representing the target/clutter dichotomy on the training dry sand site (scenario 1): a) individual feature detection, b) best combinations

As it can be seen from the figure, the data coming from co-polar quasi-monostatic channel T2R1 processed via the scheme B) provide significantly better separation of the target/clutter than the other features. It is taken as the basis feature and the forward feature selection process starts with checking the possible pairs. The classifier (2.33) based on the maximum deflection criterion is used for the feature fusion due to the fact that it allows the smaller training dataset than the one based on the maximum likelihood. The features were pseudo-normalized using

the Johnson's transformation. It was found that for this case the S_L transform produces well-acceptable results. The PLSM-processed bi-static channel T2R3 is found to be the best 2nd parameter. The better performance of the system with the second transmit antenna should be explained by the placement of the training targets closer to the border of the view of the radar/scanner system. The mutual displacement of the transmit antennas results in that one of them provides better overview of the measurement site and hence the better results. The T1R2 and T1R4 channel data processed in the same way are found to be the best 3rd and 4th features. This selection is probably due to the limited size of the training site and the very well established parameters of the penalty functional. Application of the 4-parametric MD-based quadratic classifier to the training site provides 100% detection with just 3 false alarms (Figure 5.1 b)). This classifier will be referred to as sand-Q1 below.

For the case of no training data acquired over the test site, one solely relies on the data obtained at the controlled conditions. For the considered case this means the use of the data from the measurement campaign held in the autumn of 2004 at another test site [80]. This campaign is detailed in the Appendix 1.1 and the scenario 1 from it is used to obtain the training data for both the PLSM processing and the target and clutter covariance matrixes. Using a wavelet measured over the tops of several mines and the procedure (3.11)-(3.12) I obtain the penalty functional parameters $m_0 = 1.7$ and $m_1 = 1.5$. They are more relaxed in comparison to the previous case, which is a positive factor since I expect that the reference wavelet is slightly different from that measured at the exact test site. Like in previous case I use the PLSM-SAR processed co-polar mono-static data as the base for the forward selection procedure. This time, however, the training set is large enough to allow ML criterion based quadratic classifier. In order to improve the results it provides I pseudo-normalize the features using the joint Johnson's transform-based normalization procedure (2.51)-(2.55).

The a-posteriori ROC curves corresponding to the results of the target detection on the basis of individual features are given in Figure 5.2 a). As it can be seen from the figure the best detection is again provided by the data from the T2R1 channel processed via the scheme B.

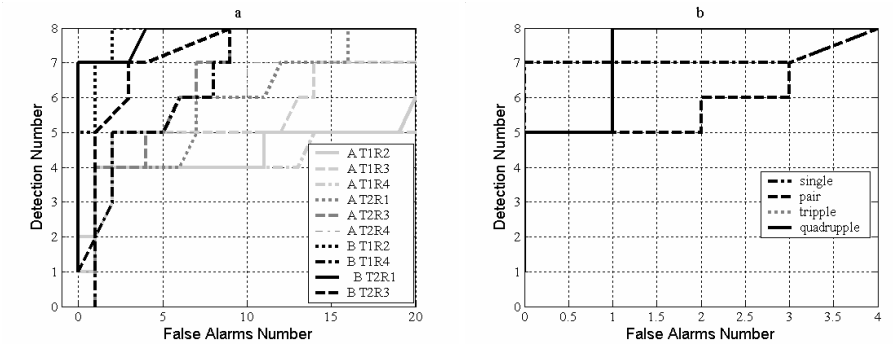

Figure 5.2 The ROC curves representing the target/clutter dichotomy on the training dry sand site (scenario 2): a) individual feature detection, b) best combinations

Organizing the forward selection procedure I obtain the second and the third retained features: T1R2 and T2R3 channel data processed by the scheme B. However, it was found impossible to improve the detection level further by addition of the features. As it can be seen from the Figure 5.2 b) the best ROC curve based on four features coincides with the best triple. Application of the ML based 4-parametric quadratic classifier, which will be referred to as sand - Q2, to the training site provides 100% detection with 1 false alarm.

Finally in the best possible case where both training subsets are available I am using the small dataset collected at the identical site to build the penalty functional, the MC'04 data to build the target covariance, and the mixture of the two to build the clutter covariance:

$$Cov^3_{\text{target}} = Cov^2_{t\arg et}$$

$$Cov^3_{\text{clutter}} = \frac{1}{2}\left(Cov^1_{\text{clutter}} + Cov^2_{\text{clutter}}\right) \tag{5.1}$$

This choice is dictated by desire not to use where it is possible the same target-related data for building the reference wavelet and penalty functional and the covariance matrixes. The PLSM parameters remain unchanged in comparison to the first scenario and the covariance matrixes tend to change not too significantly for the most of the features comparing to the second scenario, which suggests the validity of the plug-in rule approach for the given situation. The pseudo-normalization of the features and ML-based fusion is made analogously to the case 2. The forward-looking procedure suggests the same PLSM-processed data as the best features. The application of the resulting quadratic classifier (sand-Q3) to the training data from the scenario 2 results in 100% detection with 5 false alarms. The additional false alarms appear in this case due to the disruption of the clutter covariance matrix made by the addition (5.1).

Now let us apply the three quadratic classifiers obtained above to the test data. The data, which is taken as a blind test here has been acquired at the spot S3 of the

dry sandy lane (see Appendix B.1). The same data was used to exemplify the forward feature selection procedure in Chapter 4.3. Unlike that case here the classifiers are obtained without use of any information collected at this spot. The a-posteriori ROC curves corresponding to the three classifiers are shown in Figure 5.3.

As it can be seen from the figure, all three classifiers outperform the best of the results available using the base-line processing. As it was expected, the classifier, which does not use any information from the site of the test measurements, produces the poorest of the results yielding 11 false alarms (Q2). On the other hand, the classifiers that were allowed to take into the training the data from the spot adjacent to the test site produce a 100% detection with only 6 false alarms. The classifier Q3 seems to outperform the classifier Q1 but the difference is insignificant.

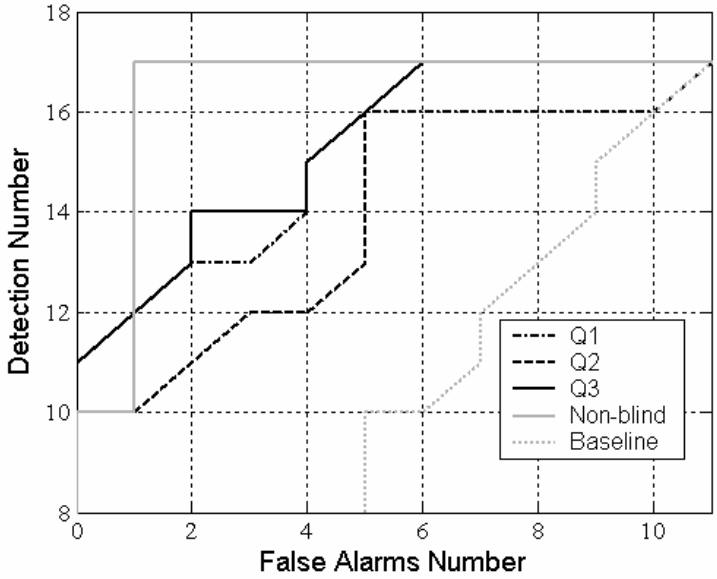

Figure 5.3 A-posteriori ROC curves for the quadratic classifiers Q1, Q2, and Q3;

The application of the procedures suggested in this thesis to the test data results in the significant improvement of the performance of GPR system. In [51] the same FA rate is reported for the test site and for the test site 100% detection level was not reached. In [49] approximately the same FA rate is reported for the case where part of the test data is used for the training. The positive development seen in the present work lies in the use of a quadratic classifier rather than LVQ (which is a development of the nearest neighbor method) or multi-level reasoning system.

A simpler quadratic classifier is (presumably) better suited for use as a plug in rule (i.e. to be trained at one site and used at another, similar but not identical).

5.1.2 Wet sandy lane

As it is seen from the description of this measurement site and setup given in the Appendix B.2 the 0.8 ns generator has been used at it. The lengthier probing pulse was used to ensure better penetration of the electromagnetic energy into the supposedly more dissipative ground. This approach has its drawbacks as the PLSM based clutter suppression proved to be not very profitable for this scenario and moreover non-uniform moisture of the ground lead to disruption of the hyperboloid traces left by objects. Overall, application of GPR in these conditions is very difficult. On the other hand, it is easy to see the superiority of the projection techniques and methods of fusion given in this work.

Here I treat measurement spot # 2 as a training data subset and measurement spot # 1 as a test data subset. As there were no measurements on the moist sand during the subsequent measurement campaigns and thus no wet-sand data are available I consider only this one scenario.

The cross-polar channels do not provide informative maps in this case and therefore only co-polar ones are considered. Moreover the burial depth cannot be used as information source since a) the brightness of objects depends mostly on the local contrast, which for this case is a function of the random environment rather than of object composition, and b) the burial depth is very difficult if possible to evaluate for the non-uniformly moistured sand. Thus the initial features are WEP and ASWEP values associated with the detected objects. Together they form eight initial features and three are retained through the forward selection process.

Thus the forward selection procedure starts here with the selection of the best singular feature and continues through all steps to arrive at the best feature vector of length three. The feature pseudo-normalization using Johnson's transform is made only for the clutter and the MD based classifier (2.34) is used for the feature fusion. This choice is again dictated by the limited size of the dataset. The forward selection process results in the WEP-values obtained in the channels T2R1, T2R3, and T1R2. The preference shown by WEP projection over the ASWEP one is probably caused by the instability of the shape of target image in focused A-Scans. The instability is in turn caused by a non-homogeneous moisture composition of the hosting soil leading to wide variability of its dielectric permittivity.

The application of the classifier (2.34) built on the previous step to the test data provides the result shown in Figure 5.4. It must be stated that GPR should not be used under such heavy moisture conditions (16% of moisture in certain parts of the lane [99]) in attempt to locate anti-personnel mines of the M14 and NR22 type. Results obtained by Rhebergen et.al [100] suggest that the moisture of this magnitude should be gone from a sand site in a matter of days if not hours and the demining attempts should be delayed untill this term. Nevertheless, application of

the techniques presented in this thesis allows increase of the detection percentage and more than a two times reduction of the false alarm rate at 85% detection rate in comparison to the base-line detection. Moreover, the PMN2 mines are detectable even in such conditions and the false alarm rate is lowered 1.7 times at a 100% PMN2 detection rate. There are no published results for the work provided in the same or similar conditions and therefore no external comparison is possible here.

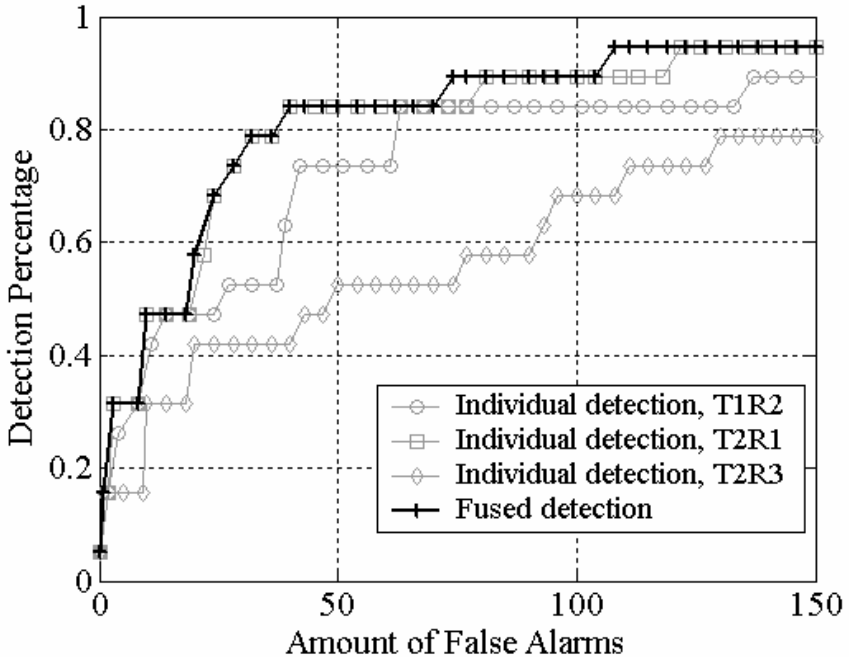

Figure 5.4 The ROC curves for the wet sand case. Individual feature based detections and the result of the Maximum Deflection based fusuion.

5.1.3 Grass lane

The Grass lane, as it is shown in the Appendix B.3 , is covered most extensively, which resulted in three different datasets. The two of these datasets are used as training sites and one as a blind test site. As each of the datasets was measured with 16 different radar scenarios the initial set of the features is very large. The main difficulty in this case is the presence of mines of the butterfly type (PFM1), which significantly differ from the PMN2, M14, and NR22 types in their scattering properties. Because of this their PLSM scores may deviate very significantly from those expected for the rest of the mines. On the other hand, their contrast is much higher due to the high metallic content and therefore their detection with base-line detection scheme improved at the stage of projection should be easier. This further

embarrasses the pre-selection because in this case unlike the sandy lane the waveform-based clutter suppression may or may not provide the best possible results. Therefore all of the initial features should be treated equally. In order to make the feature selection a feasible process the following features are hand-picked by me on the basis of the 'hands-on experience' to compose the initial pool:

1. Geometrical moments of [0 0] order computed for 3D ASWEP maps combined with the depth information computed for the co-polar channels and probing signals of two different durations (8 features)
2. 1D ASWEP values computed for the PLSM-processed co-polar datasets acquired using 0.5 ns pulse generator (4 features)
3. 2D cross-polar ASWEP values computed for the data in mono-static cross-polar channels (4 features)

These scalar parameters form an initial pool of sixteen features from which the best five are selected using the forward selection procedure. The use of somewhat lengthier feature vector for the grass is dictated by the two factors: a) the grass is considered to be a hard scenario and b) a larger than usual training dataset is available for the training.

The parameters for the PLSM-based processing are computed using the data obtained at the northern spot (see Appendix B.3 for the details on the measurement site and set-up). The presence of the butterfly mines makes the selection of the reference wavelet more difficult. I select the reference wavelet as a mean of the signals measured over five well-visible mines one of which is of a butterfly type. Definition of the parameters of the penalty functional is made maximizing functional (3.12), which in this particular case lead to the following values: $m_0 = 2$, $m_1 = 2.5$. The a-posteriori ROC curves obtained for the northern and middle (training) spots of the grass lane are shown in the Figure 5.5

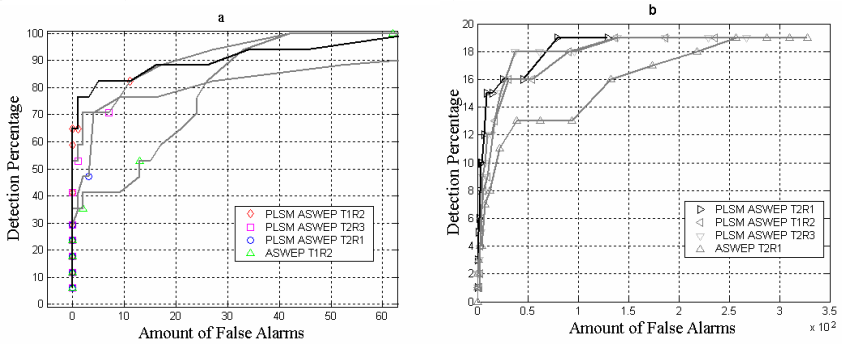

Figure 5.5 ROC curves for various individual features on the Grass lane; a) northern section of the lane; b) middle section of the lane.

The middle lane contains mostly the smaller APM placed at different depths. As it is seen from the Figure 5.5 b) the detection of the smaller (M14 and NR22)

mines in this environment can be a very difficult task. The level of false alarms is way too high and because of that the quality of the detection is judged at the 75% level rather than on the 90% and 100% levels. The forward selection procedure for this case is a time consuming one. It results in the following selection:

1. ASWEP values of the PLSM-processed T2R1 data
2. 3D ASWEP values combined with the burial depth for the T2R1 data
3. 3D ASWEP values combined with the burial depth for the T2R3 data
4. ASWEP values of the PLSM-processed T1R2 data
5. 3D ASWEP values combined with the burial depth for the T1R4 data

As always the features were pseudo-normalized in order to ensure the best possible performance of fusion algorithms. However, in this case the process of simultaneous pseudo-normalization of features did not always succeed (the possibility of this is discussed in Chapter 2.3.3). If an attempt to apply the simultaneous pseudo-normalization technique (2.51)-(2.55) was unsuccessful only clutter was pseudo-normalized and MD based quadratic detector was used rather than the ML based. In order to take into account generally weak performance of the radar at the middle spot, the covariance matrixes were obtained as weighed sum of the covariances independently obtained for the northern and the middle spot. A reducing .25 weight was used for the covariances computed at the middle spot to diminish (but not totally exclude) its influence. It has turned out in the end that the best possible combination of the features allowed simultaneous pseudo-normalization of all parameters and thus the ML based classifier (2.53) was built.

Application of the classifier to the blind test data is shown in the Figure 5.6.

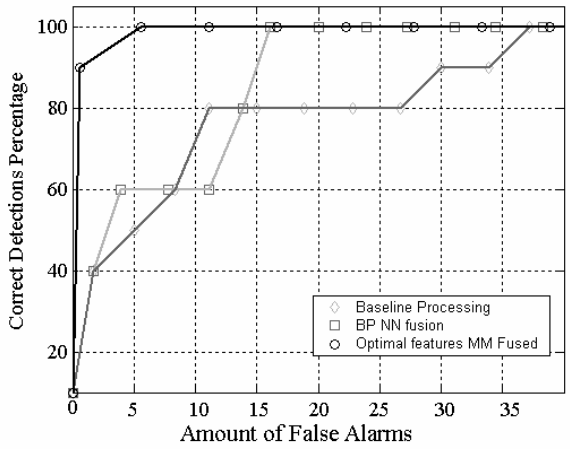

Figure 5.6 The a-posteriori ROC curves from the test lane in grass; baseline processing – best feature, baseline processing Nearest Neighbor fusion; best features according to the forward selection scheme pre-normalized, MM fusion.

Application of this resulting classifier to the training datasets showed that the fused detection indeed provides the better separation of the target/clutter classes. The detectability of the smaller mines is, however, lower than desirable. Nonetheless, the application of the classifier to the blind test data resulted in quite promising results, as it is shown in the Figure 5.6.

As it can be seen from the a-posteriori ROC curve, the false alarm rate at the 100% level of detection is diminished 3 times at the 100% level of detection and almost 30 times at the 90% level of detection in comparison to the base-line processed data fused by the nearest neighbor method. The results reported in the figure surpass those published in [51]. It should be noted, however, that the performance of the detector described by a-posteriori ROC curve strongly depends on the amount of false alarms and targets of different type placed into the ground.

5.2 Application to the data from MC'04

The measurement campaign of the autumn of 2004 (see Appendix C for the technical description) was held at a site located under tent primarily in order to test the new algorithms of the clutter suppression. The site is sandy and emulated a mine-field organized in a rough-surfaced dry sandy terrain contaminated with stones, shells, wood, plastic, and, other objects including the metal ones. The sandy soil does not pose a difficulty in the detection of all mines. On the other hand keeping the amount of false alarm reasonably low is very difficult under the conditions given.

As it is described in the Appendix, the same terrain has been measured three times. First, no targets were inserted and then the terrain was twice populated with the same set of dummy mines of PMN2 and M14 types and friendly objects. Although the targets and false alarm generating objects are virtually the same, they are placed at different positions (including depth). Besides, the random roughness of the surface was changed before every measurement. This setup allowed emulation of the very positive scenario in which a researcher has an access to the training data acquired at the conditions very similar (if not identical) to those which characterize the training site. The second scenario considered supposes that no training data is available from the test site. In this case all the training data would come from the previous measurement campaign (MC'02, [77], Appendix 5.1.1). The results for the both scenarios are described in this subsection.

In the first case (Scenario 1 used as a training set for the Scenario 2 and vice-versa) the pool of the initial features available for a researcher coincides with the one described in Chapter 5.1.1 (campaign of 2002, dry sandy lane):

1. Geometrical moment of the [0, 0] order for the WEP-based maps are combined with the burial depths into the model parameter (4.35) for the base-line processed data. This results in 6 scalar parameters describing energy characteristics of detected objects.

2. Geometrical moments of the [0, 0] order for the 3D-ASWEP-based maps are computed for the PLSM-processed data from co-polar channels. This results in 4 scalar parameters relying mostly on the waveform of object responses

Just like in that case here the conditions of the training site almost exactly (neglecting the surface roughness) coincide with those of the test site. Hence the training dataset provides a very good approximation for the reference wavelet and allows the use of fairly strict penalty functional in the PLSM-based clutter suppression. On the other hand, this time the dataset is large enough to build a well-performing maximum likelihood based quadratic detector. The penalty functional parameters for the PLSM processing (3.15) are selected via the procedure (3.10)-(3.12) to be equal to $m_0 = 1.5$ and $m_1 = 1$ for all four co-polar channels. As a result, the PLSM-SAR-3DASWEP sequence output combined with the SAR-WEP/Depth Model sequence output form the initial pool of 10 features. Examples of confidence maps provided by the features from the initial pool are shown in Figure 5.7 and Figure 5.8 for the scenarios 1 and 2 respectively. The target positions according to the ground truth are encircled.

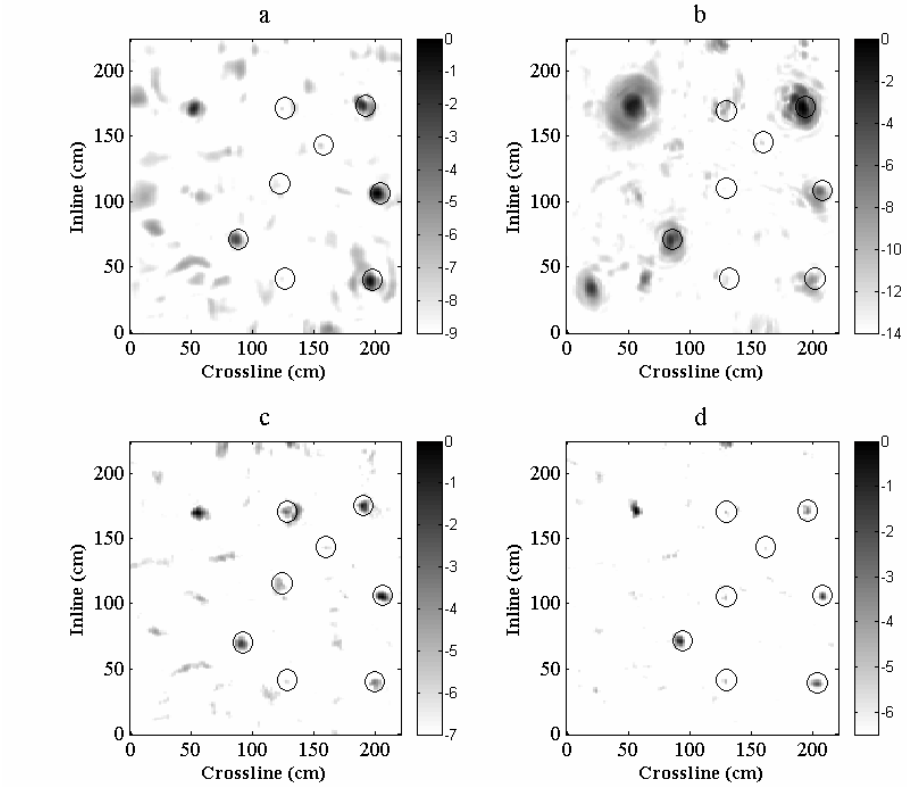

Figure 5.7 Confidence maps for the scenario – 1: a) T1R2, b) T2R4 (both via the scheme A), c) T2R1 and d) T1R4 (both via the scheme B)

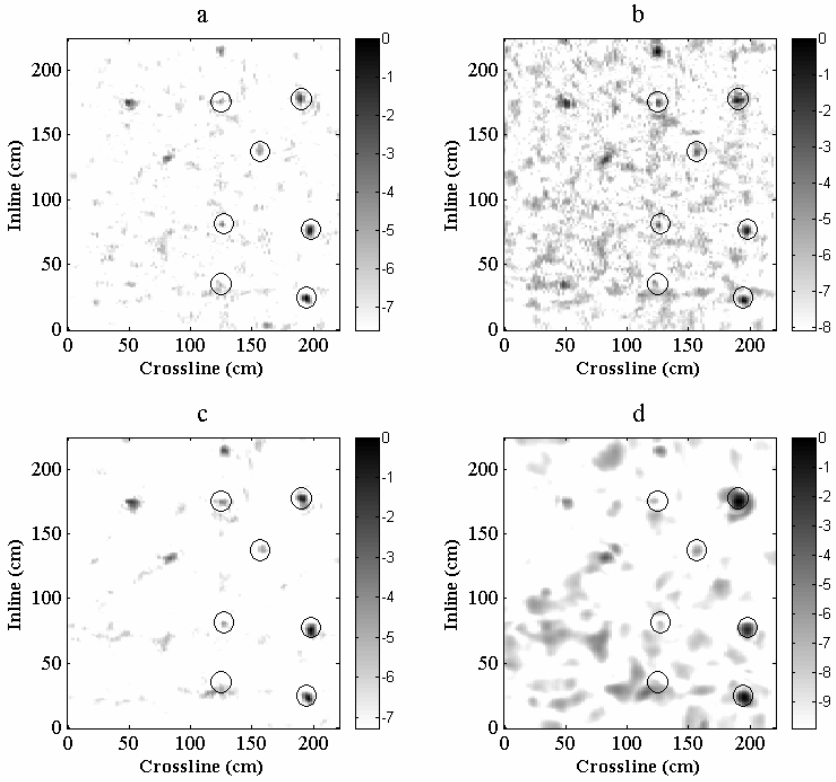

Figure 5.8 Confidence maps for the scenario – 2: a) T1R2, b) T2R1, c) T1R4 (all three from the scheme B) and d) T2R3, scheme A

As it could be expected from the set-up the PLSM-processed co-polar mono-static channels provide seemingly better confidence maps. On the other hand, the results obtained from the data processing scheme A may provide information not available at the output of the data processing scheme B. The forward selection procedure is applied to define the optimal set of three features that will be used for the clutter/target dichotomy.

The forward feature selection process ultimately results in the three best features, as it is illustrated in Figure 5.9 for both scenarios. It can be seen from the subfigures a) and b), that the output of the T2R1 radar channel processed with the scheme B is the best feature for the ground-truth – 1, while the T1R4 output processed with the scheme B is the best single feature for the ground-truth – 2.

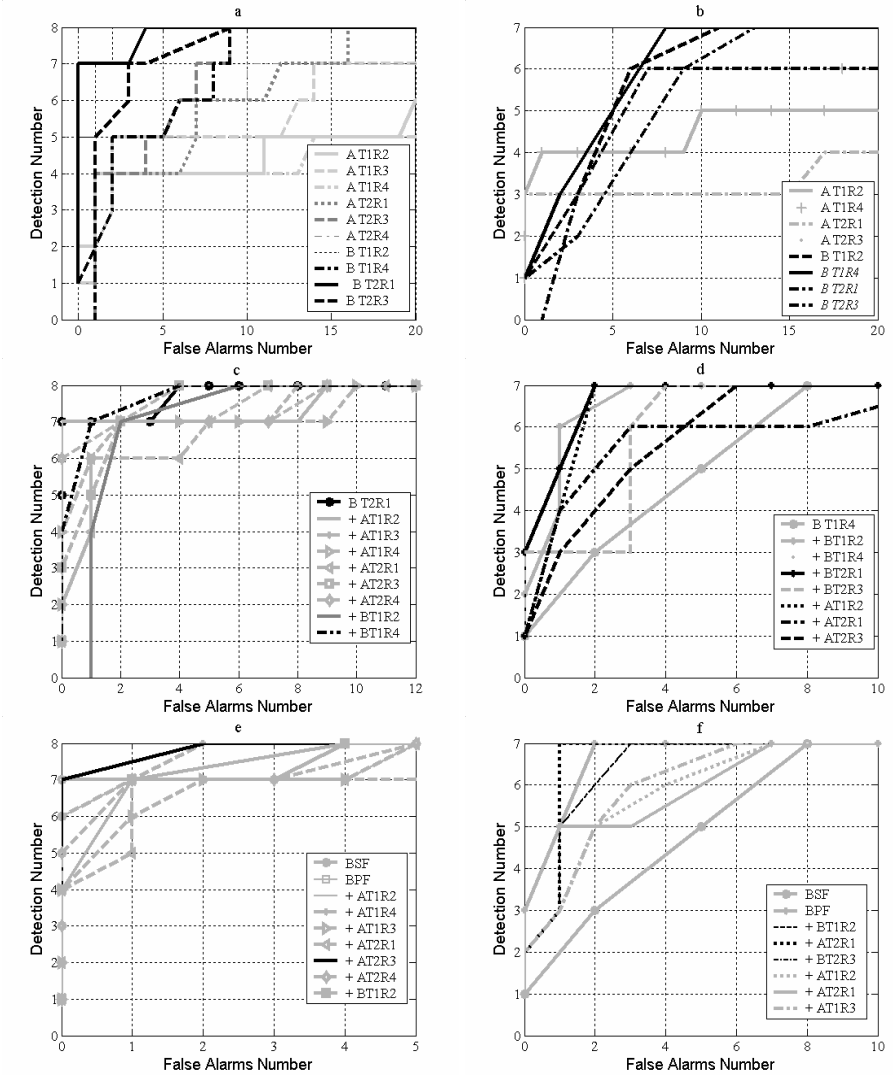

Figure 5.9 The forward feature selection process at the sandpit illustrated with a-posteriori ROC curves: a) single features, scenario – 1, b) single features, scenario – 2, c) pairs of features, scenario – 1, d) pairs of features, scenario – 2, e) triples of features, scenario – 1, f) triples of features, scenario – 2; the ROC curves corresponding to the best single features (BSF) and the best pair of features are also shown in the subfigures e) and f)

The analysis of the ROC curves corresponding to various pairings of the features with the best single feature results in the addition of the T1R4 output processed with the scheme B as the best pairing for the ground truth – 1 and the T2R1 radar channel processed with the scheme B for the ground truth – 2 (subfigures c

and d). Therefore, both ground truth have the same optimal vector of predictors of the length 2. Analyzing all possible triples of features via the ROC curves one obtains that the optimal decisive vector for the ground-truth – 1 consists of the BT2R1, BT1R4, and AT2R3 features, while for the ground-truth – 2 it consists of BT2R1, BT1R4, and AT2R1 features (subfigures e and f).

As it can be seen from the Figure 5.9 the non-blind separation of the target and clutter classes is significantly improved with the introduction of extra features. Namely, the 100% level of detection on the basis of the best single feature results in 5 and 8 false alarms for the ground-truths 1 and 2 respectively. Introduction of the best second feature lowers the amount of false alarm to the 4 and 2 respectively. The best triples of feature provide even better separation with only 2 false alarms in each case. Further separation might be possible with the addition of the extra feature but is not practical because it leads to the overtraining of the algorithm. More precisely, the separation of the classes at the training site can be further improved but the volatility of covariance of higher dimensional feature vectors prevents their successful use as plug-in rules.

The application of the quadratic classifiers resulted from the training and forward selection of the decisive features to the blind test sites produced the results shown in Figure 5.10.

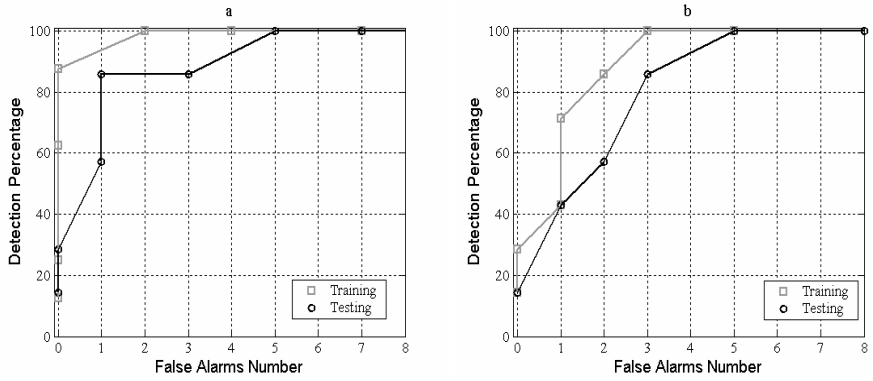

Figure 5.10 Performance of the system on the blind tests; a) trained with groundtruth – 1, tested at groundtruth – 2, b) vice versa. The pale ROC curves demonstrate the corresponding training results

As it can be seen from the figure, 5 false alarms are reported in both cases at the 100% level of detection. The 100% level of detection was obtained with the base-line processing with 14 and 16 false alarms respectively (Figure 5.9 a and b). Thus in this particular case the FAR is reduced about 3 times.

In the second set up Scenarios 1 and 2 are used as test sites and the training is made at the sandy lane (Appendix B.1). The training according to this scenario has been made and described in subchapter 5.1.1. There it was found that PLSM

processed data from the channels T1R2, T2R1, and T2R3 combine the best possible triple of features. I build a quadratic classifier on the base of the data measured during the measurement campaign at the Waalsdorp facilities in 2002. The parameters for the PLSM processing and S_L-normalization are also learned from these data. The application of this classifier to thee data acquired during the MC'04 in the sandbox results in the a-posteriori ROC curves shown in Figure 5.11.

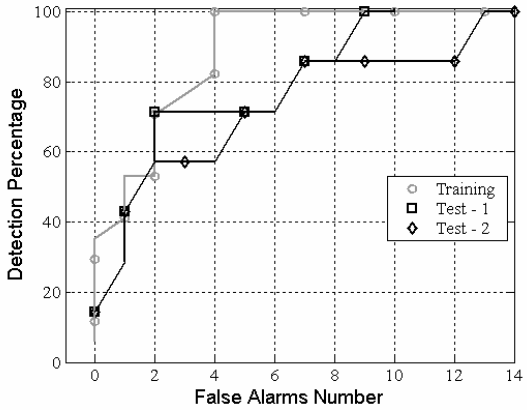

Figure 5.11 Application of ML-based quadratic classifier trained on the data from measurement campaign of 2002 to the data acquired during the measurement campaign 2004

As it can be seen from the figure, the maximum likelihood based quadratic classifier trained on the data acquired at different site produces 9 and 13 false alarms on the 100% level of detection. This false alarm rate is higher than the one achieved with the best single feature (wave-form based clutter suppression based mono-static channels). This confirms the conclusion of subchapter 5.1.1 that training on the site very similar to the test one is nearly necessary for the successful use of plug-in rules based feature fusion. At the same time the obtained results lower the false alarm rate resulted from the base-line processing.

5.3 Conclusion for Chapter 5

The practical applications of the data processing algorithms suggested in the thesis demonstrated the following main results:

- The wave-form based clutter suppression provides very strong clutter suppression in the dry soil conditions. Namely, the single feature based detection resulted in 2 times reduction of FAR for the data from MC of 2002 and 3 times reduction of FAR for the data from MC 04.

The more profound FAR reduction achieved in the latter campaign is explained by the much rougher surface in its site. The surface roughness heavily influences the baseline processing, while PLSM based algorithms are almost immune to it

- The forward selection feature selection technique allows objective evaluation of the amount of discrimination each particular feature provides
- After pseudo-normalization the quadratic classifiers based on both ML and MD criteria provide stable results
- Unlike the nearest neighbor based technique, considered classifiers provide predictable results when used as plug-in rules at testing sites
- The algorithms suggested in the thesis provided fused feature detection results, which are better than those previously published (for the test sites in which the external results exist). More precisely, the 100% detection was achieved for the sandy lane of the Waalsdorp facilities with 6 false alarms.

Chapter 6 Conclusions and Recommendations

The goal of the present study was set to suggest a set of the clutter suppression and target detection algorithms that would provide 99.6% detection of the APM using polarimetric GPR while significantly decreasing the false alarm rate corresponding to it. The success of the suggested algorithms is measured against the results published for the same terrains and achieved by other means (where such publications exist) and against the baseline detection procedure.

The state-of-the-art technology available at the moment of finalization of this thesis although quite advanced leaves unanswered several key questions. First, an automated process of data transformation is needed. In this process the data coming from different sources must be automatically transformed in such a way that target features representing features can be extracted from them. Second, currently the feature fusion algorithms do not fully exploit the possibilities provided by quadratic classifiers because these classifiers operate suboptimally if the feature normality condition is not imposed. Third, the false alarm rate remains high mostly due to the lack of clutter suppression algorithms operating from a target model approach. At the current state the clutter suppression algorithms operate from a background model and even if successful they do not provide suppression of clutter coming from friendly objects. Fourth, the optimality of the feature retrieval and determination of the optimal features are not always objectively justified. Hence objective data-driven schemes for these processes needed to be developed.

In order to achieve the goals for this study the following results were accomplished. In Chapter 2 I have suggested a new automated statistical approach to the data processing and interpretation. The approach presents independent processing of multiple data flows, construction of confidence maps, and initial detection in them. The algorithm of maps reconciliation and detection association has been suggested. The target/clutter dichotomy is then reduced to binary hypothesis testing, which is solved by statistical inference techniques. In order to improve the performance of quadratic classifiers I have suggested an adaptation of Johnson's data normalization techniques for the case of APM detection with GPR. Two techniques of clutter or simultaneous target and clutter normalization have been adapted for the cases representing different training set scenarios.

In Chapter 3 I have presented a novel generic waveform-based algorithm for clutter suppression, which drastically improves detectability of a certain class of targets (i.e. antipersonnel landmines) with video impulse ground penetrating radar. The algorithm (penalized local similarity measure) is demonstrated to possess the following features:

- It detects a class of low-metal APM with a cylindrical shape (such as PMN2, M14, and NR22) using just a single reference target return;

- The processor aims at suppression of the clutter responses from non-targets and leaves intact the spatial patterns inherent to localized objects;
- As a result it operates best when the background clutter is removed *prior* to it and spatial pattern of targets is detected *after* its use;
- The output of the processor is perfectly suited to be an input to a SAR focusing procedure due to its sharp bi-polar shape;
- The output of the processor does not directly depend on the magnitude of the input providing equalization of the responses from mines of different sizes;
- The core processor of the algorithm is insensitive to the presence of clutter objects regardless of their size and/or reflectivity provided that their signatures wavelets are different from the one of the reference wavelet;

The core algorithm is then superimposed with the SAR procedure. This superposition allows introduction of the angle-dependent reference wavelet.

In Chapter 4 I have presented the techniques of forming and selecting the decisive features for the target/clutter dichotomy. The scope of the chapter includes descriptions of the originally developed WEP/ASWEP projection techniques, which allow construction of the better confidence maps than those of the conventional energy projections and on top of that provide means for the determination of the targets burial depth. The use of the depth of the object as a feature auxiliary to its brightness has been also suggested. Besides, other statistically bound auxiliary features have been presented. Finally, the forward feature selection procedure has been adapted for the mine detection using GPR as means for objective selection of the best features.

In Chapter 5 I have presented the results of application of the methods and algorithms developed in the thesis to the data acquired during two measurements campaigns. The following scheme of the semi-automated mine detection has been developed and adopted:

1. The data are acquired over the interrogated terrain and the corresponding training site using several radar scenarios
2. The data acquired over the training site are processed independently for each of the scenarios. The processing includes:
    a. Data evaluation and pre-processing (see Appendix A.2 for details);
    b. Background removal;
    c. Training and application of waveform based clutter suppression/target detection algorithm;
    d. SAR focusing of the data resulted from the steps 2.b and 2.c;
    e. Training and application of the EP/WEP/ASWEP projection techniques, which results in several detection maps;

   f. Initial detection via local maxima detector and determination of auxiliary features in each of the maps.
3. An initial feature pool is formed from the most promising of the features resulted from the step 2. An expert assessment is required at this stage to select 10-30 of the better features from several hundreds available in principle.
4. The maps corresponding to the pre-selected features are reconciled
5. The forward selection procedure is applied to the pre-selected features, which results in the selection of the optimal feature vector.
6. The selected features are pre-normalized and the feature vector is whitened.
7. The optimal in the sense of generalized maximum likelihood or deflection linear-quadratic fusion rule is built.
8. The data acquired over the interrogated terrain are processed.
9. The list of initial detections is built using local maxima detector and the feature vector corresponding to the one found on the step 4 is built to each of the detection.
10. Linear-quadratic fusion rule built on the step 7 is applied to the list resulting in the final detection of the present targets.

The results of the testing of the above framework on the measured data showed that:

- The waveform based clutter suppression algorithm allows the suppression of false alarms rate in 2.5-3 times for the case of 100% detection in sandy lane in comparison to the base-line processing techniques
- The same algorithm reduces the false alarm rate at the 100% mines detection level 5-6 times in the rough surface sandy conditions
- Although not thoroughly tested against the false alarm generating objects, this technique showed 3 times FAR reduction in the grass site
- Introduction of the feature pseudo-normalization as a preliminary step in feature fusion allowed for successful use of quadratic classifiers based on maximum likelihood or maximum deflection criteria
- An improved stability of the data fusion approach in comparison to the previously published learning vector quantification has been shown. I.e. 100% detection has been achieved at all blind test sites with false alarms rate 50% lower than those reported in previous publications

At the same time the following research directions are left for the future. The main tool used for the feature fusion in the present thesis is a linear-quadratic classifier. Although more robust when used as a plug-in rule these classifiers require

that the feature vectors are multi-normally distributed for both (or with some reservations at least one of the) classes of clutter and target. As it is never the case at least for the brightness-bound features a process of normalization must be applied to them. It was not possible however to ensure a multi-normality of the features and only the quasi-normality of the marginals (i.e. the scalar features) is guaranteed. This does not imply that feature vector becomes multi-normally distributed, for which a normality of *any* linear combination of marginals is a criterion. In this thesis it is suggested that a simultaneous diagonalization transformation is applied to the classes of target and clutter *after* normalization of the marginals and the latter are again tested for the 4^{th} order normality. If the normality of the marginals is retained through the diagonalization transformation the feature vector can be treated as multi-normally distributed. There are two open problems in this approach: firstly, this is not a rigorous proof of the normality; secondly, if the non-normality of one or more marginals in the diagonalized distributions is detected there is no known way to resolve this. It is only possible to exclude the non-normal feature and repeat the process of diagonalization.

The waveform based clutter suppression proved to be a very significant achievement in the reduction of the false alarm rate. However the question of the applicability of the technique to soils other than various types of sand should be addressed. This question is not fully investigated in the present thesis due to the lack of the corresponding data. It is shown that the waveform based clutter suppression in the form of Gaussian PLSM can tolerate certain instabilities in the soil parameters and target type but more in-depth investigation of the issue with the data at hand would be of interest. The second open question related to the issue is expansion of the technique to the case where two distinctively different waveforms are sought for simultaneously.

The functional dependence between the WEP-brightness of a target and the depth of its burial is successfully exploited in this thesis (especially in chapter 5.1.3). However the decisive feature resulting from the established dependence could have been more productive is a sufficient amount of training data reflecting different targets placed at different burial depths were exploited. This needed improvement is left for the future work.

As it seen from the Chapter 5, a full-polarimetric GPR can provide vast amount of features for target detection. Features resulting from other sensors that could be present in the system will add to that amount. Overall, an initial pool of more than 500 features can be expected. Application of extensive search for the best possible feature vector of the length 4 to 8 is computationally prohibitive. If automated the forward selection procedure described in the Chapter 4 of the present thesis can be applied to all available initial features. In order to automate this procedure every ROC curve must be characterized with a single scalar number parameter. For example, minimal number of false alarms for a given level of detection or an area above the curve could be candidates for such a parameter. Identification of the best parameter is an open issue, which requires a separate research.

Overall, the insufficient amount of the training data prevents from using extensive feature vectors, which could be desirable in difficult scenarios. This can only be overcome by exhaustive measurement campaigns. In this thesis the features to be used for the target detection are chosen via the forward selection procedure. This procedure results in a feature set providing the best separation for the training site and it has been noticed that the best sets are not always comprised by the features providing the best one-feature detection. The amount of information each particular feature adds to the already existing pool cannot be judged from the forward feature selection process. Therefore the application of the information theory to this aspect of landmine detection with GPR can be of interest for the future research.

Appendix A IRCTR GPR

As the requirements for a GPR system dedicated to landmine detection are substantially different from the ones for a conventional GPR [3] the specific radar had been developed in IRCTR [29]. Among most important specific requirements are the substantial antenna elevation above the ground, high down-range and cross-range resolution, and finally high accuracy of the measured data to support target's identification. In this appendix I describe the principles of the hardware design and software support of the radar that was used to acquire all the data present in this thesis.

A.1 Design considerations

The three main parameters of a radar design are frequency band, the antenna configuration and the sampling rate. The frequency band has to be adequate to the task of detecting antipersonnel mines inside and/or above of a soil. Landmine detection requires down-range resolution of the order of several centimeters (a few times smaller than a typical size of an antipersonnel mine) in the ground, which can be achieved using a bandwidth up to 3 GHz. The optimal allocation of this band can be found uniquely. As it was shown in [103] the ideal GPR should use all frequencies from DC till some upper frequency, which is determined by a required down-range resolution. Since practically very low frequencies are not accessible due to a limited size of antenna system and at frequencies above 4 GHz the propagation loss and clutter (caused by air–ground interface roughness and inhomogeneity of the soil surface) limit the applicability of GPR systems considerably [4]. The video impulse radar developed at IRCTR has 2 orthogonal polarized transmit antennas and 4 receiver antennas connected to the independent channels correspondingly. In the Figure 2 Tx_i are the transmitters, Rx_i are the receivers, X and Y are the axes direction, the antennas polarizations are denoted with arrows. Thus there are 4 co-polar and 4 cross polar receiving channels.

The identical dielectric wedge antennas are used as transmitters, identical loops are used as the receivers. The receive antennas are placed directly underneath the transmitters in order to narrow the footprint of the antenna system and thus to enchanse its spatial resolution. One of the consequences of the design is that the direct wave is the largest signal in the system, which defines the upper limit of the system's dynamic range.

Tx/Rx	Rx1	Rx2	Rx3	Rx4
Tx1	34.8	9.9	10	45.8
Tx2	10	31.1	45.2	9.9

Table A.1 Distances between the antennas in horizontal plane, cm.

The radar has 4 quasi-monostatic transmitter-receiver pairs (T1R2 and T2R1 co-polar; T1R3 and T2R4 cross-polar) and 4 significantly bi-stactic ones (T1R1 and T2R2 co-polar; T1R4 and T2R3 cross-polar). The distances in X-Y plane between the antennas are presented in the Table 1. The heights of the receiving loops over the surfaces were chosen to be 20 cm over the sand and 10 cm over the grass. The distance between the receiver loop and the aperture of the transmit antennas is 28 cm.

The high quality of the hardware and the high stacking number provide a sub sample stability of the firing times of the generator. Figure A.1 presents the overlapped plot of 36735 A-Scans, which compound one of the measured C-Scans.

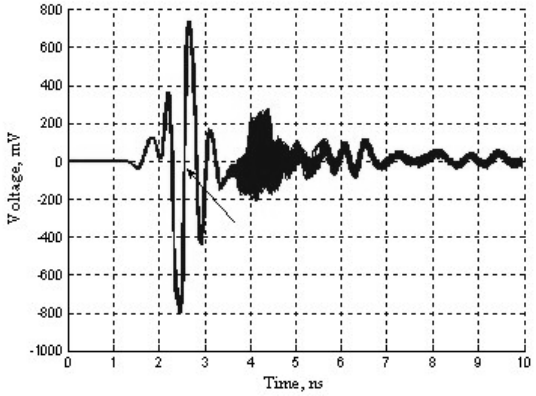

Figure A.1 A-Scans compounding a typical C-Scan overlapped; the arrow marks the main zero-crossing used for evaluation of the stability

The moments of the zero crossing T_0, depicted by the arrow in the figure are shown at the Figure A.2

Vertical lines on the Figure A.2 represent end points of the B-Scans acquired during the actual measurements. The mean jumps of the T_0 are placed in the close vicinities of the lines and most probably are due to the mechanical vibrations of the system in the ends and beginning of the movements. The other possible reason of these minor jumps is 1 sec breaks of the system operation which happen in between B-Scans. The jitter of the system has been determined equal to 6.47 ps on the entire C-Scan and to 3.5 ps after the slow trend removal from the data. In both cases the jitter is well inside of one sample.

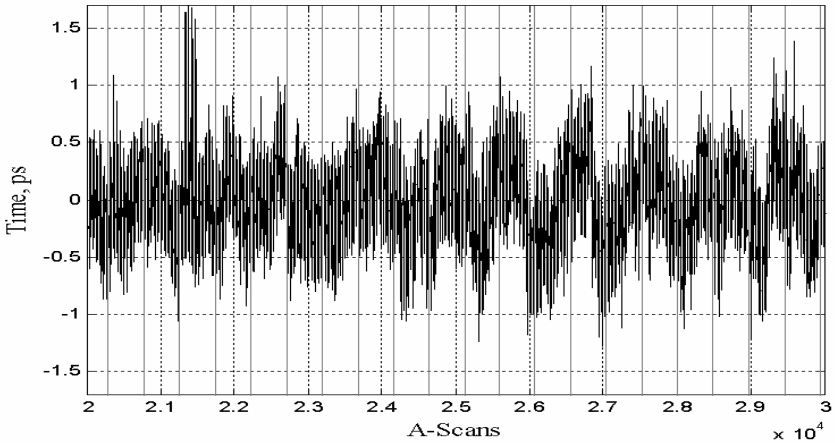

Figure A.2 Evolution of the main zero-crossing in the C-Scan plotted in Figure A.1; gray vertical lines in the figure correspond to ends of B-Scans

A.2 Data pre-processing

In this appendix I introduce a set of the data quality evaluation parameters and a data pre-processing chain (DPPC), which allows for stabilization of these parameters. I show the influence of this stabilization on both the quality of the Ground Bounce (GB) removal and in the final ROC curve. The data which I use to demonstrate the DPPC has been acquired during a measurement campaign held in the sand pit located in the TNO DS&S lab in The Hague, The Netherlands in the end of 2004 [80], Appendix 1.1.

The short list the problems peculiar to the raw data taken from a video impulse GPR, which can affect the performance of the detector consists of:

- Noise on the frequencies outside of the operational band of the equipment
- Instability of the time-axis of the equipment
- Instability of the voltage-axis of the equipment
- Instability of the quantity of the A-Scans in B-Scans and misalignment of the adjacent B-Scans

Further I discuss the techniques that allow easing these problems and showing the improvement of the data. The time domain pass-band filtering is used for noise suppression outside of the operational band of the Radar; the instabilities of the time axis of the radar is compensated by an appropriate sub-sample shifting of the A-Scans made in the frequency domain; the voltage axis instability is compensated by the normalization of the direct wave on the median value of the direct wave voltage for the C-Scan; the missing A-Scans are made up with linear interpolation

of the neighboring A-Scans and the misalignment of the adjacent B-Scans is compensated by an optimal sample-shifting of the B-Scans.

The DPPC used for the compensation of the instabilities, which are observed in the raw A-Scans is shown in Figure A.3

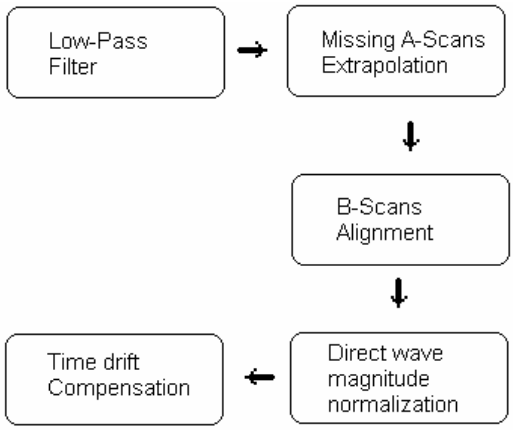

Figure A.3 Data Pre-processing scheme

As it can be seen from the Figure, we start with suppressing of the noise on the frequencies outside of the operational band of the GPR. Since the operational band of our GPR is limited to 3.3 GHz [29] and the sampling rate used here defines the Nyquist frequency of 25.6 GHz it is obvious that most of the frequency band of each A-Scan does not contain any valuable information. A low-pass filtering of each A-Scan is therefore appropriate as a first step of the pre-processing.

As the fastest voltage slope observed in the data is approximately 220mV in .08 ns the shape of the pulse should not be affected if we apply low-pass filter to the A-Scans suppressing the energy in the frequencies above ~4GHz. Taking into account the realization of the of the 10th order Butterworth filter we are going to use, it is safe to choose the cut-off frequency equal to 6.5 GHz.

When the high frequency noise is suppressed it is easier to develop a procedure of the stabilization of the radar axes. The instability of the voltage axis of the radar is probably caused by transitional processes in amplifying circuits of the radar generator as well as mechanical vibrations of the receive antennas. And the instability of the time axis of the radar is mainly due to the non-equal time delays between the firings of the generator of the radar amplified by a tendency of the generator of this particular radar for the slow trend towards the earlier times. Although the time-axis instabilities of the first kind are normally of sub-sample nature, aggravated by the voltage axis instabilities they may significantly worsen the performance of the GB removal procedure and to lesser extent the performance of

the SAR focusing. Thus it is very important to diminish their influence at least for the times corresponding to the direct wave and ground bounce.

The following statistical processes are used for the evaluation of the stability of the axes:

The value of the main minimum of the direct wave of the GPR taken in each A-Scan of a C-Scan is used to characterize the stability of the voltage axis of the GPR

The exact time of the main zero crossing of the direct wave is used to characterize the stability of the time axis of the GPR

While the waveform of the IRCTR GPR is quite stable [29], the magnitude of the radiated pulse exhibits a minor instability. The range of this instability is typically within 1% and its variance is about of 0.2% of the peak to peak magnitude. Due to the placement of the receive antenna directly underneath of the transmit one the received wave in all co-polar configurations has a maximum of the absolute value corresponding to the direct wave [30]. Thus, the magnitude instability can be compensated by normalization of all A-Scans to the mean value of the main minimum of the direct wave:

$$\tilde{u}_i(t) = \frac{\overline{A}}{\min_t[u_i(t)]} u_i(t) \tag{A.1}$$

where $\overline{A}$ is the mean value of the main minima of the direct wave and $u_i(t)$ is a raw A-Scan. In our case this is equivalent to the normalization on the maximum of the absolute value of the direct wave. Slightly more complicated phenomena have been observed in the cross-polar channels of the radar, where specific structure of an air/ground interface or large elongated objects may cause a reflection of a magnitude higher than the one of the direct wave. Therefore for the successful use in the cross-polar channels the global minimum in (A.1) must be replaced with the one restricted for $t < T_s$, where T_s is a time corresponding to the return of the surface reflection.

The time axis of the equipment is, again, quite stable in comparison to a conventional GPR: the time drift of the direct wave is typically in a sub-sample range for the whole C-Scan [31]. However even sub-sample instability of the time axis may result in deterioration of the performance of GB removal techniques based on any kind of mean value elimination. Therefore, drift of the equipment is compensated by sub-sample shift of all A-Scans to the median value of the main zero crossing. This operation is performed in the frequency domain according to

$$\tilde{U}_i(f) = \exp\{jf(\tau_i - \overline{\tau})\} U_i(f) \tag{A.2}$$

where τ_i is the time of the zero-crossing in the i-th A-Scan, $\overline{\tau}$ is the mean value of this parameter in the C-Scan, $U_i(f)$ and $\tilde{U}_i(f)$ are spectra of a raw and preprocessed A-Scans.

The overlapped A-Scans which compound a C-Scan before and after the compensation of these instabilities preceded by the low-pass filtering are shown in Figure A.4 below. As it can be seen from the figure, the time drift is successfully compensated not only for the exact point in time for which the statistic is gathered but also for the whole range of the main energy lobes of the direct wave.

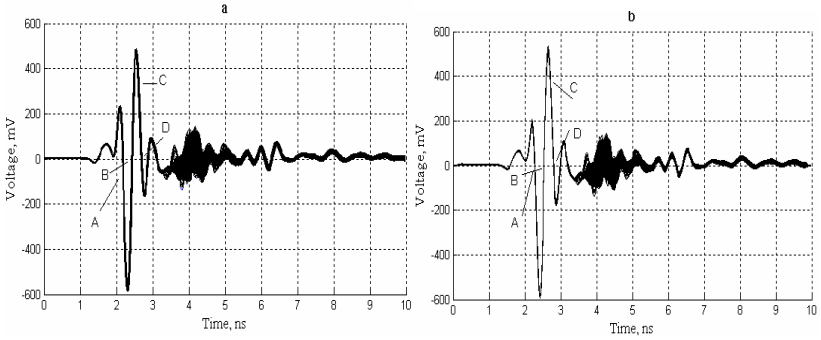

Figure A.4 Overlapped A-Scans, which compound the raw (a) and the preprocessed C-Scan.

Numerically, the achieved improvement can be illustrated by the analysis of the statistics of the time drift for several points taken in the time span of the direct wave. To illustrate this point I take four points on the time axis marked as A, B, C, and D in Figure A.4 and build a statistic processes of the time drift peculiar to these points. By the time drift here I mean the times in which the voltage crosses the zero line for points A, B, and D and the 400 mV line for the point C. The trend (range) and the jitter (standard deviation) are given in the Table A.2.

The Table clearly demonstrates a significant diminishing of both parameters not only for the point B, for which the procedure of stabilization has been provided but also for 3 other points.

Time point,ns		**A** 2.19	**B** 2.44	**C** 2.6	**D** 2.7
Trend, Jitter, ps					
Raw	**T, ps**	**35.4**	**151**	**116**	**40.**
	J, ps	**2.6**	**3.6**	**1.9**	**2.3**
PP	**T, ps**	**2.9**	**0.1**	**1.5**	**3.7**
	J, ps	**1.2**	**0.01**	**0.6**	**1.5**

Table A.2 Trend (T) and Jitter (J) of the points on the Direct Wave

This improvement plays an important role at the stage of the ground bounce removal. The influence of this stage of the equipment drift compensation is illustrated in Figure A.5. The figure shows the early portions of overlapped A-Scans, which form the raw (a) and preprocessed (b) C-Scans. The GB has been removed

from these A-Scans by cylindrical moving window average eliminator ([23], MWAE, subchapter 1.2.1).

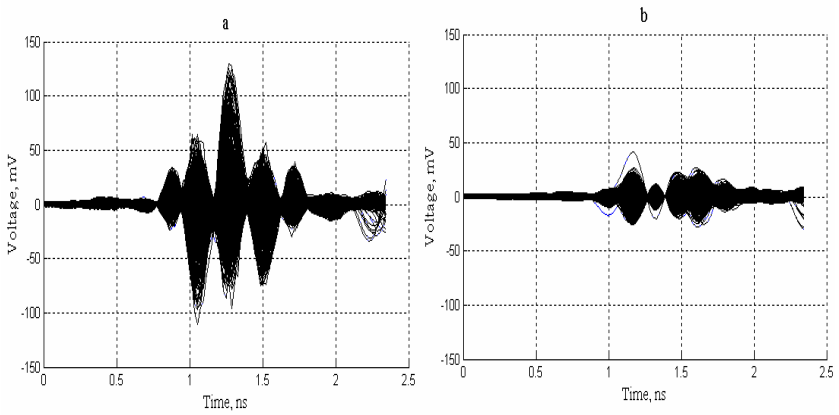

Figure A.5 Early time portions of A-Scans compounding the Raw a) and Pre-processed b) C-Scans after the GB elimination

Quantitatively speaking the mean energy of the direct wave remnant is 6 dB lower in the pre-processed C-Scan in comparison to the raw one. This improvement is due to the fact that when the direct waves of the A-Scans inside the chosen window are unstable even on a sub-sample level, the MWAE operator performs a numerical derivation and since the speed of voltage change there is quite high, high values of the remnant arise.

Another type of the problems, which may occur in the raw C-Scans, is missing A-Scan: it can happen that certain B-Scans, which compound the C-Scan, have lower than average number of A-Scans. In this case the missing A-Scans are constructed by a linear interpolation with the use of the A-Scans of the adjacent B-Scans. It does not significantly worsen the SAR imaging performance and it should not since it is usually necessary to made up only a few out of typically 50000 A-Scans. However, the mines (as well as any small objects) appear in the time slices of raw C-Scans as ellipses [101]. The absence of a few A-Scans in one or several of the B-Scans typically leads to the disfiguring of these elliptical images. The example of such disfiguring is shown in Figure A.6.-a) below. In the C-Scan illustrated by the time-slice in the figure several A-Scans have been missed by the equipment during the acquisition of the B-Scan # 40 (the B-Scans are enumerated in the figure in order opposite to which they have been collected) and the elliptical images of the objects placed to the left from it are disfigured. This instability is compensated by relevant re-shifting of the B-Scans made on a whole-sample level. The smoothness of these ellipses in Figure A.6 b) can be used to asses the quality of the mutual re-alignment of the B-Scans.

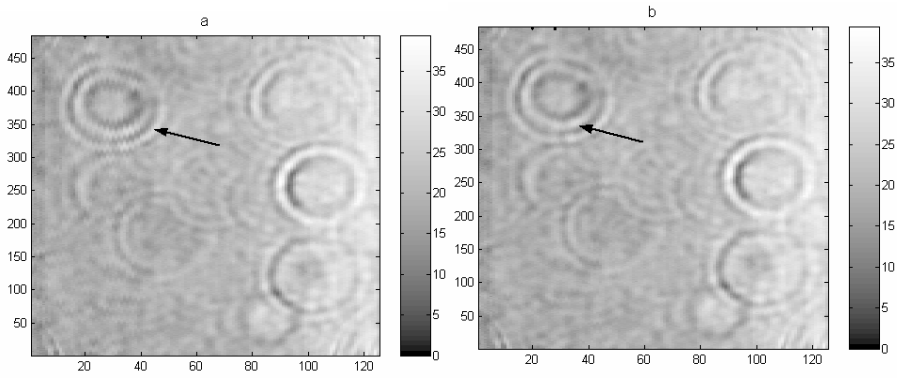

Figure A.6 Time slices of the raw a) and re-aligned b) C-Scans. The distorted elliptical image of the mine is depicted with arrow

To illustrate the influence which a proper DPPC may have I apply the following realization of a baseline data processing scheme (see the discussion in chapter 2.1) to the data shown in Figure A.6 with and without preprocessing:

$$\begin{aligned} &GB\,removal \rightarrow SAR \rightarrow \\ &\quad \rightarrow Energy\ Projection \rightarrow \\ &\rightarrow Automated\ Detection \\ &\rightarrow ROC\ curve \end{aligned} \tag{A.3}$$

The baseline processing is chosen intentionally over more sophisticated techniques to demonstrate the merits of the pre-processing. As it can be seen from Receiver Operations Characteristics curves shown in Figure A.7, the introduction of the DPPC alone improves the performance of the system

Therefore it can be said that a data pre-processing scheme, which allows compensation of instabilities of the time- and voltage- axis of a video-impulse GPR, is a necessary step in mine detection with GPR. The improvement in the statistical characteristics of main extremum and time of the main zero-crossing of the direct wave viewed as statistical processes is shown to cause the improvement in the background removal and as the matter of fact in the detection abilities of the system. The latter is shown by the improvement achieved in building of the ROC curve.

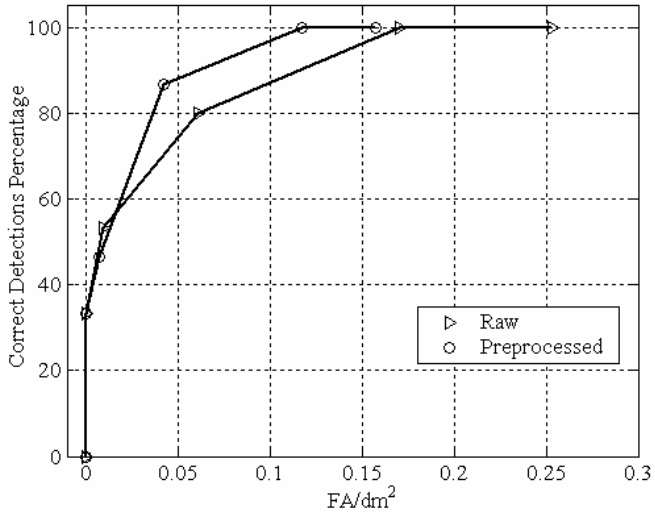

Figure A.7 The ROC curves for the raw and pre-processed C-Scans

Appendix B Measurement campaign of summer 2002

The Measurement Campaign of summer 2002 was held in cooperation with TNO DS&S Laboratory at the measurement facility 'Waalsdorp' in Den Haag [78]. The goal of the Campaign on the IRCTR side was testing of the performance of the GPR equipment developed in IRCTR in different soil conditions. The measurements have been executed at a time span from July 15 to July 25 of 2002.

The measurements were made in three different soil conditions and resulted in the extensive set of 72 C-Scans covering seven different (electrically or physically) sites. The minefield simulation sites were represented by a dry sandy lane, artificially moistured sandy lane, and grass. This Appendix describes the physical conditions at which these measurements were made and measurement sites and set ups.

B.1 Dry sandy lane

The radar was placed at the scanner system over the sandy lane to produce a 20 cm gap between the receive antennas and the surface of the lane. The electromagnetic permittivity of the ground is estimated to be $\varepsilon_r \cong 2.5$. The lane has dimensions of approximately 3 by 10 meters and the two spots on it have been covered. The lane contains mine simulants of PMN2, M14, NR22 types and various false alarm objects placed at depths of 0 to 6 cm. Also the TDR sensors are placed at depths 10 – 15 cm to monitor the ground conditions.

The sandy lane was covered in two separate radar sessions thus producing two overlapping spots. The 0.5 ns generator has been used in order to ensure better resolution of the system. The first spot on the sandy lane contains 6 specimens of PMN2 mine, 8 specimens of M14, and 4 specimens of NR22. The false alarms are generated by 6 intentionally buried objects of various types and more than 10 TDR sensors. These sensors reflect the probing waves strong enough to be an additional source of the false alarms. The objects placed in this spot are detailed in the Table B.1, part Sand-1.

The second spot on the sandy lane (Table B.1, part Sand – 2) contains only 2 PMN2 mines, 3 M14 and 3 NR22 mines placed close to the borders of the measured spot. The intentionally buried false alarm objects (5 specimens) and about 10 TDR sensors are spread evenly over the spot.

Measurement Spot	ε_r, estimated	Antenna height, cm	Present Mines (quantity)	Depth Range, cm	Present FA	Depth Range, cm
Sand 1	2.5	20	PMN2 (6) M14 (8) NR22(4)	0 - 6	Metal disk, metal ball, barbed wire, Stone (2), brick, TDR sensors (~12)	0 - 15
Sand 2	2.5	20	PMN2(6) M14 (8) NR22 (4)	1 - 6	Metal disk, metal ball, barbed wire, stone, brick, TDR sensors (~10)	5 - 15

Table B.1 Objects placed at the sandy lane

The material properties of the mine simulants and friendly objects placed at the lane can be found in Table B.2.

Object Type	Top size, cm	Height, cm	Case / Composition	Metal Content
APM PMN2	∅ 12	5.4	Plastic/TNT'	Pin
APM M14	∅ 5.8	4	Plastic/TNT'	Pin
APM NR22	∅ 5.2	5.5	Plastic/TNT'	No
APM PFM1	12*6.5"	2	Metal/TNT'	Large
Barbed Wire	30*0.4	∅.3	Metal	100%
Metal Disk	∅ 12	0.3	Metal	100%
Metal Ball	∅ 8	∅ 8	Metal	100%
Brick	15*7	4	Silicon	No
Stone	∅"~ 8	∅"~ 8	Stone	No
Wood	∅"~ 18	3	Wood	No
TDR sensors	various	various	Metal/Plastic	Large
Plastic cup	∅ 6	6	Plastic/Cotton	No

'– SIMULATED, "– IRREGULAR

Table B.2 Material parameters of the targets in the sandy lane

B.2 Wet sandy lane

In order to estimate the performance of the radar in the extremely wet conditions the sandy lane has been moistured by the artificial raising of the underground water as well as due to the repeated showers during that time. Frederich Roth has taken the sand probes for quantitative analysis of its properties and it has been shown by Goritty et. al [102] that the water content in the sand varied from 7% to 15%. The dielectric permittivity of the sand was estimated to vary in the limits of 6 to 11.

The 0.8 ns generator was used for the measurements in order to ensure the better penetration of the probing pulses into the dissipative soil. The rest of the experiment set up was unchanged in comparison to the dry sand case.

B.3 Grass lane

The grass lane has the same dimensions as the sandy lane, namely 3*10 meters. This lane has been covered in the three measurements spots, two of which were overlapping. These (namely the southern and the middle spots) are used for the training purposes and the groundtruth for them had been revealed. The northern spot is used for the blind testing and only the horizontal positions of the mines without specification of their depth and types are revealed.

The radar has been connected to the scanning platform in such a way that the receive antennas are 10 cm above the ground (see Figure B.1). The dielectric permittivity of the ground is estimated to be $\varepsilon_r \cong 5$. Both 0.5 ns and 0.8 ns generators were used to perform the measurements. This resulted in that each spot of the lane has been measured with 16 radar scenarios.

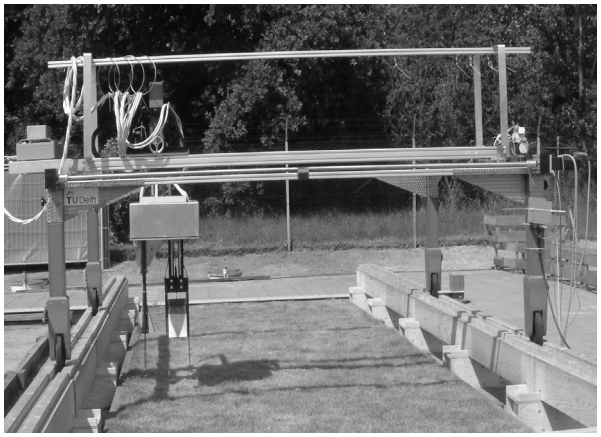

Figure B.1 Radar-Scanner construction over the grass lane

The mine simulants found in the grass lane are described in the Table B.3. As it can be seen from the table no false alarms except for the TDR sensors are placed into the grass lane.

Object Type	Top size, cm	Height, cm	Case / Composition	Metal Content
APM PMN2	∅ 12	5.4	Plastic/TNT'	Pin
APM M14	∅ 5.8	4	Plastic/TNT'	Pin
APM NR22	∅ 5.2	5.5	Plastic/TNT'	No
APM PFM1	12*6.5"	2	Metal/TNT'	Large
Antitank Mine	∅ 40	20	Plastic/TNT'	Large
Metal Disk	∅ 12	0.3	Metal	100%
TDR sensors	various	various	Metal/Plastic	Large

'– SIMULATED

Table B.3 Material parameters of the targets in the grass lane

Appendix C Measurement campaign of 2004

The joint IRCTR/TNO DS&S measurement campaign with the video impulse GPR of IRCTR and the measurement facilities of TNO DS&S was held in the November-December of 2004. The present appendix, which describes the Campaign is organized in the following way: the goals of the campaign, the measurement site and setup descriptions are given in the subchapter C.1 and C.2 ; subchapter C.3 is dedicated to the technical characterization of the equipment output and its comparison to the values of relevant parameters observed during the measurements taken in previous years.

C.1 Goals of the campaign

The main goals of the joint IRCTR/TNO DS&S Measurement Campaign, which was held during the late autumn 2004 at the TNO sandpit, were:

- Demonstration of the IRCTR GPR performance under the controllable conditions
- Acquisition of the set of the C-Scans to be used for evaluation of the data processing algorithms developed by the TNO- DS&S
- Acquisition of the set of the C-Scans to be used for demonstration of the progress in the development of the data processing algorithms made in IRCTR in the year 2004

To this end the following plan of the experiments was accepted:

- The Scanner frame has been set up in the tent sandpit located in the TNO DS&S in Den Haag.
- The GPR had been tested for the stability of its performance in motionless position at the TU Delft and then relocated to the measurement site and connected to the scanner.
- Two sets of the measurements have been made over the presumably empty groundtruth in order to estimate the performance of the equipment on the move
- A groundtruth has been agreed with the TNO side[4] and then set up with the help of Paul Hakkaart of IRCTR and Peter Heijnen from TNO DS&S
- Two sets of measurements have been made over this groundtruth, the resulting data have been analyzed, preprocessed and delivered to the TNO DS&S
- Another groundtruth, answers to my own conception of the interesting measurement, has been set up and the set of C-Scans has been acquired over it
- The technical analysis has been performed over all acquired data and it has been found that certain steps in the preprocessing stage should be made in order to compensate the equipment drift.

[4] Ir. Jan Rhebergen is the first contact person from the TNO DS&S side

- The adequate preprocessing scheme has been developed and all the data have been preprocessed in accordance to it.
- The resulting C-Scans have been processed by the data processing scheme developed in the IRCTR in the years prior to 2003
- The newly algorithms of waveform based clutter suppression, windowed and alternating sign windowed energy projection have been introduced
- The performance of the equipment has been demonstrated in terms of visual demonstration (confidence maps) and Receiver Operator Curves

C.2 Measurement site and set up

The Measurement Campaign has been held at a sandpit located inside TNO DS&S measurements terrain in Den Haag. Unlike the HOM2000 minefield simulating lanes, which are placed in the same location under the open sky, the sandpit is under the tent and is not specifically meant to simulation of the minefield. The pit has dimensions of 10 by 10 metes, is more than 3 meters deep and is filled with highly contaminated sand. It is mainly designed for the experiments with GPR equipment dedicated to the civil engineering and contains some objects, which detection is the main goal of civil GPR, including several pipes and cables. As no civil GPR due to its frequency range is affected by the presence of relatively small pieces of clay, stones, shells etc., there were no efforts made to keep the site clean of such objects. On top of that the heavy human presence on the sand itself prevents any possibility of making the soil/air interface flat. Overall it has to be kept in mind that using the mine-detecting GPR in such conditions means in fact taking the equipment tests onto much higher level of difficulty in comparison to that of the Measurements Campaign [77] on the Waalsdorp lanes [78] in July 2002.

The general placement of the scanner frame and radar on the surface of the sand pitch is sketched in the Figure C.1. As it can be seen from the figure, the scanner frame has been situated almost exactly in the center of the pitch. This decision was forced by the placements in the same pitch of the additional TNO soil water content measurement sub-site and significant amount of highly magnetic soil (both shown in the figure). It was impossible to move the frame closer to the warm house due to the cables hanging there in the air

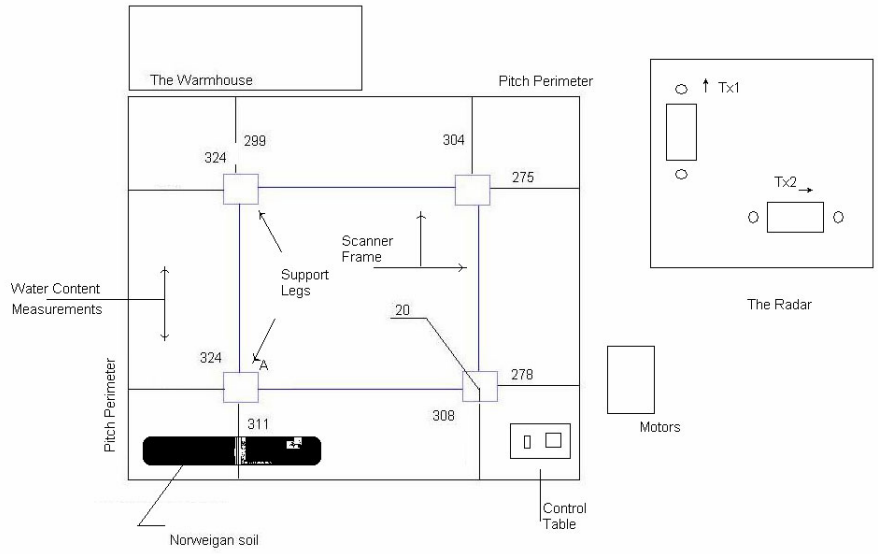

Figure C.1 The placement of the Scanner frame in the sand pit

.

The photos in the Figure C.2 a) and b) show the overall landscape of the measurement site and the character of the roughness of the air-soil interface. The large amount of shells, pieces of clay and other small scatterers is also worth noticing. These objects create random scattering and significantly embarrass application of any background subtraction procedures. Overall, as it can be seen from the photos, the measurements represent the 'rough surface' radar scenario. This scenario is significantly more difficult to energy based detection procedures in comparison to the one observed at HOM2000 lanes (Appendix B).

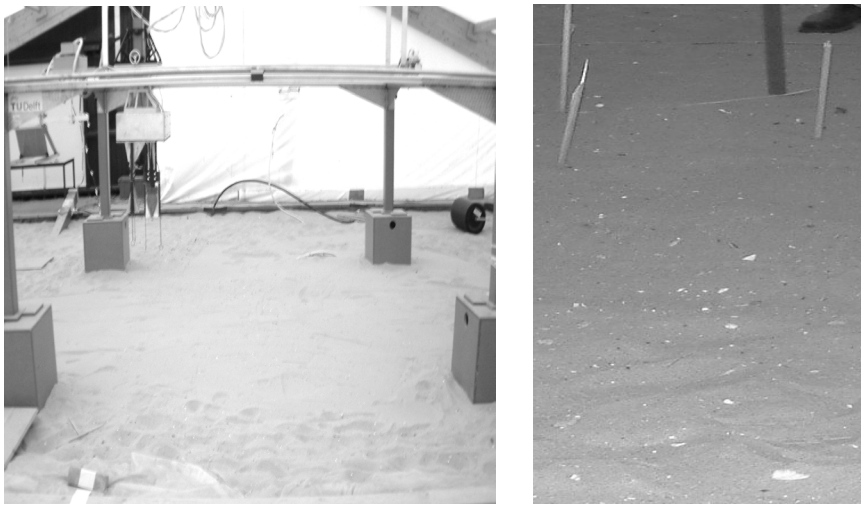

Figure C.2 The General view of the measurements site and the air/ground interface close up

The Radar has been connected to the Scanner frame in such a way that the transmitter antenna 1 was polarized from south to north and consequently the transmitter antenna 2 from east to west. The main movements of the Radar during the measurements were held in South – North direction. The following is the full set of the technical setup of the data acquisition:

- Number of channels: 9 = 2 quasi-monostatic co-polar + 2 bi-static co-polar + 2 quasi-monostatic cross-polar + 2 bi-static cross-polar + calibration channel
- Height of the receivers 30 cm
- Height of the transmitters 58 cm
- The area of scanning is: X*Y = 266*248 cm^2
- Grid density: 0.55 cm dX (inline) and 2 cm dY (cross-line)
- The time window is equal to 10 ns and is sampled into 512 points
- The dot averaging mode is used with N = 64

The measurements have been provided over 4 different ground scenarios: the empty ground (only uncontrolled clutter object present), which is referrod to as the Groundtruth 0, and two main scenarios: the Groundtruth 1 and Groundtruth 2. The Groundtruth 1 is shown in the Figure C.3-a. The numbers represent: 1 - a piece of wood, 2 - plastic cup, 3 - shrapnel, 4- PMN2 mine,5 -piece of clay, 6- M14 mine,7- M14 mine, 8- M14 mine, 9- a piece of clay, 10- M14 mine,11- PMN2 mine,12 - PMN2 mine.

The Groundtruth 2 is shown in the Figure C.3-b. The numbers represent: 1 - PMN2 mine, 2- shrapnel, 3 - a piece of wood, 4 -a piece of clay, 5- several small shells, 6 -a plastic cup, 7- M14 mine, 8 -M14 mine, 9- M14 mine, 10- 3 fifty euro-

cent coins, 11- M14 mine, 12 -PMN2 mine, 13- PMN2 mine, 14 -PMN2 mine. The objects labeled with white labels are surface laid; the gray-labeled ones are at zero or few millimeters depth, and the black–labeled objects are placed at the depth of 5-6 cm. The objects present in the ground are listed in the Table B.2

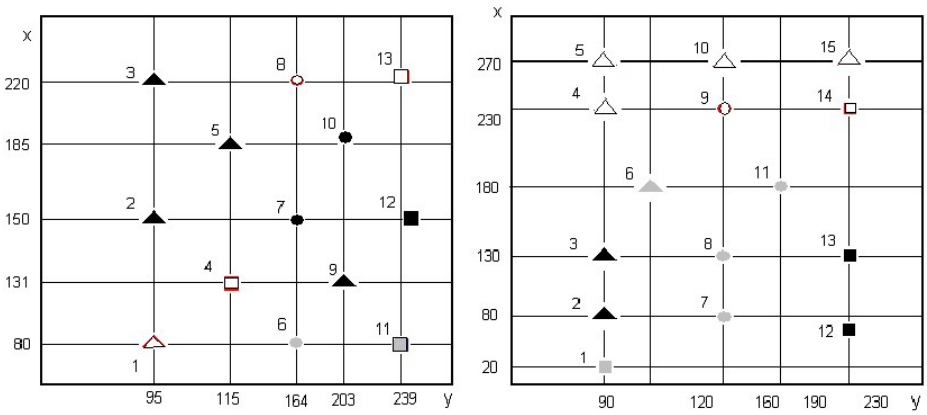

Figure C.3 The ground truths used during the measurements a) scenario – 1, b) scenario - 2

C.3 Technical evaluation of measured data

The following parameters are used to quantify the quality of the data:

- The stability of the main zero crossing
- The stability of the direct wave waveform
- The stability of the direct wave magnitude
- The stability of the quantity of the A-Scans in B-Scans
- The quality of the alignment of the adjacent B-Scans

Stability of the main zero crossing

The character of this time drift recorded during the measurements is shown in Figure C.1 for one of the C-Scans.

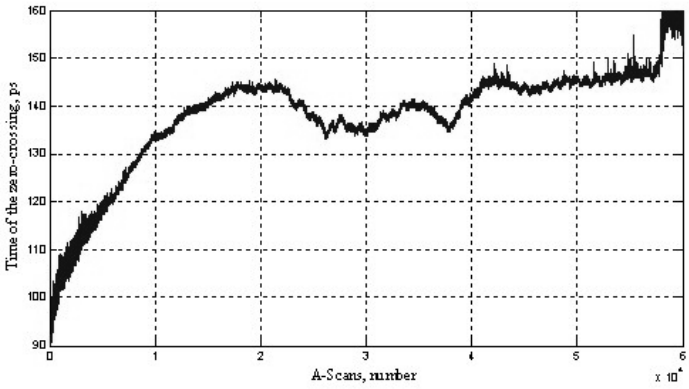

Figure C.1 The long-term drift of the generator (the whole C-Scan)

The Table C.1 compares the parameters of the equipment drift observed during these and past measurements. As it can b seen from the Table, the performance of the equipment has significantly worsened to the present time and hence the preprocessing action should be taken here to compensate for the drift.

Parameters/ Occasion	2002		2003		2004	
	Stand Still	On the Move	Stand Still	On the Move	Stand Still	On the Move
Drift (ps/hour)	3.2	9.137	3.803	12.13	17.8	151
Jitter σ (ps)	0.286	3.4278	0.37	3.7	3.6	3.6

Table C.1 of the stability of the equipment during the years of 2002-2004

It can be noticed that the fast jitter is mainly caused by the effects of the B-Scan switching; this includes the transitional processes in electronics as well as mechanical vibration of the antenna system.

Waveform and signal magnitude stability

The main magnitude of the direct wave changes inside the 7% limits, which is typical performance of the radar. Nevertheless it has been decided that the preprocessing action step of the normalization of the magnitudes to the median value should be always taken for the data of this Measurement Campaign. After the normalization, the waveforms are close enough in the L_2 so no step is taken in an attempt to compensate the instability of the shape of the direct wave.

Stability of the quantity of the A-Scans in B-Scans and (mis)alignment of the adjacent B-Scans

The problem here is the sporadic change of the quantity of A-Scans in B-Scans. In each C-Scan approximately 5 – 7 of the B-Scans have an untypical quantity of the compounding A-Scans. The difference between the typical and untypical amount of A-scans usually lies in the margins of ±1 but can go as far as -3 (see Figure C.1).

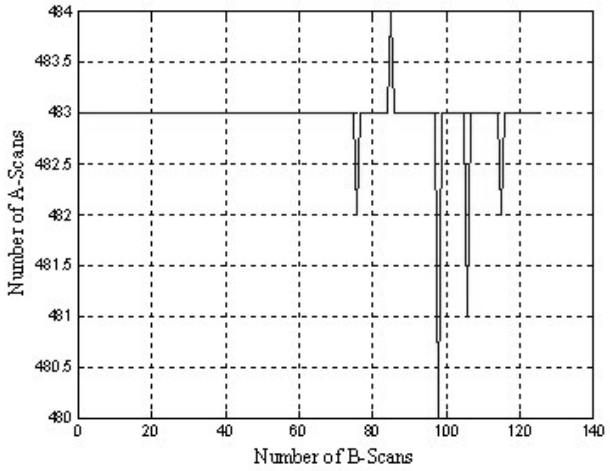

Figure C.1 The number of A-Scans in B-Scans, which compound one of the C-Scans

This leads to the necessity of the introducing of the fake A-Scans, which are obtained on the ends of the relevant B-Scans through the linear interpolation. Another problem, which arises here, is bad alignment of the adjacent B-Scans leading to the deformation of the images in time slices and to worsening of the performance of the SAR algorithm. Hence the preprocessing step should be taken here to compensate the misalignments.

As it has been shown in the following defects are to be compensated before the data is sent to a processing chain:

- The magnitude instability
- The time drift
- The missing A-Scans
- The B-Scans misalignment

These defects can be compensated by means described in the Appendix A.2 .

List of Acronyms

APM	Antipersonnel Plastic Mine
DPS	Data Processing Scheme
DDQ	Decorrelated Distance Qlassifier
DPPC	Data Pre-Processing Chain
EMI	Electro-Magnetic Induction
FA	False Alarm
FAR	False Alarm Rate
FFT	Fast Fourier Transform
GB	Ground Bounce
GPR	Ground Penetrating Radar
HH	Hand Held
HMM	Hidden Markov's Model
IR	Infra-Red
k-NN	k Nearest Neighbors
LMD	Local Maxima Detector
LSM	Local Similarity Measure
LVQ	Learning Vector Quantization
MC	Measurement Campaign
MD	Maximum Deflection
ML	Maximum Likelihood
PLSM	Penalized Local Similarity Measure
ROC	Receiver Operation Characteristics
SAR	Synthetic Aperture Radar
SNR	Signal to Noise Ratio
TNT	Trinitrotoluene (explosive)

References

[1] J. Cornelis, A. Craib, and R. Voles, "*Strategic Study of Humanitarian Demining Prospects"*, The European Union for Humanitarian Demining EUDEM2 Report, 2000.

[2] J. McDonald, J.R. Lockwood, J. McFee, T. Altshuler, T. Broach, L. Carin, R. Harmon, C. Rappaport, W. Scott, and R. Weaver,"Alternatives for landmine detection", Rand Corporation Report, 2003.

[3] Mine Action Coordination Center Report "Mines in South Lebanon. Threat Factsheet #2", *url: http://www.maccsl.org/threatsheets/Threat%20Factsheet2.pdf*

[4] D. J. Daniels, Ed., *Ground Penetrating Radar* (2nd ed.) IEE Pub. , London, UK, 2004.

[5] D. J. Daniels, "GPR for landmine detection, an invited review paper" – *in Proc. of the 10th International Conference on Ground Penetrating Radar*, Delft, The Netherlands, pp. 7 – 10, 2004.

[6] K.C. Ho, and P.D. Gader "A linear prediction land mine detection algorithm for hand held Ground Penetrating Radar", *IEEE Transactions on Geoscience and Remote Sensing*, vol. 40, no. 6, pp. 963-976, June 2002.

[7] P.D. Gader, J.M. Keller, and B.N. Nelson, "Recognition technology for the detection of buried land mines", *IEEE Transactions on Fuzzy Systems*, vol. 9, no. 1, pp. 31-43, February 2001.

[8] K. C. Ho, L.M. Collins, L.G. Huettel, and P.D. Gader, "Discrimination mode processing of EMI and GPR sensors for hand-held land mine detection" , *IEEE Transactions on Geoscience and Remote Sensing*, vol. 42, no. 1, pp. 249-263, January, 2004.

[9] M.Sato, J. Fujiwara, X Feng, Z.-S. Zhou, and T. Kobayashi, "Evaluation of a Hand-held GPR MD sensor system (ALIS)" - *in Proc. of IARP International workshop on Robotics and Mechanical Assistance in Humanitarian Demining (HUDEM2005)*,pp. 21-26, June, 2005.

[10] Niitek, Inc. Niitek web page url http://www.niitek.com.

[11] J. J. Legarsky, J.T. Broach, and S.S. Bishop, "Processing of GPR data from NIITEK landmine detection system", *In Proc. of the SPIE Detection and Remediation Technologies for Mines and Minelike Targets VIII*, vol.5089, pp. 1375—1382, 2003.

[12] Q. Zhu and L.M. Collins, "Application of feature extraction methods for landmine detection using Wichmann/Niitek Ground Penetrating Radar", *IEEE Transactions on Geoscience and Remote Sensing*, vol. 43, no. 1, pp. 81-85, January, 2005.

[13] R.B. Cosgrove, P. Milanfar, and J. Kositsky, "Trained detection of buried mines in SAR images via the deflection-optimal criterion", *IEEE Transactions on Geoscience and Remote Sensing*, vol. 42, no. 11, pp. 2569-2575, November 2004.

[14] T. Wang, O. Sjahputera, J. M. Keller, and P.D. Gader, "Feature analysis for forward-looking landmine detection using GPR", *In Proceedings of the SPIE Detection and Remediation Technologies for Mines and Minelike Targets X*, vol. 5794, pp. 1233-1244, 2005.
[15] "Multisensor vehicle-mounted mine detector" *USA Patent#* 6026135.
[16] GeoCenters EFGPR Website url:
http://www.geo-centers.com/products/EFGPR-Overview-1-03.pdf
[17] Defence R&D Canada Suffield Company Website url:
http://www.dres.dnd.ca/ResearchTech/Products/MilEng_Products/RD20001_ILDP/
[18] V. Kovalenko, A. Yarovoy, F. Roth, L.P. Ligthart, and R.F. Bloemenkamp "Multi-Waveform Full-polarimetric GPR Sensor for Landmine Detection: First Experimental Results" *in Proc. of EUDEM2-SCOT*, Brussels, Belgium, September 2003, pp 554 - 560
[19] P. D. Gader, B. Nelson, H. Frigui, G. Vaillette, J. Keller, "Fuzzy Logic Detection of Landmines with Ground Penetrating Radar," Signal Processing, Special Issue on Fuzzy Logic in Signal Processing, vol. 80, No. 6, pp. 1069-1084, June, 2000.
[19] P.D. Gader, M. Mystkowski, and Y. Zhao, "Landmine detection with Ground Penetrating Radar using hidden Markov models", *IEEE Transactions on Geoscience and Remote Sensing*, vol. 39, no. 6, pp. 1231-1244, June, 2001.
[20] Y. Zhao, P.D. Gader, P. Chen, and Y. Zhang, "Training DHMMs of mine and clutter to minimize landmine detection errors", *IEEE Transactions on Geoscience and Remote Sensing*, vol. 41, no. 5, pp. 1016-1024, May, 2003.
[21] A.M. Zoubir, I.J. Chant, C.L. Brown, B. Barkat, and C. Abeynayake, "Signal Processing Techniques for Landmine Detection Using Impulse Ground Penetrating Radar", *IEEE Sensors Journal*, vol. 2, no. 1, pp. 41-51, February, 2002.
[22] J.B. Rhebergen, A.P.M Zwamborn, and D.V. Giri, "Design of an ultra-wideband ground-penetrating radar system using impulse radiating antennas", *in Proc of Second International Conference on the Detection of Abandoned Land Mines*, pp. 45 – 49, October, 1998.
[23] J. LoVetri, S. Primak, B.J.A.M. van Leersum, and A.P.M Zwamborn "Feasibility study into the identification of landmines using UWB radar: an analysis using synthesized data" *in Proc. of Ultra-Wideband Short-Pulse Electromagnetics 4 Conference*, 425-432, June, 1998.
[24] C. Pichot, J.-Y. Dauvignac, C. Dourthe, I. Aliferis, and E. Guillanton. "Inversion algorithms and measurement systems for microwave tomography of buried objects". *In Proc. of the 16th IEEE Instrumentation and Measurement Technology Conference, IMTC/99*, volume 3, pages 1570–1575,May 24–26, 1999. Venice, Italy.
[25] M. Sato, "Bistatic GPR system for landmine detection using optical electric field", *in Proc. of IEEE Antennas and Propagation Society International Symposium*, vol. 2, pp. 207-210, 2003.

[26] F. Roth, P. van Genderen, and M. Verhaegen, “Radar scattering models for the identification of buried low-metal content landmines”, - *in Proc. of 10th International Conference on GPR*, Delft, The Netherlands, pp. 689-692, 2004.
[27] I.L. Morrow and P. van Genderen, "Effective imaging of buried dielectric objects", *IEEE Transactions on Geoscience and Remote Sensing*, vol. 40, no. 4, pp. 943-949, June, 2002.
[28] P. van Genderen, "Multi-waveform SFCW radar", *in Proc. of 33rd European Microwave Conference*, vol.2, pp. 849 - 852, 2003.
[29] A.G. Yarovoy, L.P. Ligthart, A.D. Schukin, and I.V. Kaploun, “ Polarimetric Video Impulse Radar for Landmine Detection”, *Subsurface Sensing Technologies and Applications*, vol.3, no.4, pp. 271-293, October, 2002.
[30] A.G. Yarovoy, A.D. Schukin, I.V. Kaploun, and L.P. Ligthart, “The dielectric wedge antenna,” *IEEE Transactions on Antennas & Propagation*, vol. 50, No. 10, pp. 1460-1472, October, 2002.
[31] A.G. Yarovoy, L.P. Ligthart, A.D. Schukin, and I.V. Kaploun, “Multi-waveform full-polarimetric video impulse radar for landmine detection” *in Proc. of 33rd European Microwave Conference*, vol.3, pp. 1003 - 1006, 2003.
[32] J. Groenenboom, and A.G.Yarovoy, ”Data processing and imaging in GPR system dedicated for landmine detection”, *Subsurface Sensing Technologies and Applications*, vol.3, No.4, pp.387-402, October, 2002.
[33] B. Karlsen, J. Larsen, H.B.D. Sorensen, and K.B. Jakobsen, "Comparison of PCA and ICA based clutter reduction in GPR systems for anti-personal landmine detection” *in Proc. of 11th IEEE Signal Processing Workshop*, pp. 146 - 149, 2001.
[34] D. Carevic "Wavelet-based method for detection of shallowly buried objects from GPR data" *in Proc. of Conference on Information, Decision and Control*, pp. 201-206, 1999.
[35] I.I. Jouny and M.P. Kolba, "Clutter suppression and feature extraction for land mine detection using ground penetrating radar" *in Proc. of IEEE Antennas and Propagation Society International Symposium*, vol. 2, pp. 203-206, 2003.
[36] A. van der Merwe and I.J. Gupta, “A novel signal processing technique for clutter reduction in GPR measurements of small, shallow landmines”, *IEEE Transactions on Geoscience and Remote Sensing*, vol. 38, no. 6, pp. 2627-2637, November, 2000.
[37] C. Rappaport, M. El-Shenawee, and H. Zhan, “Suppressing GPR clutter from randomly rough ground surfaces to enhance non-metallic mine detection”, *Subsurface Sensing Technologies and Applications*, vol. 4, no. 4, pp. 311 – 326, October, 2003.
[38] J. F. Claerbout *Imaging the Earth's Interior*, Blackwell Science Ltd., 1985
[39] S. Gindikin and P. Michor, editors, *75 Years of Radon Transform*, International Press, 1994.
[40] J.C. Curlander and R. McDonough, *Synthetic Aperture Radar: Systems and Signal Processing*, Wiley & Sons Inc., USA, 1992.

[41] N. Osumi and K. Ueno, “Microwave holographic imaging method with improved resolution”, *IEEE Transactions on Antennas and Propagation*, vol. AP-32, no. 10, pp. 1018-1026, October, 1984.

[42] G. W. K. Gu and J. Li, “Migration based SAR imaging for ground penetrating radar systems," *IEE Proc. on Radar, Sonar, and Nav*., vol. 151, no. 5, pp. 317 - 325, August, 2004

[43] J. Song, Q. H. Liu, P. Torrione, L. Collins, "Two-Dimensional and Three-Dimensional NUFFT Migration Method for Landmine Detection Using Ground-Penetrating Radar", *IEEE Transactions on Geoscience and Remote Sensing*, vol. 44, no. 6, pp. 1462-1469, April, 2006.

[44] R. Benjamin, I.J. Craddock, G.S. Hilton, S. Litobarski, E. McCutcheon, R. Nilavalan, and G.N. Crisp, "Microwave detection of buried mines using non-contact, synthetic near-field focusing", *IEE Proc. on Radar, Sonar, and Nav*., vol. 148, no. 4, pp. 233 - 240, August, 2001

[45] K. Fukunaga, *Introduction to Statistical Pattern Recognition* (2nd ed.), Academic Press, 1990.

[46] B. Picinbono and P. Duvaut, “Optimal linear-quadratic systems for detection and estimation,” *IEEE Trans. Inform. Theory*, vol. 34, pp. 304–311, March, 1988.

[47] A.H. Gunatilaka, and B.A. Baertlein, "Feature-Level and Decision-Level Fusion of Noncoincidently Sampled Sensors for Land Mine Detection" IEEE Trans. on Patt, Anal. and Mach. Int., vol. 23, No. 6, pp. 577 - 589, June, 2001.

[48] G. Shafer, *A Mathematical Theory of Evidence*, Princeton Univ. Press, USA, 1976.

[49] N. Milisavljevic´ and I. Bloch, "Sensor Fusion in Anti-Personnel Mine Detection Using a Two-Level Belief Function Model" IEEE Trans. on Syst., Man, and Cybern.—part C: Appl. and Rev., vol. 33, no. 2, pp. 269 - 283, May, 2003.

[50] S. Perrin, E. Duflos, P. Vanheeghe, and A. Bibaut, "Multisensor fusion in the frame of evidence theory for landmines detection," *IEEE Trans. Syst., Man, Cybern. C*, vol. 34, no. 4, pp. 485-498, November, 2004.

[51] F. Cremer, *Polarimetric Infrared and Sensor Fusion for the Detection of landmines*, Ph.D. Thesis, TU Delft, The Netherlands, 2003

[52] N. L. Johnson, “Systems of frequency curves generated by methods of translation”, *Biometrika*, vol. 36, pp. 274 – 282, 1949.

[53] F. Roth, P. van Genderen, and M. Verhaegen ,“Convolutional models for buried target characterization with ground penetrating radar”, *IEEE Transactions on Antennas and Propagation*, vol. 53, no. 11, pp. 3799-3810, November, 2005.

[54] X. Xu, E.L. Miller, C.M. Rappaport, and G.D. Sower, “Statistical method to detect subsurface objects using array Ground-Penetrating Radar”, *IEEE Transactions on Geoscience and Remote Sensing*, vol. 40, no. 4, pp. 963-976, April, 2002.

[55] D. Potin, P. Vanheeghe, E. Duflos, and M. Davy, "An Abrupt Change Detection Algorithm for Buried Landmines Localization", *IEEE Transactions on Geoscience and Remote Sensing*, vol. 44, no. 2, pp. 1016-1024, May, 2006.

[56] D. Potin, P. Vanheeghe, E. Duflos, and M. Davy, "Landmines Ground-Penetrating Radar Signal Enhancement by Digital Filtering"", *IEEE Transactions on Geoscience and Remote Sensing,* vol. 44, no. 9, pp. 2393-2406, May, 2006.

[57] D.J. Hall *Mathematical Techniques in multisensor data fusion.*Artech House, Inc., USA, 1992

[58] V. Kovalenko, A. Yarovoy, L.P. Ligthart "Statistical Analysis of High Resolution Subsurface Images with Application to Landmines Detection" *in Proc. of International Symposium on Antennas and Propagation*, Sendai, Japan, pp. 805-808, August, 2004.

[59] J. Laaksonen and E. Oja "Classification with Learning k-Nearest neighbors", *In. Proc. of ICNN'96*, pp 1480 – 1483, USA, June, 1996.

[60] A.K. Jain and D. Zonker "Feature Selection: evaluation application and small sample performance", *IEEE Trans. On Pattr. Anal. Ans Mach. Intl.,* vol 19, no 2, pp. 153-158, February, 1997.

[61] F. Roth "*Convolutional Models for Landmine Identification with Ground Penetrating Radar"* Ph.D. Thesis, TU Delft, The Netherlands, 2004.

[62] P.D. Gader , W.-H. Lee, and J.N. Wilson, "Detecting landmines with Ground-Penetrating Radar using feature-based rules, order statistics, and adaptive whitening", *IEEE Transactions on Geoscience and Remote Sensing*, vol. 42, no. 11, pp. 2522-2534, November, 2004.

[63] Collins, L. and P.Torrione, "Application of texture feature classification methods to landmine/clutter discrimination in off-lane GPR data" in Proc. of Geoscience and Remote Sensing Symposium, vol. 3, pp.1620-1623, 2004.

[64] C.-C. Yang and N. Bose, "Landmine detection and classi¯cation with complex-valued hybrid neural network using scattering parameters dataset," *IEEE Trans. Neural Networks*, vol. 16, no. 3, pp. 743-753, May, 2005.

[65] J.E. Mast and E.M. Johansson, "Three-dimensional ground penetrating radar imaging using synthetic aperture time-domain focusing", *SPIE report*, 1994.

[66] H. Brunzell *"Signal processing techniques for detection of buried landmines using GPR"*, Ph. D. Thesis, TU Chalmers, Sweden, 1998.

[67] A.W. Bowman, and A. Azzalini, Applied Smoothing Techniques for Data Analysis, Oxford University Press, UK, 1997.

[68] A.R. Webb, *"Statistical Pattern Recognition (2nd ed.)"*, Wiley , USA, 2002

[69] C.J. Huberty, *"Applied discriminant analysis"* . Wiley-Interscience, USA, 1994

[70] V. Kovalenko, and A. Yarovoy , "Alternating-Sign Windowed Energy Projection of SAR Focused GPR Data", *in Proc. of the European Radar Conference*, Paris, France, October, 2005, pp. 399-402

[71] P. Chevalier and B. Picinbono, “Complex linear-quadratic systems for detection and array processing,” *IEEE Trans. Signal Processing*, vol. 44, pp. 2631–2633, October, 1996.

[72] C.D. Meyer, *"Matrix Analysis and Applied Linear Algebra",* Cambridge University Press, UK, 2001.

[73] C. R. Baker, “Optimum quadratic detection of a random vector in Gaussian noise,” *IEEE Trans. Commun*., vol. COM-14, pp. 802–805, December, 1966.

[74] S. S. Shapiro, and A.J. Gross, *Statistical Modeling Techniques*, Marcel Dekker Inc., 1981.

[75] R.B. Ash and C.A. Doleans-Dade *"Probability & Measure Theory, 2nd Ed.)",* Academic Press, 1999

[76] V. Kovalenko, and A. Yarovoy, “Analysis Of Target Responses And Clutter Based On Measurements At Test Facility For Landmine Detection Systems Located At TNO-FEL” – *in Proc. of the 2nd International Workshop on Advanced Ground Penetrating Radar (IWAGPR)*, Delft, The Netherlands, pp. 82 – 87, May 2003.

[77] A.G. Yarovoy, W. de Jong, V. Kovalenko, F. Roth, R.F. Bloemenkamp,F. Cremer, J.B. Rhebergen, P.J. Fritz, J. van Heijenoort, P. Hakkaart, M.A. Ouwens, “Multi-Sensor Measurement Campaign at TNO-FEL Test Lanes in July 2002” in Proc. of IGARSS, Toulouse, France, ISBN 0-7803-7930-6 CDROM, 2003.

[78] W. de Jong, H.A. Lensen, and Y.H. Janssen, “Sophisticated test facility to detect land mines”, in Proc. of Detection and Remediation Technologies for Mines and Minelike Targets IV, SPIE Proceedings, vol. 3710, pp.1409-1418, 1999.

[79] V. Kovalenko, A. Yarovoy, and L.P. Ligthart, “Reduction of Clutter in Data of Mine-Detecting GPR” - *accepted for publication in the book of Proc. of EuroEM 2004*, Magdeburg, Germany, July, 2004.

[80] V. Kovalenko, A. Yarovoy, and J.B. Rhebergen, "Joint IRCTR / TNO-DS&S measurement campaign for AP-mine detection with VIR GPR", – *in Proc. of the 3rd International Workshop on Advanced Ground Penetrating Radar (IWAGPR)*, Delft, The Netherlands, pp. 31 – 36, May, 2005.

[81] F.M. Dickey, and L.A. Romero, “Normalized correlation for pattern recognition”, *Optics Letters,* vol. 16, no. 15, pp. 1186-1188, August 1991.

[82] M. Born, “*Principles of optics*”, Cambridge U. Press, 1999.

[83] G. Sewell, *"Computational Methods of Linear Algebra (2nd ed.)"* Wiley-Interscience, USA, 2005.

[84] V.Kovalenko, A.Yarovoy, F.Roth, L.P. Ligthart “Full-polarimetric measurements over a minefield-like test site with the video impulse ground penetrating radar” - *Proc. SPIE 5089, Detection and Remediation Technologies for Mines and Minelike Targets VIII*, Orlando, FL, USA, pp. 448-456, April, 2003.

[85] V. Kovalenko, A. Yarovoy, and L.P. Ligthart, “Object Detection in 3D UWB Subsurface Images” in *Proceedings of EuMW*, Amsterdam, The Netherlands, pp. 237-240, October, 2004.

[86] A.B. Kostinsky, and W.-M. Boerner “On Foundation of Radar Polarimetry” *IEEE Transactions on Antennas & Propagation*, vol. 34, No. 12, pp. 1395-1404, December, 1986.

[87] D. Freedman, R. Pisani, and R. Purves "Statistics", W. W. Norton & Company, USA, 1997.

[88] V.Kovalenko, A.Yarovoy, L.P. Ligthart “Statistical Properties of Antipersonnel Mine Signatures in SAR-Processed GPR Images*” in Proc. Of 10th International Conference on Ground Penetrating Radar*, Delft, The Netherlands, pp. 685 – 688, June, 2004.

[89] A. Yarovoy, F. Roth, V. Kovalenko, and L.P. Ligthart, "Application of UWB Near-Field Polarimetry to Classification of GPR Targets" , *accepted for EuROEM'04 book*

[90] R. Mukundan "Moment Functions in Image Analysis: Theory & Applications", World Scientific Publishing , USA, 1998.

[91] V.Kovalenko, A.Yarovoy, A.Fogar “Impact of ground clutter on buried object detection Ground Penetrating Radar” *in Proc. of IGARSS 2003 IEEE International Geoscience and Remote Sensing Symposium*, Toulouse, France, ISBN 0-7803-7930-6 CDROM

[92] V.Kovalenko, A. Yarovoy, F.Roth, L.P. Ligthart, and R.F. Bloemenkamp “Multi-Waveform Full-polarimetric GPR Sensor for Landmine Detection: First Experimental Results” *in Proc. of EUDEM2-SCOT – 2003 Brussels*, Belgium, September 15-18, 2003, pp 554 - 560

[93] V.Kovalenko, A. Yarovoy, L.P. Ligthart “Application of Deconvolution and Pattern Search Techniques to High Resolution GPR Data” *International Conference on Electromagnetics in Advanced Applications ICEAA'03*, Turin, Italy, September, 2003, pp. 699 – 702.

[94] F. Cremer, W. de Jong, K. Schutte, “Fusion of polarimetric infrared features and GPR features for landmine detection", – *in Proc. of the 2nd International Workshop on Advanced Ground Penetrating Radar (IWAGPR)*, Delft, The Netherlands, pp. 222 – 227, May 2003.

Summary

Ground Penetrating Radar (GPR) is seen as one of several promising technologies aimed to help mine detection. GPR is sensitive to any inhomogeneity in the ground. Therefore any APM regardless of the metal content can be detected. On the other hand, all the inhomogeneities, which do not represent mines, show up as a clutter in GPR images. Moreover, it is known that reflectivity of APM is often weaker than that of stones, pieces of shrapnel and barbed wire, etc. Altogether these factors cause GPR to produce unacceptably high false alarm rate whilst it reaches the 99.6% detection rate which is prescribed by an UN resolution as a standard for humanitarian demining.

The main goal of the work presented in the thesis is reduction of the false alarm rate while keeping the 99.6% detection rate intact. To reach this goal a set of data processing algorithms is developed and organized into an unsupervised target detection scheme. These algorithms are dedicated to clutter suppression and simultaneous detection of APM signatures in both GPR raw data and images resulting from them.

The developed algorithms constitute together the following achievements:

- An unsupervised generalized likelihood ratio test-based feature fusion framework;
- A waveform based target detection/clutter suppression;
- Advanced methods for construction of GPR maps

The *unsupervised generalized likelihood ratio test based feature fusion framework*, which has been suggested in this thesis, takes as input an arbitrary amount of confidence maps corresponding to training and testing sites. The output of the framework is a list of target locations. The framework uses training data which can come from independent and non-coincident measurements with different radars and even sensors. The data from each of the sensors are processed independently to result in several *detection lists*. Every detection in these lists is accompanied with one or several features each represented by a scalar number. A decision level fusion is applied to reconcile the lists i.e. to associate the detections in them with the appropriate physical locations. Then the binary hypothesis testing is executed for the reconciled locations separating them on clutter and target lists. The generalized likelihood ratio test is employed to this end. The *feature pre-normalization* via Johnson's transform in suggested by the author to be used prior the testing. It is shown in the thesis that such approach outperforms the direct generalized likelihood ratio testing *ad. hoc.* based fusion techniques.

The waveform based target detection/clutter suppression algorithm, which detects disc-shaped APM in heavy clutter with low false alarm rate, has been developed by the author. The algorithm detects a class of low-metal APM with a cylindrical shape (such as PMN2, M14, and NR22 etc.) using just a single reference target return. It suppresses clutter responses from friendly objects while marking

the presence of targets with sharp monopulses and preserving the spatial pattern inherent to localized objects. The algorithm is insensitive to the reflectivity and physical diameter of the target and also tolerates certain volatility in the properties of the hosting soil. This algorithm is superimposed with a focusing technique to further improve the mine detectability.

A number of *improved projection techniques*, which allow better detection of APM in focused GPR images is also developed by the author. These utilize the prior knowledge on the character of the spatial correlation properties of target images and allow detection of the burial depth of the target.

The algorithms suggested in the thesis were tested on the data acquired during two separate measurement campaigns held at the special facilities for testing of mine detection systems. It has been shown, that the fused multi-feature detection that uses the algorithms reported in this thesis, significantly decreases the false alarm rate in comparison to the previously published studies for the same minefields.

Vsevolod Kovalenko

Samenvatting

Ground Penetrating Radar (GPR) wordt gezien als een van de veel belovende technieken die gericht zijn op het ondersteunen van de mijndetectie. GPR is gevoelig voor elke inhomogeniteit in de grond. Om die reden zal elke APM gedetecteerd worden, of er metaaldelen in zitten of niet. Anderzijds worden alle inhomogeniteiten die niet door mijnen veroorzaakt worden, zichtbaar als clutter in de GPR beelden. Belangrijker nog, het is bekend dat de reflectiviteit van APM vaak zwakker is dan die van stenen, resten van granaten and prikkeldraad, etc. Al deze factoren zorgen er voor dat de GPR een onacceptabel hoog percentage valse alarmen geeft, terwijl het de detectienorm van 99,6% haalt zoals vastgesteld door een VN-resolutie voor humanitair ontmijnen.

Het belangrijkste doel van het werk dat in dit proefschrift wordt gepresenteerd is de reductie van het percentage valse alarmen met behoudt van het detectienorm van 99.6%. Om dit doel te bereiken werd een set algoritmen voor dataverwerking ontwikkeld en bijeengebracht in een unsupervised schema voor doelwitdetectie. Deze algoritmen worden gebruikt voor de onderdrukking van clutter en tegelijkertijd de detectie van de APM-signatuur, zowel uit de onbewerkte data van de GPR als uit de beelden die hieruit voortkomen.

De ontwikkelde algoritmen vormen samen de volgende resultaten:

- Een, op testen van het unsupervised gegeneraliseerd waarschijnlijkheidspercentage gebaseerd, frame dat eigenschappen bij elkaar brengt of bundelt;
- Doelwitdetectie & clutter-onderdrukking op golfvorm gebaseerd;
- Geavanceerde methoden voor de samenstelling van GPR kaarten.

De unsupervised gegeneraliseerde waarschijnlijkheids verhouding test gebaseerde eigenschappen fusion structuur, zoals voorgesteld in dit proefschrift, gebruikt als input een arbitrair aantal confidentiekaarten die afgeleid zijn van training- en testlocaties. De output van het frame wordt gevormd door een lijst doelwitlocaties. Het frame gebruikt de trainingsgegevens die afkomstig kunnen zijn van onafhankelijke en niet-coïncidentele metingen met verschillende radars en zelfs sensoren. De data van elk van de sensors worden onafhankelijk verwerkt en leveren zo verschillende detectielijsten. Elke detectie in deze lijsten gaat samen met een of meer eigenschappen elk weer gerepresenteerd door een scalair nummer. Een fusie van besluitniveaus wordt toegepast om de lijsten met elkaar in overeenstemming te brengen, ofwel om de in deze lijsten weergegeven detecties in verbinding te brengen met de geschikte fysieke locaties. Hierna wordt de binaire test van de hypothese uitgevoerd voor de in overeenstemming gebrachte locaties waarbij scheiding tot stand komt tussen clutter en doelwitlijsten. Hiertoe wordt de test van het gegeneraliseerde waarschijnlijkheidspercentage toegepast. Voorafgaand aan het testen wordt de eigenschappen pre-normalization via Johnson's transformatie aangeraden door de auteur. Het wordt in het proefschrift

aangetoond dat een dergelijke benadering een beter resultaat oplevert dan de, op ad hoc testen van het directe gegeneraliseerde waarschijnlijkheidspercentage gebaseerde, fusietechnieken.

De auteur ontwikkelde de op de golfvorm gebaseerde doelwitdetectie / clutter-onderdrukking algoritmen, die de komvormige APM detecteert in heavy clutter met en laag percentage valse alarmen. Het algoritme detecteert een klasse APM met laag metaalgehalte en een cilindrische vorm (zoals de PMN2, M14, en NR22 etc.) waarbij slechts een enkel referentiedoel return. Het onderdrukt de clutter respons van neutrale objecten terwijl de aanwezigheid van doelwitten met scherpe monopulsen worden gemarkeerd waarbij het ruimtelijk patroon dat inherent is aan gelokaliseerde objecten, wordt behouden. Het algoritme is ongevoelig voor de reflectiviteit en fysieke diameter van het doelwit en kan ook een zekere vluchtigheid in de eigenschappen van de omringende bodem aan. Dit algoritme is gesuperponeerd met een techniek van focussen om de detectie van mijnen verder te verbeteren.

Een aantal verbeterde projectietechnieken, die een verbeterde detectie van APM in GPR beelden die gefocust zijn, werden eveneens door de auteur ontwikkeld. Deze benutten de voorkennis, met betrekking tot het karakter van de ruimtelijke correlatie-eigenschappen van de doelwitbeelden, en maken detectie mogelijk waarbij de diepte, waarop het doelwit is begraven, aangegeven wordt.

De algoritmen die in dit proefschrift worden voorgesteld werden getest op de data die bij twee afzonderlijke meetsessies die op speciale testlocaties voor mijnendetectiesystemen werden gehouden. Het werd aangetoond dat detectie met gefuseerde multi-eigenschap detectie die de algoritmen uit dit proefschrift gebruikt een aanzienlijke verlaging van het percentage valse alarmen laat zien in vergelijking tot eerder gepubliceerde onderzoeken met betrekking tot dezelfde mijnenvelden.

Vsevolod Kovalenko

Acknowledgements

First and foremost, I would like to thank my promotors and supervisors, Professor Leo Ligthart and Professor Alex Yarovoy.

The daily guidance tirelessly provided by Professor Yarovoy allowed this thesis to be completed. His genuine interest in every idea I was coming up with and his unquestionable expertise in the field of GPR made the research fruitful. As one example, it was his foresight that allowed the idea of Gaussian-shaped penalty functional to be developed.

The continuous support and guidance provided by Professor Leo Ligthart were absolutely necessary for this thesis to come to the conclusion. His keen interest in every single obtained result, and the perspective he always had helped so much to keep the research on track and to structure the thesis. His requirements on the clearness of explanations for the obtained results helped a lot not only to potential readers of the thesis but also to me.

A research in which theoretical considerations are combined with experimental results always requires a team work. Such a team is well established in IRCTR where I was lucky enough to pursue my degree. The measurement campaigns, which provided the data necessary for my research, were assisted by Paul Hakkart, Johan Zeiderveld, and Joost van Heijenoort to whom I express my sincere gratitude.

I also want to thank Jan Rhebergen of TNO DS&S for his help in the organization of the measurement campaigns. Besides, he provided the opportunity for me to work on the restricted terrain in the TNO.

I would like to thank those who helped me in various aspects of the research and official matters in IRCTR. I want to thank Dr. Oleg Krasnov with whom I had many valuable discussions, scientific and otherwise. I express my gratitude to Laura Bauman and Mia van der Voort – Kesser who helped enormously with various types of formal matters.

Special thanks go to my old friends and teachers from Radiointroscopy department of the Institute for Radio Physics and Electronics in Kharkov, Ukraine. In particular, I would like to express my sincere gratitude to the head of the department and my supervisor since university years Professor Dr. Sci. S.A. Masalov and to Dr. G.P. Pochanin who introduced me to the world of radar about a decade ago.

Finally, I would like to thank my parents, Larissa and Oleg Kovalenko who gave me so much and demanded so little. I want to express my deepest gratitude to my wife Tatyana whose love and support have been felt during all these years. And last but not least, I am very grateful to our little Anastasia, who is the source of the pure inspiration for me.

Vsevolod Kovalenko

About the Author

Vsevolod Kovalenko was born in Kharkov, Ukraine January 20, 1973. After completing his high school study he entered the Mechanics and Mathematics Department of the Karazin's Kharkov National University. He has graduated from the University in 1995 with a Specialist (Master of Sciences) degree in Applied Mathematics. Upon the graduation he joined the Institute for Radiophysics and Electronics of the National Academy of Sciences of Ukraine in Kharkov as a research engineer. During his stay at the IRE he was engaged in the development of software and algorithms for Ground Penetrating Radar data acquisition and processing.

In the beginning of 2002 he came to the International Research Centre for Telecommunications and Radar (IRCTR) where he joined the team working on the project 'Advanced Re-Locatable Multi-Sensor System for Buried Landmine Detection'. He again was responsible for the development of the software dedicated to data acquisition, pre-processing, and technical evaluation. The results obtained during this research allowed him to pursue a Ph.D. degree. He switched to promovendus status in 2004 and focused his research on the algorithms for the detection of antipersonnel landmines under the guidance of Professor L.P. Ligthart and Professor A.G. Yarovoy.

Since 2002 Vsevolod Kovalenko has had 20 research articles published or accepted to be published in major journals and refereed international conferences on the subject of development of algorithms for GPR data acquisition and processing with focus on the detection of antipersonnel landmines.

Currently Vsevolod Kovalenko continues his research in IRCTR. He is engaged in the project EXTENT where he studies algorithms for extended targets detection with polarimetric radar.

Publications by the Author

IEEE Journal

V. Kovalenko, A. Yarovoy, L.P. Ligthart, "A Novel Clutter Suppression Algorithm for Landmine Detection with GPR" – accepted for publication in *IEEE Transactions. on Geoscience and Remote Sensing*

International Conferences

V.Kovalenko, A.Yarovoy , "Analysis Of Target Responses And Clutter Based On Measurements At Test Facility For Landmine Detection Systems Located At Tno-Fel" – in Proc. of the 2nd International Workshop on Advanced Ground Penetrating Radar (IWAGPR), May 14-16, 2003, Delft, The Netherlands, pp. 82 – 87.

V.Kovalenko, A.Yarovoy, F.Roth, L.P. Ligthart, "Full-polarimetric measurements over a minefield-like test site with the video impulse ground penetrating radar" – *in Proc. SPIE 5089, Detection and Remediation Technologies for Mines and Minelike Targets VIII*, April 21-25, 2003, Orlando, FL, USA, pp. 448-456.

V. Kovalenko, A. Yarovoy, F. Roth, L.P. Ligthart, and R.F. Bloemenkamp, "Multi-Waveform Full-polarimetric GPR Sensor for Landmine Detection: First Experimental Results" *in Proc. of EUDEM2-SCOT*, Brussels, Belgium, September 2003, pp. 554 – 560.

A.Yarovoy, **V. Kovalenko,** A. Fogar, "Impact of ground clutter on buried object detection by ground penetrating radar" - *in Proc. of IGARS'03*, July 2003, pp. 755 – 757.

V. Kovalenko, A. Yarovoy, L.P. Ligthart, "Application of Deconvolution and Pattern Search Techniques to High Resolution GPR Data" - *in Proc. of International Conference on Electromagnetics in Advanced Applications ICEAA'03*, Turin, Italy, September 8-12, 2003, pp 699 – 702.

V. Kovalenko, A.Yarovoy, L.P. Ligthart, "Statistical Properties of Antipersonnel Mine Signatures in SAR-Processed GPR Images" - *in Proc. of 10th International Conference on Ground Penetrating Radar*, June 21-24, Delft, The Netherlands, 2004, pp. 685 – 688.

A.Yarovoy, **V. Kovalenko,** F.Roth, E. Ligthart, A. Fogar, L.P. Ligthart, "Landmine detection and discrimination based on GPR data" - *in Proc. of 10th International Conference on Ground Penetrating Radar*, June 21-24, Delft, The Netherlands, 2004, pp. 673 – 676.

V. Kovalenko, A. Yarovoy, L.P. Ligthart, "Statistical Analysis of High Resolution Subsurface Images with Application to Landmines Detection" *in Proc. of International Symposium on Antennas and Propagation*, August 18-21, Sendai, Japan, 2004, pp. 805-808.

V. Kovalenko, A.Yarovoy, L.P. Ligthart, "Object Detection in 3D UWB Subsurface Images" in proceedings of EuMW, Amsterdam, The Netherlands, October 11-15, 2004, pp. 237-240.

V. Kovalenko, A.Yarovoy, L.P. Ligthart, "Reduction of Clutter in Data of Mine-Detecting GPR" –*in the book of Proc. of EuroEM 2004*, July 12-16,2004, Magdeburg, Germany, pp. 733 – 741.

A. Yarovoy, F. Roth, **V. Kovalenko**, and L.P. Ligthart, "Application of UWB Near-Field Polarimetry to Classification of GPR Targets" –*in the book of Proc. of EuroEM 2004*, July 12-16,2004, Magdeburg, Germany, pp. 665 – 674.

V. Kovalenko, A. Yarovoy, and L.P. Ligthart, "Waveform Based Detection of Anti-Personnel Landmines with an UWB Radar", - *in Proc. of IEEE International Conference on Ultra-Wideband*, September, 2005, pp. :644 – 649.

V. Kovalenko, A. Yarovoy, L.P. Ligthart, P. Hakkaart, and J.B. Rhebergen, "Joint IRCTR/TNO-DS&S measurement campaign for AP-mine detection with VIR GPR", - *in Proc. of the 3rd International Workshop on IWAGPR*, May 2-3, Delft, The Netherlands, 2005, pp. 31 – 36.

V. Kovalenko, A. Yarovoy, L.P. Ligthart, "Effect of the Data Pre-Processing on GPR Mine Detector Performance " - *in Proc. of IEEE EuMW*, October, 2005, pp. 73-76.

V. Kovalenko, A. Yarovoy, L.P. Ligthart, "Alternating-Sign Windowed Energy Projection of SAR Focused GPR Data" - *in Proc. of IEEE EuMW*, October, 2005, pp. 399-402.

V. Kovalenko, A. Yarovoy, L.P. Ligthart, "A SAR-Based Algorithm for Imaging of Landmines with GPR" - *in Proc. of IEEE Workshop on Imaging Systems and Techniques* , April, 2006, Minori, Italy, pp. 65-70.

V. Kovalenko, A. Yarovoy, L.P. Ligthart, "A SAR-Based Algorithm for Imaging of Landmines with GPR" - *in Proc. of IEEE Workshop on Imaging Systems and Techniques* , April, 2006, Minori, Italy, pp. 65-70.

V. Kovalenko, A. Yarovoy, L.P. Ligthart, "A Clutter Suppression/SAR Focusing Algorithm for Landmine Detection with GPR" - *in Proc. of 11th International Conference on Ground Penetrating Radar*, June 19-22, 2006, Columbus, OH, USA, CD-ROM.

V. Kovalenko, A. Yarovoy, L.P. Ligthart, "Normalization of Feature Distributions for Linear-Quadratic Fusion in Landmine Detection Using GPR" - *in Proc. of 3rd European Radar Conference*, September 13-15, Manchester, UK, 2006, 257-260.